2015

Wheel rail curve squeal modeling & rolling stock based mitigation measures

Chao Wang
University of Wollongong

WHEEL RAIL CURVE SQUEAL MODELING & ROLLING STOCK BASED MITIGATION MEASURES

A thesis submitted in partial fulfilment of the
requirements for the award of the degree

Master of Philosophy

from

UNIVERSITY OF WOLLONGONG

by

Chao Wang, B.Eng., MSc

School of Mechanical, Materials, Mechatronic Engineering
Faculty of Engineering and Information Sciences

2015

CERTIFICATION

I, Chao Wang, declare that this thesis, submitted in partial fulfilment of the requirements for the award of Master of Philosophy, in the School of Mechanical, Materials, Mechatronic Engineering, Faculty of Engineering and Information Sciences, University of Wollongong, is wholly my own work unless otherwise referenced or acknowledged. The document has not been submitted for qualifications at any other academic institution.

(Signature)

Chao Wang

31 August 2015

TABLE OF CONTENTS

LIST OF TABLES

LIST OF FIGURES

ABBREVIATIONS AND ACRONYMS

AAR —– Association of American Railroads

AOA —– Angle of Attack

ARTC —– Australian Rail Track Corporation

CCSB —– Constant Contact Side Bearer

CRC —– Cooperative Research Centres

CTA —– The Community Transportation Association of America

EDR —– Effective Damping Ratio

PN —– Pacific National

SEPTA —– Southeastern Pennsylvania Transportation Authority

SOAC —– State of the Art Cars

TfNSW —– Transport for New South Wales

TTC —– Transportation Test Center

ABSTRACT

Railway curve squeal, on one hand, has long been held as an annoying environmental problem to the local community which increasingly demands effective technical countermeasure to alleviate its impact; on the other hand, it is a complex theoretical question involving nonlinear wheel-rail contact mechanics, rail vehicle curving dynamics, and vibration instability of the wheel-rail structure. Many factors affect the transient phenomena of curve squeal and a large amount of field monitoring data have been collected in the rail noise CRC projects in NSW. Due to the intrinsic perplexity of curve squeal, field data analysis leads to ambivalent conclusions regarding the influence of wheelset angle of attack (AOA), wheel-rail contact state, wheel-rail structure and mechanical properties on curve squeal. This ambivalence demands theoretical investigation and clarification since it is possible to analyse individual parameters and their combination on curve squeal through efficient computation methods. This thesis addresses part of this mystery through investigation of the causes of large wheelset AOA based on railway vehicle curving dynamics and investigation of wheel-rail parameters on curve squeal based on finite element method and complex eigenvalue analysis.

For the sensitivity analysis of key bogie parameters on wheelset AOA, a detailed freight wagon model has been built on the multi-body dynamics software, VAMPIRE®. Bogie parameters and their ranges in operating life have been collected through close industrial connection and carefully calibrated in terms of accuracy and availability. Individual bogie parameters and combination of major influencing factors on wheelset AOA have been simulated, analysed and ranked in terms of their relative importance. To be more specific, these important parameters include equivalent friction coefficient of the centre bowl, friction coefficient of the CCSB metal cap, warp stiffness between side frames and bolster, and setup height of CCSB. The worst case scenario of bogie parameters in regards to wheelset AOA is also identified and

compared with field test wheelset AOA results. It would provide assistance for future rolling stock based curve squeal mitigation measures.

For the curve squeal prediction, a three dimensional wheel-rail contact and complex eigenvalue analysis model is built on the finite element software, ABAQUS. In the model, firstly, non-friction static contact is established under full axle load, then friction is introduced and a new contact state is searched under the constant sliding state. With this contact state as boundary condition, the friction induced damping effect on the vibration instability is evaluated during the subsequent complex eigenvalue analysis using the positive real part and negative effective damping ratio to indicate instability. Meanwhile, the wheel and rail mode shapes are visually checked to classify them into different categories and more importantly to identify the major vibration components in these unstable cases. The influence of individual parameters, such as wheel-rail friction coefficient, wheel rim thickness, lateral shift, rail support stiffness and damping, is discussed at first, and then combinations of wheel influencing factors, and different sliding directions between wheel and rail are incorporated. Together, this part of the study provides insight into the squeal mechanism under constant friction coefficient and constant sliding state, in contrast to the conventional analysis based on stick/slip and negative friction slope mechanism.

ACKNOWLEDGMENTS

The author is grateful to the CRC for Rail Innovation (established and supported under the Australian Government's Cooperative Research Centres program) for the funding of this research - Project No. R1.128 Enhanced Noise Management. The authors is also grateful for support from TfNSW, ARTC, PN, Aurizon and other members of the project steering committee.

Special gratitude for passionate supervision and continuous support of this thesis from A/Prof. Richard Dwight, Dr. Jiandong Jiang, Dr. Wenxu Li is acknowledged.

The author is also grateful for consultations with Mr. Peter Klauser, Mr. Bruce Sismey, Dr. Weiwei Liu and Dr. Tieling Zhang during curving dynamics modelling.

1. Introduction

1.1 Research background

Wheel-rail noise is a significant issue for many rail networks. Wheel-rail noise can be mainly categorized into three classes: (i) rolling noise on tangent tracks; (ii) squeal and flanging noise on low radius curves; and (iii) impact noise due to rail joint and wheel flats. Due to the wide application of continuously welded rail and regular wheel tread maintenance (machining), impact noise is no longer a prevalent noise issue now. Rolling noise is broad-band noise on the tangent track, which is prevalent from several hundred Hz to 5000 Hz. It is excited by irregularities of wheel-rail contact surface and strongly depends on train speed. Wheel and rail are equally important noise contributors to rolling noise. Squeal and flanging noise, also generalized as curving noise, have a relatively high noise level, usually 20-30 dB higher than rolling noise, which mainly affects local residents located near the particular curve. Rolling stock curving dynamics is thought to have a significant influence over the occurrence of curving noise. While flanging noise can be effectively alleviated by rail gauge face lubrication, squeal has proven to be more difficult to control effectively. Thus, both the academic community and the rail industry put more effort into investigating cause and mitigation methods for squeal.

1.2 Objectives and scope

(1) To develop theoretical models with improved accuracy on predicting curve squeal by possibly applying the current mechanism – coupling of degrees-of-freedom (mode coupling) – possibly leading to self-excited friction-induced oscillation in the case of constant friction coefficient.

(2) To investigate the sensitivity of key bogie parameters and the influence of related worn components on one of the key curving dynamics parameters for squeal occurrence – angle of attack of wheelsets.

(3) To determine how the coupling of degrees-of-freedom (mode coupling) can be

applied to reduce or eliminate curve squeal output for rolling stock in service by investigating the influence of key parameters on squeal occurrence and guiding wheel damping design.

(4) To develop a comprehensive set of knowledge on methods of noise mitigation related to rolling stock, ranging from angle of attack control by targeted maintenance criterion revision to new wheel damping devices development.

1.3 Thesis outline

The structure of the thesis is as follows:

In Chapter 2, a thorough literature review is presented, including railway curve squeal mechanism, curving dynamics, investigation on large angle of attack (AOA), and wheel damper design for squeal control.

In Chapter 3, a detailed multi-body dynamics model is built and used to investigate the influence of individual bogie parameters and their combinations on angle of attack (AOA).

In Chapter 4, a frequency domain FEM model of a single wheel and a short span of rail is used to investigate curve squeal tendency in the context of constant friction coefficient.

Chapter 5 summarises all the work accomplished in this thesis and proposes potentially valuable research questions for further investigation.

2. Literature review

2.1 Railway curve squeal mechanism

Railway curve squeal is a type of mono-tonal, high-pitch noise, which occasionally occurs when the railway vehicle is running along tight curves. It is generally considered to be a type of self-excited vibration instability of the railway wheel, similar to aerodynamic flutter, rather than a resonance phenomenon. However, the mechanism leading to instability is still a controversial topic.

2.1.1 Stick/slip and negative friction slope mechanism

Although there is little proof, from the start, it is generally accepted that curve squeal is generated by the "stick/slip mechanism". Rudd (1976) proposed three possible mechanisms of wheel squeal: (1) longitudinal differential slip between the inner wheel and outer wheel due to the different distances travelled by the two wheels on a solid axle; (2) flange rubbing which usually occurs between the outer wheel flange and high rail gauge corner; and (3) wheel stick/slide across the rail head induced by lateral creepage, named as "crabbing". The first mechanism was discarded, because vehicles with independently rotating wheels, which allowed differential rotation, still squealed when running along the tight curve (Rudd, 1976). The second mechanism was not sufficient, since experimental evidence showed that lubricating of the outer flange did not eliminate squeal and it was the inner wheels which squealed (Berglund, 1972; Steppenbeck, 1974). As a result, the third mechanism was investigated and an analytic model was presented. It was a one-degree-of-freedom model, representing a single wheel mode, which would only become self-excited and unstable under frictional force in the presence of falling friction slope versus sliding speed. The negative damping concept was introduced to represent that the friction force would increase the vibration energy of the structure and lead the system to become self-vibrated. Once the wheel vibrations become unstable, their amplitude will not go to infinity but develop into a limit cycle, since it will be limited by the non-linearities in the system. The limit of

vibration amplitude was stated stemmed from the change in the slope of the friction-creepage curve. Furthermore, it was believed that only one wheel mode was responsible for curve squeal. In his review article on wheel-rail squeal, Remington (1985) summarized the state-of-art of railway curve squeal up to 1985. It was concluded that a comprehensive analytical model of squeal needed to be developed, which should include the measured data on the friction coefficient versus lateral creep, the finite element model of wheel vibration, and the vehicle curving dynamics model. Based on Rudd (1976)'s research idea and Remington (1985)'s proposal, a number of more detailed models were developed by the following researchers.

Fingberg (1990) presented a finite element model of wheelset and a modal rail model to represent the vibration characteristics of both wheel and rail in high frequencies. The boundary element method was used to calculate the sound radiation of the wheel. The friction characteristic for low creepage before the saturation point was based on Kalker's theory (Kalker, 1979), and the one for high creepage after the saturation point to include the falling friction slope were based on Kraft (1967). One shortcoming is that the vehicle curving dynamics was not included, and the creepages were assumed to be known.

Périard (1998) extended Fingberg's work by determining the wheel-rail contact condition with a vehicle curving dynamics program for tram squeal prediction. The law of Poiré and Bochet, and the law of Galton were used to consider effect of the sliding velocity and humidity on the friction coefficient. The whole wheelset was modeled using the finite element method, while a model was built to calculate the wave propagation in rails at high frequencies. Finally, the sound radiation was evaluated by the Rayleigh intergral method.

Recently, a laboratory investigation led by Monk-Steel et al. (2006) found that in the presence of longitudinal creepage of 2%, a sustained falling region was not seen in the lateral friction force, and continuous squeal noise was not shown until the level of lateral creepage exceeds the longitudinal creepage. As a result, he suggested

longitudinal creepage should also be included in the railway curve squeal prediction model due to lateral creepage, which was developed by De Beer et al. (2003). Furthermore, test rig (scale 1:3) results, obtained by De Beer et al. (2003), indicated that the lateral position of the contact point on the wheel tread is of significant importance for squeal occurrence, that is, squeal noise only occurred for a contact position on the field side of the wheel tread, rather than the flange side.

A summary of the friction characteristics versus creepage applied in various curve squeal prediction models is shown in Table 2.1 and Figure 2-1. A reference rolling speed of 10 m/s has been used.

Table 2-1 Modelling of the falling regime based on experiments

Author	Friction characteristic	Data
Rudd (1976)	$\mu = \mu_0(\xi/\xi_0)e^{(1-\xi/\xi_0)}$	$\mu_0 = 0.4$
Kraft (1967)	$\mu_0(v) = \mu_{stat}\left(1 - 0.5e^{-0.138/\lvert v\rvert} - 0.5e^{-06.9/\lvert v\rvert}\right)$	$\mu_{stat} = 0.4$
Poiré/Bochet (Périard 1998)	$\mu_0(v) = \mu_{stat}\left(\frac{1}{1+0.03\lvert v\rvert}\right)$	$\mu_{stat} = 0.4$
Galton (Périard 1998)	$\mu_0(v) = \mu_{stat}\left(\frac{1+0.018\lvert v\rvert}{1+0.097\lvert v\rvert}\right)$	$\mu_{stat} = 0.4$

To sum up, the prevalence of this mechanism is mainly attributed to the experimental observation of the dependence of the friction coefficient versus sliding speed, known as the Stribeck effect. Meanwhile, it may be due to the fact that experts in the wheel-rail interaction academic community share a consensus on the wheel-rail rolling contact theory. This theory is built on theoretical and experimental foundations that partial wheel-rail contact patch is in sticking, and partial wheel-rail contact patch is in sliding at low creepage level, and after reaching friction force saturation, the whole contact patch will be in a full sliding state at high creepage level. However, full sliding will lead to wheel tread damage, like wheel flat, which is less likely to happen in a dry friction condition without considering braking. Thus, it is easier to accept the

"stick/slip" loop around friction force saturation point due to negative friction slope during curve squeal, even with little proof.

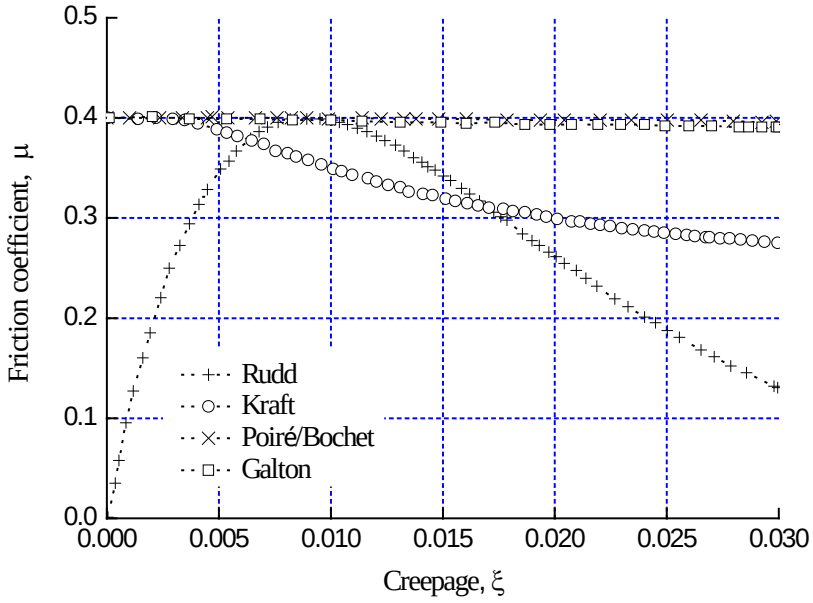

Figure 2-1 Friction characteristics used by various authors (Monk-Steel, 2006)

··+··rolling friction according to Rudd,

··o··sliding friction according to Kraft,

··×··sliding friction according to Poiré/Bochet,

··□··sliding friction according to Galton

The main drawback of these models based on the negative friction slope mechanism is that these squeal prediction results are extremely sensitive to the chosen function for the dependence of the friction coefficient versus creepage. In fact, real tracks are subjected to environmental conditions and wear processes (abrasion, corrosion, dirt, etc.), and thus it is quite doubtful to assume that the friction conditions during squeal can be described by just one particular friction curve. Secondly, negative damping predicted by Rudd's theory is very high compared to what is needed in real situations to eliminate curve squeal by increasing the wheel loss factor. As reviewed by Remington (1985), up to 1985, the most successful treatment for squeal was wheel damping, which had demonstrated repeatedly to effectively eliminate squeal. As a result, it was stated that this discrepancy clearly indicated a weakness in that theory.

2.1.2 Coupling of degrees-of-freedom mechanism

Vibration systems with a constant normal contact force may show self-excited vibration only if in the presence of negative friction slope. This is the case for the Stribeck friction law. If the normal contact force is not constant but is coupled with the vibrations of different degrees-of-freedom and phase angle differences exist among them, then even in the constant friction coefficient condition, self-excited vibration instability can still take place, if the friction force couples at least two degrees-of-freedom together (D'Souza, 1990). This type of instability can also be called flutter instability, mode-coupling, or mode coalescence. It has been first exemplified by analytical models developed by authors like Jarvis and Mills (1963-1964), Earles and Lee (1976), North (1976), Millner (1978), Hoffmann et al. (2002). Then, increasing computation power makes it possible to perform complex eigenvalue analysis (CEA) on the finite element model, with the positive real part of the system complex eigenvalues indicating instability of modes (Ouyang, 2005). Mode coupling (or mode coalesence) in large structures (like an automotive disc brake system) is in essence the same phenomenon as the coupling of two degrees-of-freedom due to friction force. However, the complex eigenvalue analysis provides a conservative approach (Nack, 2000). The positive real part of the eigenvalue is necessary, but not sufficient, to predict the occurrence of unstable vibrations, not all unstable modes predicted by CEA will grow into limit-cycle vibration (Tarter, 2004). To improve CEA performance, energy criterion, like the calculation of feed-in energy, can help to indicate the level of squeal tendency and the most likely squeal mode (Guan, 2003). The modal assurance criterion (MAC) can provide a quantitative method to assess the relative contribution of normal modes of individual components within the unstable complex mode. The normal modes with high MAC values can then be redesigned to decouple the vibrations (Park et al., 2001).

For railway curve squeal prediction, finite element complex eigenvalue analysis in the case of constant wheel-rail friction coefficient and pure sliding was carried out by

Chen (2008). This model included a finite element model for a single wheel and one rail with contact springs between wheel and rail using NASTRAN. Limited convincing results of unstable modes were obtained, since without the assistance of additional criterion (for example, feed-in energy and MAC), it is hard to identify which system modes are more prone to become unstable and thus squeal, and the contribution of the corresponding wheel mode and rail wave to the prone-to-squeal unstable complex mode of the wheel-rail system. Possibly due to the difficulty and complexity to determine the damping value of the track system (mainly the damping properties of a rail pad in the concrete sleeper track system or that of a timber sleeper in the timber sleeper track system) in high frequency, track damping was not considered in this model.

Glocker et al. (2009) and Cataldi-Spinola (2007) developed a new approach to predict curve squeal in the case of a constant friction coefficient. Unilateral contact and Coulomb friction, instead of Kalker's rolling contact theory, was used in this high-frequency squeal prediction model. Only wheel elasiticity was considered in this model. The equilibrium condition for steady-sliding was determined and a stability analysis of the leading bogie's wheels was conducted for various wheel diameters, different friction coefficients and different directions of sliding velocity. The contact positions and sliding velocity of the leading bogie's wheels were pre-determined by the rigid-body vehicle curving dynamics model of a driving trailer during negotiation of a tight curve. After identifying the configurations which may lead to curve squeal, time-stepping methods were used in the numerical integration of the time-domain squeal model. Periodical oscillation of normal contact force was observed, which is due to the elasticity of the wheel. In phase portraits, the presence of the limit cycle of longitudinal and transversal contact velocity-displacement can be seen, with a frequency of about 3.99 kHz. Besides, three modes of free wheel, which occur at similar frequencies, were identified to be essential to that squeal event around 4 kHz. One was responsible for the wheel rim vibrating in the lateral direction, and two radial

modes allowed for the normal force variation. It concluded that these combined conditions leading to vibration instability and squeal (constant friction coefficient, normal force variation, and coupling of three different modes in normal and tangential directions) can be attributed to the coupling of the normal and tangential degrees-of-freedom mechanism, which is, within a certain range, insensitive to the chosen friction curve.

Pieringer (2011) recently presented a detailed time-domain model to predict curve squeal in the case of a constant friction coefficient. Wheel and rail high-frequency vibrations were represented by impulse response functions which were derived from a finite element model of wheel and a waveguide finite element model of rail. This simplification significantly reduced the computation effort and enabled the inclusion of a three-dimensional, non-linear and transient contact model which was solved at each time step in the wheel-rail interaction model. It was a modification of Kalker's Program – CONTACT, which added the global vertical and tangential displacement of the wheel and rail vibration to the normal contact and tangential contact model at each time step and was solved iteratively. Wheel-rail contact positions, lateral creepage and wheelset angle of attack were pre-calculated through a vehicle curving dynamics model. The rms-value of the lateral contact force was introduced to characterise the relative instability and thus squeal tendency. The simulation results confirmed that the stick/slip was possible in the case of constant friction, which was attributed to the coupling between normal and tangential vibration. However, it was admitted this time-domain model gave limited insight into the underlying mechanism. Bending modes with zero nodal circles were found to be closely correlated to instability and thus squeal. One or two wheel modes could be shown to participate in each stick/slip oscillation at different frequencies. Key parameters of wheel-rail contact - lateral creepage, lateral contact position, and the value of friction coefficients – all showed a significant influence on the likelihood of squeal.

2.1.3 Summary

Since railway curve squeal is a type of friction-induced, highly non-linear and transient phenomenon, and is related to the intrinsically complicated wheel-rail interaction in the high frequency range, understanding and modelling this phenomenon is still a challenge.

From the literature review presented above, modelling based on a negative friction slope mechanism has a major shortcoming - namely the extreme sensitivity and dependence of the squeal prediction results on the chosen friction function. Also, the friction modifier based on this mechanism and designed to overcome negative friction characteristics has only achieved limited success in eliminating curve squeal. Moreover, recent curve squeal simulations based on the coupling of degrees-of-freedom mechanism show that in certain combined conditions squeal occurs in the case of a constant friction coefficient. It is possible that both mechanisms occur in practice. Further investigation needs to be conducted to improve the accuracy of theoretical modelling in regards to the tendency and amplitude of curve squeal. After that, laboratory and field tests should follow to verify this.

2.2 Classic vehicle curving dynamics

Redtenbacher (1855) provided the first theoretical analysis of the rolling of a coned wheelset on a curve. A simple geometric formula was derived to present the lateral movement of a wheelset in pure rolling during curving. This situation is only achievable in sufficient large curve radius or flangeway clearance. Later, Mackenzie (1883) presented the first correct description of curving with the inclusion of friction forces. His calculations showed that the outer wheel flange exerts a lateral force against the outer rail, which is sufficient to balance the friction of the wheel treads.

Modern research on curving is marked by the linear model developed Boocock (1969) and Newland (1968). Coned wheelsets are constrained by suspension elements in longitudinal, lateral and yaw degrees-of-freedom. These suspension elements connect

the axles and the bogie frame and carbody. The attitude of the bogie vehicle and the force acting on each rigid body are derived by solving the equations of equilibrium of the multi-body system. Since linear functions are used to approximate the suspension elements, the wheel-rail geometry, and the creepage/creep-force relationship, it is valid only for large radius curves, due to the limit of linear theory. The nonlinearities due to creep saturation and wheel-rail contact geometry in flange and flange root contact cannot be included in the linear model. Besides, for freight wagons, the nonlinear characteristics for friction dampers, and steel-steel connections between the main bogie components cannot be reflected by the linear model correctly.

The first comprehensive nonlinear treatment of practical vehicles curving simulation stemmed from the work by Elkins and Gostling (1977). Contact nonlinearities caused by the change of contact patch and friction saturation are taken into account. As the wheel lateral position increases, the inclination of the normal force, and the lateral creep force generated by spin are also taken into account. This is done by accessing a lookup table created by Kalker's CONTACT model which calculates the tangential creep forces for arbitrary values of creepage and spin and for a wide range of contact ellipticities.

Since the 1980s, commercial railway vehicle dynamics becomes increasing available, including SIMPACK, VAMPIRE, NUCARS, ADAMS, GENSIS. With the assistance of such software, finer models can be introduced to represent the effects of freight wagon suspension nonlinearities, which are more pronounced during curving. Although these software packages liberate engineers from the laborious work of programming all modules from the start, the accuracy of modelling still heavily depends on the user's expertise and capabilities on deciding the complexity and limitation of the model relative to the physical problem under investigation.

2.3 Curving dynamics performance index – Angle of attack

2.3.1 Why wheelset AOA is targeted

Curving performance of a rail vehicle bogie can be measured by the angle of attack, AOA, which the wheels adopt when traversing a curve. AOA for a rigid wheelset can be defined as the yaw angle of the wheelset from its radial position; alternatively, it is the angle between the track radial line and the centre line of the axle of the wheelset. High AOA has been shown to be a necessary condition for curve squeal (Rudd, 1976; Remington, 1985; Fingberg, 1990). Generally the higher the wheelset AOA, the higher the squeal noise level. This appears to be logical given that the level of AOA corresponds to the level of lateral creepage. This results in lateral friction force and friction energy, which is the source of excitation of the self-excited vibration of wheel squeal.

Evidence from observation on rail systems (Anderson, et al, 2008; Dwight, Jiang, 2009), indicate that, when the AOA of the leading wheelset of the leading bogie on a curve is within the normal range (within 10 mrad), moderate (lower decibel) squeal may occur. When the AOA is high (exceeding 20 mrad), severe (much higher decibel) squeal may occur (Anderson, et al, 2008; Dwight, Jiang, 2009). From limited data collected at one site on a 300 m radius curve, the noisiest curve squeal events (exceeding 110 dB at 2m) were observed when axles pass with an AOA exceeding 20 mrad; events exceeding 120 dB at 2m were only observed when axles pass with an AOA exceeding 30 mrad (Anderson, et al, 2008; Dwight, Jiang, 2009).

For the widely used conventional three-piece bogie, the vast majority (95%) of those passing through a trackside monitoring site expect to perform what is accepted to be a normal AOA within a range of 10 mrad on the leading wheelset of the leading bogie (Anderson, et al, 2008; Dwight, Jiang, 2009). Around 2% of the axles showed an AOA greater than 30mrad corresponding to a very poor curving performance (Anderson, et al, 2008; Dwight, Jiang, 2009). The reasons for this variation are not evident.

Understanding the reasons will lead to more effective management of AOA, associated bogie component wear, and wheel squeal.

A normally-performing freight wagon with three-piece bogies has a small AOA for trailing axles on curves. The leading wheelsets of the conventional three-piece bogies on curves should have an AOA close to 1 mrad for each degree of curvature. Normal AOA of the leading wheelset should be close to 6mrad when negotiating a 291 m radius curve (a 6-degree curve) (Shust, Urban, Lovette, 2000).

2.3.2 Common causes of abnormally high angle of attack

For abnormally large AOA, common accepted causes associated with the vehicle, are (Wolf, 2004; Hagaman, 1998; Tickell, 2004; Skerman, 2009): (1) bogie warp, resulting from either insufficient steering moment mainly caused by hollowed wheels; or insufficient warp stiffness due to wedge rise; or significant resistance to bolster rotation due to excessive friction in the centre bowl or tight side bearers; (2) steering effects from bogie component geometry variations, such as difference between wheel diameters or between side-frame wheelbase dimensions; and (3) characteristics of components such as brake rigging or springs.

Bogie warping refers to the condition where the two side frames adopt a parallelogram position; the bogie is twisted out of square during curving. It is measured by the warp angle α: the side frames move back and forth relative to the centre plate as shown by the horizontal arrows in Figure 2-2 and the bolster adopts an angle α relative to the side frames. The resistance to the side frame warping/ parallelogramming motion is referred to as warp stiffness (MNm/rad). As shown in Figure 2-3, if two side frames twist as much as one degree (17.5 mrad) out of square, the bogie is considered to be “warped”, (Wolf, 2004). Bogie warping gives rise to high AOA (Mace, 1994; Simson, 2006d).

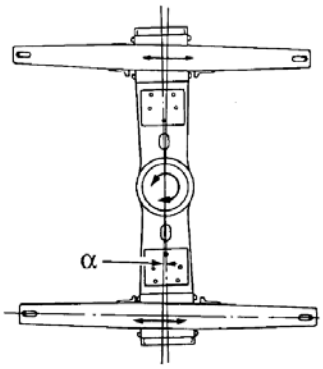

Figure 2-2 Warping/Parallelogramming motion (Hawthorne, etc., 1990)

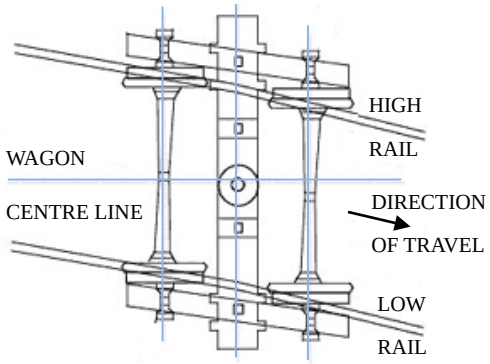

Figure 2-3 An abnormally curving, warped bogie (Wolf, 2004)

Geometry differences may be expected to improve curving performance in one direction of travel and degrade curving performance in the opposite direction. Such effects may become evident if consistent tracking and monitoring of a vehicle while travelling in different directions is possible. From trackside monitoring (Dwight, Jiang, 2009), most freight wagons with large AOA usually show continuously large AOA in both directions, which indicates that the cause is typically not related to geometry properties. Abnormal angle of attack caused by brake rigging and spring have been reported (Kopke, 2004). No researched evidence for this has been found in the literature.

2.3.3 Relationship between high AOA and large bogie warp angle

Bogie warp occurs when forces acting on a bogie cause it to warp in such a way that both wheelsets develop a large AOA (Mace, 1994). A bogie is warped by sufficiently large reversed steering moments to overcome the centre bowl and side bearer friction

moment and the bogie's inherent warp resistance. A direct correlation between large bogie warp angle and large AOA of a 100-ton ASF Ride Control trailing bogie has been indicated in both simulation modelling and AAR's Transportation Test Center (TTC) track test results, as shown in Table 2.2 (Mace, 1994).

Table 2-2 Bogie steering moments and angles in a 7.5 degree curve (Radius=233m) (Mace, 1994)

	Wheelsets	Leading wheelset Steering Moment of the trailing bogie (kip-in)	Bolster Warp Angle (mrad)	Wheelset AOA (mrad)	
				Lead	Trail
NUCARS Modeling	Worn Heumann	+40	5	10	2
	Hollow	-90	11	15	8
In-situ Measured	Worn Heumann	+18	4	11	3
	Hollow	-60	18	24	19

In another typical study (Simson, 2006d) for a 106-ton VSA wagon, it is found that excessive flange wear when negotiating a 304.5 m radius curve is related to bogie warp on the leading bogie caused by high bogie rotation friction. Figure 2-4 (Simson, 2006d) indicates that both of the wheelsets (axle 1 and 2) of the leading bogies are in flange contact and thus the AOA of these wheelsets increases as a direct result of bogie warp.

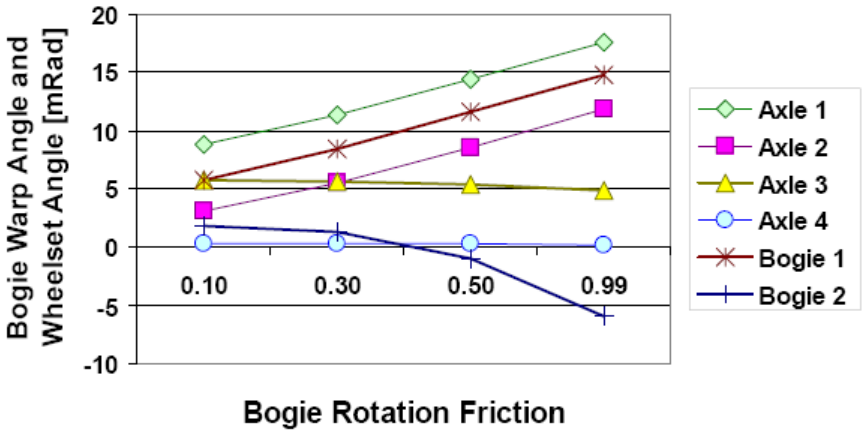

Figure 2-4 Bogie warp and AOAs during negotiating a tight curve (Simson, 2006d)

A closer investigation of AOA differences at 40 km/h and 60 km/h is presented in

Figure 2-5, where the AOA at 40 km/h are higher than that at 60 km/h. Simson (2006e) suggests that this represents the increase of the bogie warp retained in the constant radius curve caused by rotation friction moments at the centre bearing. In short, bogie warp will lead to large AOA of both wheelsets of the same bogie (Wolf, 2004, Mace, 1994, Simson, 2006d).

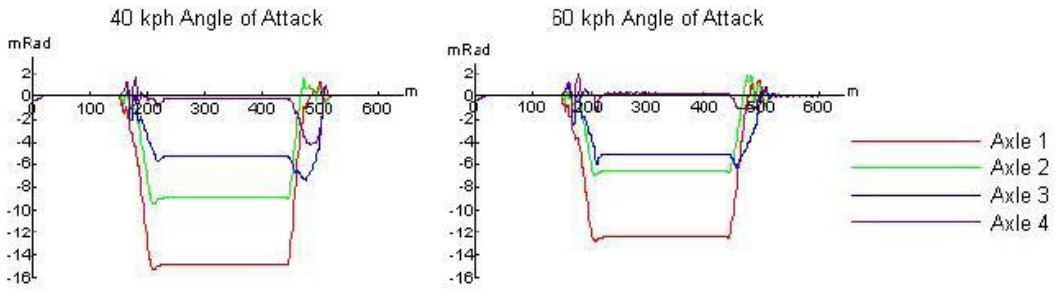

Figure 2-5 Wheelset AOA over the 304 m radius curve for steel wear liner (Simson, 2006e)

2.3.4 Bogie warp due to excessive worn bogie components

When a three-piece bogie traverses a curve the leading wheelset is forced laterally outward by the centripetal force. By design the wheel tread profiles are normally based on a conical shape so that the rolling radius difference between the inner and outer wheel generates a steering moment. This tends to "steer" the bogie around the curve. This steering force from wheelsets will be transferred through bearing adapters, and into the sideframe, through the friction wedge and the spring group, and eventually into the bolster. A turning moment between the bolster and the carbody will be generated to balance the steering moment of the wheelset and the warp moment of the interface between the sideframe and the bolster, as shown in Figure 2-6. The relationship discussed above can be represented by Equation 2-1 below:

$$\alpha=(M_t-M_s)/K_w \tag{2-1}$$

where M_w is warp moment, M_t is turning moment, M_s is steering moment, α is warp angle, and K_w is warp stiffness respectively.

This equation demonstrates that a large warp angle (α) can be caused by a large turning

moment (M_t), insufficient steering moment (M_s), insufficient warp stiffness (K_w) and/or combination of these three factors.

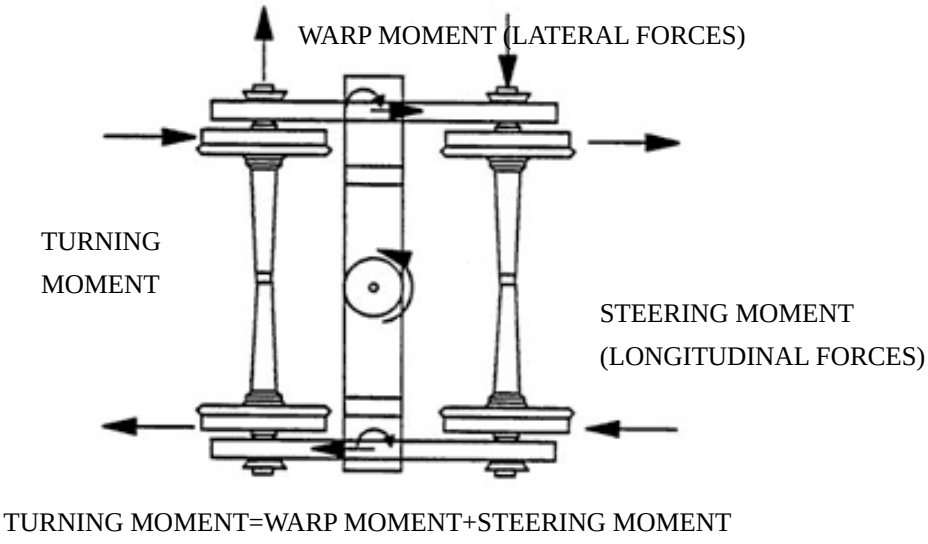

Figure 2-6 Equilibrium during curving (Wolf, 2004)

(1) Large turning moment

Large turning moment between carbody and bolster can be caused by excessive friction in the centre bowl, or rotational resistance due to tight side bearings or possible additional rotational resistance created by the constant contact side bearers (Wolf, 2004):

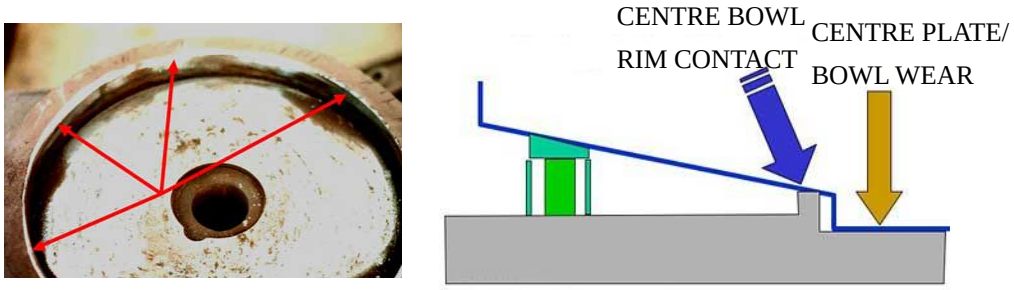

Figure 2-7 Worn centre bowl, the contact of the bowl rim (Wolf, 2004; Wolf, 2005)

Under normal design conditions, when the carbody centre plate rotates within the centre-bowl, the turning moment of the two surfaces in contact can be defined by Equation 2-2, where an even distribution of vertical load across the surface of the centre bowl is assumed (Wolf, 2005).

$$M_{CB} = R(2/3)\mu N \qquad (2\text{-}2)$$

Where M_{CB} = centre plate turning moment;

R = the radius of the centre plate;

μ = the friction coefficient;

N = the normal force from carbody weight.

In the situation where there is substantial wear on the surface of the centre plate or centre bowl, the centre plate will sit deeper in the centre bowl, which may cause contact around the rim of the centre bowl, as shown in Figure 2-7. In this case, the turning moment radius is moved to the extreme radius of the centre bowl rim, as described in Equation 2-3 (Wolf, 2005).

$$M_{CB} = R\mu N \tag{2-3}$$

The substantial increase (33% increase based on Equations 2-2 and 2-3) in turning moment due to a worn centre bowl can cause the wheelset steering moment to be insufficient to steer the bogie bolster through the curve, thus bogie warp occurs (Wolf, 2005).

Simson (2006a, 2006b) investigated a series of factors which affect bogie rotation friction for a heavy-loaded coal wagon with 106 ton gross weight, including centre bowl friction, side bearer type and curve transition design. Increased wheel-rail wear is concluded to be generated by large AOA due to bogie warp. Excessive rotational resistance of the centre plate polymer liners, that is the large turning moment, is identified as the root cause of the high wheel-rail wear. The constant side bearer is not the source of major rotational resistance of the loaded wagon as first thought (Emereole, 2006). Centre plate lubrication and different designs of low polymer liners have been trialled in order to improve wheel-rail wear. Simson (2006c) found that wheel-rail wear in gentle curves for three-piece bogie increase significantly with centre plate bearing rotation friction, however, in very tight curves there is almost no change in the total wheel-rail wear.

Moreover, tight side bearings can also cause resistance to bolster rotation. In a specific

case of a type of coal wagon with conventional three-piece bogie, it is reported that modification of constant side bearer, replacing the CCSB with the gap-type roller side bearer, is very effective in reducing squeal noise (Tickell, 2004).

(2) Insufficient steering moment

Insufficient steering moment, produced by longitudinal creepage forces, is mainly due to poor wheel-rail profiles and friction condition, typically, hollowed wheel.

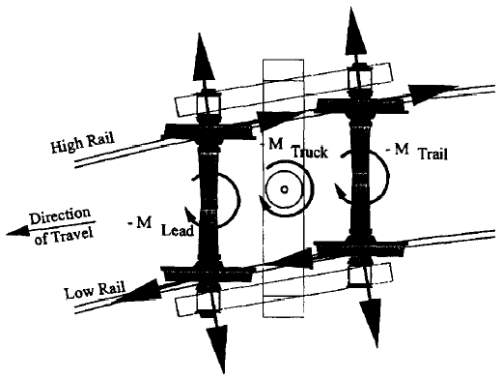

Figure 2-8 Steering moments during normal curving (Mace, etc., 1996)

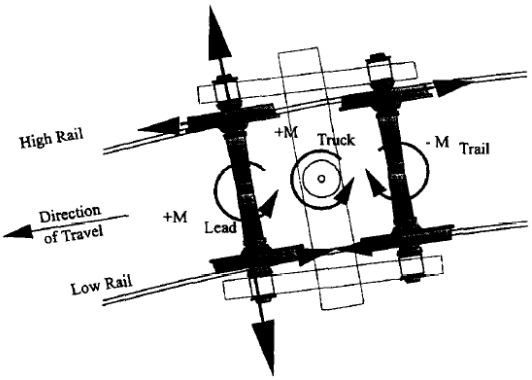

Figure 2-9 Steering moments during curving, warped bogie (Mace, etc., 1996)

Numerical curving dynamics results show that when hollow wear of the wheel exceeds 2.9 mm (Sawley, 2005), the leading wheelset may produce a negative steering moment which, in combination with negative trailing wheelset steering moment, reverses the net steering moment of the bogie, as shown in Figure 2-8 and Figure 2-9. A negative bogie steering moment resists the rotation of the bogie in the entry transition curve and, if of sufficient magnitude, the bogie steering moment (caused by longitudinal creep forces) exceeds its inherent warp restraint then the bogie warps instead of rotating (Mace, DiBrito, etc., 1994; Mace, Pena, etc., 1996).

(3) Insufficient warp stiffness

Tests of conventional three-piece bogies have shown that a significant proportion of the inter-axle shear stiffness (warp stiffness) that governs their hunting and warp performance relates to the connection between side frame and bolster. However, most designs have been deficient in the magnitude of resistance to yaw (warp) movement between the side frame and the bolster. To compensate, shear plates, braces, and linkages have been introduced to increase the warp stiffness of the suspension. Taillon (2001) introduced a friction wedge design method to maintain a minimally sufficient warp resistance and optimum vertical coulomb damping, without the need for additional stabilization and bracing devices. Wedge width has been identified to have a significant effect on warp stiffness and have no effect on vertical damping, which make it a good choice for design. In combination with a sufficient wedge width, the smaller-than-normal wedge angle becomes a powerful feature for producing a combination of high warp friction moment with low to moderate damping force.

During service, the wedge pocket and the column wear plate will gradually wear, and the friction wedge itself will be smaller. The net result of wear is that the preload of wedge spring will be smaller and thus the friction wedge itself be pushed upward by the wedge spring. In this process, the warp stiffness and damping provided by the friction wedge will be reduced. This phenomenon is termed “wedge rise” (Wolf, 2004). From a test of an ASF 70 ton ride control bogie, the value of warp stiffness of a full-worn bogie is only 63% of that of a new bogie (Hawthorne etc., 1990).

2.3.5 Summary

A normal freight wagon should have a small AOA for trailing axles of each bogie on curves. The leading wheelsets of normal traditional three-piece bogies on curves should have an AOA close to 1 mrad for each degree of curvature. High AOA for a conventional three-piece bogie is identified to be closely related to bogie warp. Bogie warp results from insufficient steering moment from wheel-rail contact mainly caused by the hollow-worn wheel, insufficient warp stiffness between sideframes and bolster,

and excessive turning moment between bolster and carbody.

Investigation of the effect of friction coefficient and constant contact side bearers to high AOA depends on wagon load, since turning moment between bolster and carbody directly depends on wagon load and load distribution between centre plate and side bearers. A fully loaded wagon is used to represent the maximum possible turning moment due to centre plate load and side bearer load for designing the maximum warp moment the friction wedge need to resist (Taillon, 2001). Besides, investigations of bogie rotation friction moment and wheelset steering moment due to hollow wheel tread profile are generally related to a specific combination of other bogie parameters.

Question 1: The quantitative relationship between the bogie warp angle and the AOA of the individual wheelset is still not clear and is known to depend on the bogie types and other specific curving dynamics context.

Question 2: Are there any occasions when the wheelset shows large AOA while the bogie is not warped?

Question 3: It is not clear whether the root causes of high AOA identified in each case study of specific types of bogie and specific curve site situations in the literature can be extended to other cases. In this thesis, a most frequent prone-to-squeal bogie type with large AOA identified in the field monitoring needs to be investigated since there is no previous theoretical research on this particularly large AOA issue conducted for this type of wagon or associated bogies. The influence and ranking of importance of bogie parameter and their combination in different worn conditions on wheelset AOA should be clarified.

2.4 Vehicle and wheel-rail dynamics in higher frequency

Models of classical multi-body vehicle dynamics have been built to consider the fundamental dynamics of the vehicle-track system, for instance, hunting stability, curving performance and ride comfort, which typically cover frequencies from 0 Hz to 20 Hz (Elkins, 1992). Obviously, if we want to study curving noise issues, this frequency range and modelling must be extended. However, the feasibility of a

combined numerical treatment of both the low frequency vehicle dynamics and the high frequency squeal dynamics should be considered with respect to the different associated time scales. For instance, to execute a quasi-static curving analysis, a track length of about 50 m is assumed. It takes the vehicle 12.5s to go through in a running speed of 4 m/s. Meanwhile, the period at a squeal frequency of about 4 kHz is 250 μs, which makes a factor of 50 000 between the two time scales (Glocker, et al., 2009). However, the traditional squeal models present a weak link between the low-frequency vehicle dynamics model and high frequency squeal dynamics model, by providing the wheel-rail contact parameters and results from the low frequency vehicle dynamics calculation to high frequency vibration and squeal model. The contribution of wheel and rail vibration at middle and high frequencies to the wheel-rail interaction and vehicle curving dynamic behaviour is neglected. Wheelset and track are often modelled as rigid bodies in classical multi-body vehicle dynamics, but wheelset structural flexibility (and track flexibility) may affect the vehicle track interaction.

With the increasing calculation power of computers, it is quite possible and valuable to run real-time squeal simulations as the vehicle transverses a tight curve by including wheelset flexibility and track flexibility into the vehicle dynamics.

2.5 Wheel damper for curve squeal mitigation

When a train traverses a sharp curve, it may emit an intense, mono-tonal noise. It sounds like a whistle or high pitched note and is generally termed as ‘curve squeal’. It is generally recognised that the origin of curve squeal is the so-called ‘stick-slip loop’ that occurs in the contact surface between wheel and rail. It is a phenomenon related to curves, since high levels of lateral slip mainly occur in narrow radius curves (for most railways narrow curves typically are defined to have a radius below 500 meters in metro and tramway below 100 m). Squeal will appear when a lateral natural frequency of the wheel is excited, meanwhile, the rail contribution to squeal noise is considered to be limited.

Solid wheels normally have a very low damping and have a large number of

eigenfrequencies and associated mode shapes. The probability of coincidence of the excitation with one of these frequencies is therefore rather high; considering furthermore that wheel damping is normally extremely low for lateral bending modes, it is easy to understand that once the stick-slip process has started it tends to “tune” on a very limited number of lateral bending eigenmodes, causing the extremely tonal squealing noise.

As is generally known, squealing noise appears only if damping is below a given threshold, in other words, squeal does not happen if wheel damping is artificially increased above the same threshold. Theoretical consideration from Remington show that squeal noise will not occur if the wheel damping is high enough (> 10%) to overcome the oscillations induced by the stick-slip phenomena (Kluijver de,1997), although his work, based on negative friction slope, tends to overestimate the damping value actually needed to inhibit stick-slip oscillation and eliminate squeal. Some common type of wheel dampers will be discussed as below:

2.5.1 Ring damper

(1) Description:

Ring dampers are steel rods, 0.5 inches in diameter for example, which are bent into a circle and inserted inside grooves machined under the wheel rim, as shown in Figure 2-10 The end of the ring may be left loose, welded to each other, or connected with an adjustable tensioning device (Kurzweil, Wittig, 1981).

(a) Valdunes ring damper **(b) welded position** **(c) the system for controlling preload**

Figure 2-10 Ring damper (Brunel, 2010)

(2) Mechanism:

The mechanisms of friction damping and interaction between ring and wheel groove, and associated squeal attenuation are not well understood. Friction or impact between the ring and groove are usually thought to be the mechanism for squeal noise attenuation (López, 1999; López, 2004). Besides, recent research progress from France proposes that the vibration and noise attenuation is due to modal coupling between the wheel and the ring (Brunel, 2010).

Parameters which act on the efficiency of the solution are the number of rings, their position, weight and assembly into the groove (preload) (Brunel, 2004).

(3) Effectiveness:

The effectiveness of the ring dampers, in fact of any damping techniques, in suppressing squeal, is related to the amount of damping they provide at the squeal frequencies.

The double ring solution, used in the Valdunes “Corail” wheels in Figure 2-10 (a), has already been employed successfully on several transit applications (Paris, Hong-Kong, etc.). Attenuations vary from roughly 5 dB to more than 10 dB. For the Hong-Kong experimental setup, a special test train arrangement has been done with one part of the train equipped with existing wheels and the rest with Valdunes ring damped wheels. An outside microphone located at a distance of about 2 to 3 m from the track has measured the wheels acoustical signatures. A sound level attenuation of 10 dB is obtained between the existing wheels and the Valdunes ring damped wheels. Nevertheless, the same ring damped solution has been inefficient for other applications in Argentina and in Switzerland (Brunel, 2004).

Wheel squeal noise reductions of the order of 9-11 dB were observed for ring dampers that were not frozen in place. When frozen in their grooves, squeal

noise reduction effectiveness is 3-5 dB or totally lost, as a result of dirt and other material freezing the ring damper in the retaining groove (Nelson, 1997).

Besides, the damping value of numerous configurations of the ring damper are measured and evaluated in Kurzweil's report. It is not clear from these results whether the mass of the ring (relative to the wheel rim mass), the damping properties of the ring, the area over which the ring contacts the groove, ring tension, or some other parameters are most important in optimizing damping. One of the highest damping configurations was the worn wheel with steel damping ring (Kurzweil, Wittig, 1981).

(4) Advantage:

It is a simple and cost-effective method to reduce squeal noise. The ring damper costs about $35 per wheel, compared with $500-1000 per wheel for a tuned mass damper, and $1500-1800 per wheel for constrained layer damping treatment (Nelson, 1997).

Compared with the machined "T-shape" uneven groove and the deep tap hole drilled in the wheel rim for mounting the tuned mass damper, the groove for the ring damper is comparably small (0.5 inches in diameter) and has a smooth half-circle cross section. It is considered relatively safer by railway operators and wheelset manufacturers in regards to stress concentration near the groove which may later lead to crack formation and wheel failure.

(5) Disadvantage:

It has been observed that the effectiveness of ring dampers depends on the application and may vary a great deal from one wheel to another with no plausible explanation (Brunel, 2010). Because the mechanisms of attenuation are not well understood, these variations have not to date been explained.

After ten months of service on SEPTA, the ring dampers were found to be tightly bound in the wheel grooves, with an accompanying loss of effectiveness.

The rings appeared to have rusted in the grooves. The problem was also observed to have occurred on the SOAC car at the Transportation Test Centre. The CTA has not experienced this problem during several years of experience with ring-damped wheels. It is important to note, however, that the CAT cars are disc braked, whereas the SEPTA cars and SOAC cars are tread braked. The higher wheel temperatures and brake dust from the tread brakes could be contributing to this problem (Kurzweil, Wittig, 1981).

When frozen or rusted in their grooves, the rings lose their frictional damping characteristics, thus squeal noise reduction effectiveness is lost.

The placement of the groove on ring damped wheel tested at SEPTA, requires the removal of material from the wheel tyre and reduces the useful life of the wheel when the rings are placed on the field side. The CTA has developed designs for new replacement wheels which provide an extra 1 cm of metal in the tread so that the field side ring grooves will not reduce the wheel life (Kurzweil, Wittig, 1981).

By placing the groove on the flange side, the permissible wear of the tyre is not affected. However, several transit authorities have raised the question of the grooves causing stress concentrations in the wheel that could lead to wheel failures, particularly with the grooves on the flange side of the wheel. London Transport, the only system to have widely applied ring dampers, has not experienced problems resulting from stress concentrations at the grooves for the dampers (Kurzweil, Wittig, 1981).

(6) Commercial product:

Several commercial products are available and have been put into operation for years. Valdunes ring damped wheels are in service in trains of various metro lines (Helsinki, Hong Kong, New York, Paris) as well as in certain locomotives (Norway, Switzerland) (Müller, 2003). In Queensland, ring dampers fitted to

some passenger rolling stock have been successful in reducing squeal (Anderson, 2008b). This type of ring damped wheel (IMU wheel) is supplied by OneSteel Ltd in Australia, with the ring placed on the field side, not on the flange side of the wheel (Skerman, 2011).

2.5.2 Tuned mass damper

(1) Description:

(a) VSG damper (Bochumer Verein, 2011)

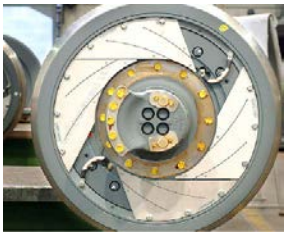

(b) Shark fin damper (Schrey & Veit GmbH, 2011)

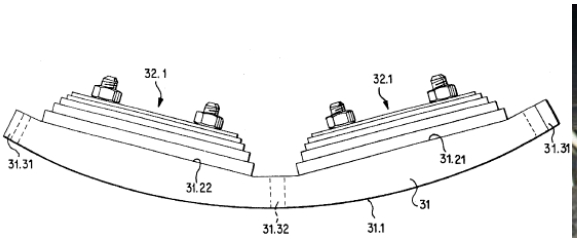

(c) VICON-RASA damper (Schrey & Veit GmbH, 2011)

Figure 2-11 Tuned mass damper

VSG tuned mass dampers (as shown in Figure 2-11(a)) consist of a series of tongues with damping material between them, are usually mounted with screws and nuts in a “T-shape” circular groove. The resonating frequencies of the

absorbers are exactly tuned to the frequencies of the wheels (prone to squeal) to be damped.

Shark fin dampers (as shown in Figure 2-11(b)) acting as a tuned absorber, consist of damped sandwich plates, and are mounted onto a ring which is concentric to the wheel tyre and fastened to it with a number of bolts. Each plate is split into three to four slices, and each slice corresponds to a modal frequency of the wheel, which can enable the energy at the vibration frequency to pass to the plates and then be dissipated in the form of heat energy.

The VICON-RASA absorbers (as shown in Figure 2-11(c)) consist of a series of layers of metal and damping plates and have the same curvature as the ring segments, to which they are riveted. Individual vibration absorbers are fastened to the segments of a ring fitted into the inside circumference of the wheel rim.

(2) Mechanism:

Tuned mass dampers dissipate energy depending on the local displacement in a structure, rather than as layered damping treatments that depend on surface strains. Essential prerequisites for a single degree of freedom tuned damper to be of value are that the damper be located at a point on the wheel of high displacement response, such as an antinode, and that the structure has a single resonance or a group of resonances with similar significant strain energies.

In addition, tuned dampers can be designed with multiple resonances that occur at relatively widely separated frequencies that can in turn be effective in damping structures over a broad range of frequencies. This is the requirement for curve squeal control, which usually involves several (3~5) vibration modes of the specific wheel that are tuned to be damped at specific narrow (prone to squeal) frequency band.

(3) Effectiveness:

Vibration absorbers attached to the wheel rim/tyre and designed to absorb vibration energy over a range of frequencies from 400 Hz to 5000 Hz can be effective in reducing wheel squeal. Usually, high-frequencies above about 1000 Hz are most significant.

These absorbers are reported to be effective in eliminating or reducing squeal, 10 dB and above in the curve squeal peak frequencies (Müller, 2003).

In Queensland, shark fin dampers fitted to some passenger rolling stock have been successful in reducing squeal (Anderson, 2008b). This type of wheel (SMU220 wheel) with shark fin damper is supplied by OneSteel Ltd in Australia (Skerman, 2011).

(4) Advantage:

By appropriately tuning the dampers, either the bending or radial modes of the wheel can be damped thus optimizing noise reduction for curve squeal or rolling noise. The absorbers are reusable, that is, they can be removed from worn wheels and mounted onto new ones.

(5) Disadvantage:

Tuned mass dampers convert vibration energy to heat using visco-elastic elastomers, which are themselves affected by temperature. However, no data is available concerning the performance of tuned mass dampers at low or very low temperatures. A special elastic mounting ring is needed to accommodate the thermal expansion of the rim and protect the tuned mass damper from thermal damage.

The tuned mass dampers need to be tuned on the specific wheel eigenmodes. This treatment is expected to be dependent on the wheel rim thickness which is modified as a normal wheel maintenance practice. There is evidence of significant changes in modal frequencies between wheel types and as wheels undergo re-machining as part of the normal maintenance cycle. For example,

Figure 2-12 indicates that for one mode the shift was from 4079 to 3501 Hz as the wheel progressed from new to scrap diameter. This has to be considered in determining the viability of a treatment.

However, it should also be noted that the tuned mass damper is different to the undamped tuned resonator or “dynamic absorber”, which functions as discrete tuned resonant energy transfer devices. Tuned mass dampers dissipate energy; are effective over a range of frequencies; and, in some cases a single damper can be effective in controlling the response of the wheel in several modes of vibration.

It remains a problem that the design of the tuned mass damper is wheel-dependent, since it must be designed for pre-determined wheel natural frequencies.

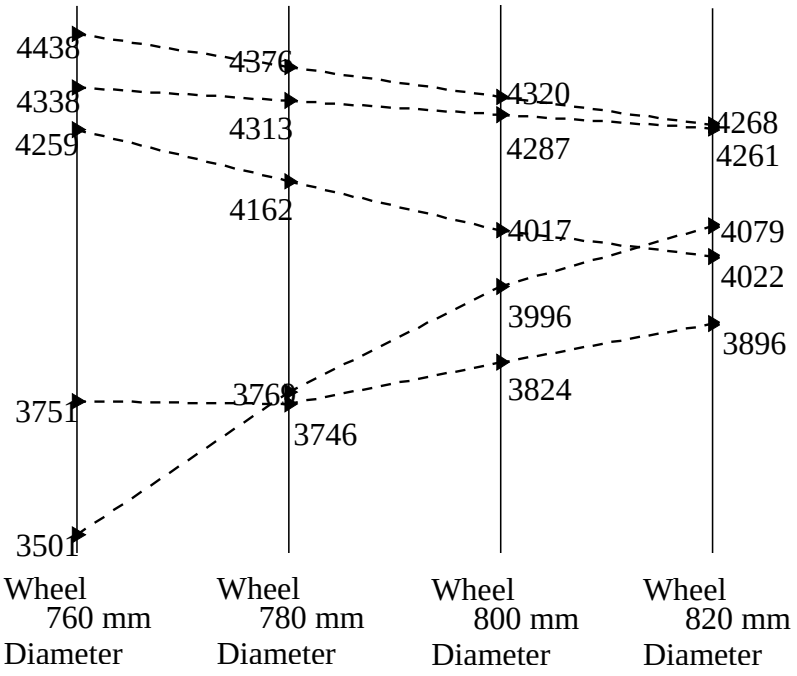

Figure 2-12 shift of the eigenfrequencies [Hz] due to the reduction of the wheel diameter (Cataldi-Spinola, 2003)

(6) Commercial product:

Several commercial products are available and have been in operation for years, especially in metro lines (Müller, 2003; bochumer-verein, 2011; Schrey & Veit GmbH, 2011). VSG wheel dampers have been applied in various Light Rail vehicles according to the information from the manufacturer. The wheel absorbers on monobloc wheels, made by Schrey & Veit GmbH, have been applied in Switzerland (Panorama vehicles of MOB), Germany (S-Bahn Berlin) as well as light rail (DT8.10 of SSB) and the bayrische Zugspitzbahn.

2.5.3 Constrained layer damping treatment

(1) Description:

Constrained layer damping treatment consists of a steel or aluminum layer constraining a viscoelastic high damping polymer sheet (internal and/or external) glued onto the wheel web, as shown in Figure 2-13.

(2) Mechanism:

Viscoelastic damping is exhibited strongly in many polymeric damping materials. Polymeric materials are made up of long molecular chains. The carbon atoms join strongly together and can be branched so that the long chain can be strongly or weakly linked, according to the composition and processing of the polymer. The damping arises from relaxation and recovery of the polymer network after it has been deformed, and a strong dependence exists between frequency effects and temperature effects because of the direct relationship between material temperature and molecular motion (Nashif, 1985). The dependence of the elastic and viscous properties of the viscoelatic damping material on frequency and temperature is usually represented by its nomogram as shown in Figure 2-14. Usually for railway noise applications, the selection criterion for viscoelastic damping material is firstly based on its large loss factor over relatively wide temperature and frequency range.

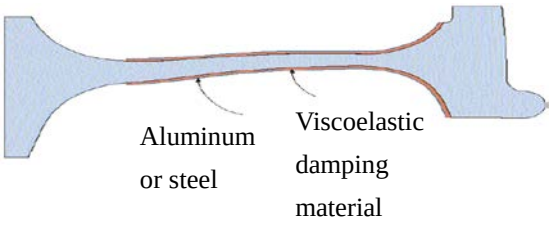

Figure 2-13 Constrained layer damping treatment

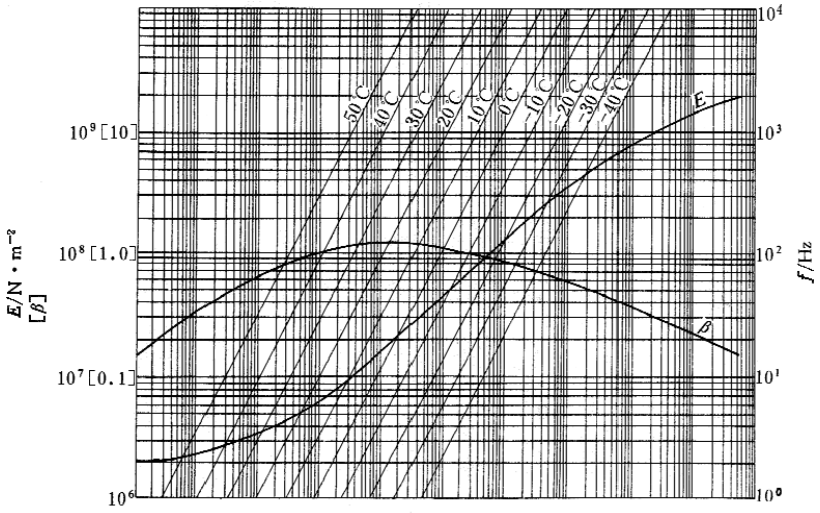

Figure 2-14 Damping polymer property specification of ZN03

When the structure is subjected to cyclic bending, the metal layer will constrain the viscoelastic material and force it to deform in shear. Shear deformation is the mechanism by which the energy is dissipated. For transverse bending of a wheel, maximum bending strain and velocity occur at the tyre. Significant bending of the wheel centre may also be involved, in which case a constrained layer damping treatment would be effective if applied to the web of the wheel (Nelson, 1997).

At low temperatures, where the damping material is in its glassy region, both the structure and the constrained layer become rigidly coupled. In this case, little shear deformation occurs in the middle layer, and hence the energy dissipation is also small. On the other hand, at high temperatures, where the viscoelastic material is in its rubber region and soft, both the structure and constrained layer become almost decoupled. The energy dissipation in this case is also minimal, even though the shear deformation in the middle layer is high.

This is because the shear modulus of the middle layer is low. Between these two extremes, the material possesses an optimal modulus value, so that the energy dissipation for the constrained layer goes through a maximum. The maximum shear deformation in the middle layer is a function of the modulus and the thickness of the constrained layer, the thickness of the damping layer, and the wavelength of vibration in addition to the properties of the damping material (Nashif, 1985). As usual, the temperature is the first parameter of importance with respect to the damping performance of a constrained layer treatment. The maximum damping with temperature occurs in the transition region of the material.

(3) Effectiveness:

Constrained layer damping treatments have been used effectively to increase the damping of wheels and thereby eliminate squeal.

Squeal reductions of 7~24 dBA when new, and 11~18 dBA after 17 months have resulted for Soundcoat Co. constrained layer damping treatments (Nelson, 1997). It consists of a layer of DYAD damping treatment adhered to the side of the rim of the wheel and constrained with a steel angle rolled into a ring, with positive mechanical retention.

In the UK, Constrained layer damping treatments, made by Heathcote Industrial Plastics, have been applied to the wheels of tread-braked multiple unit trains since the late 1980s to prevent curve squeal (Thompson, 2009). Measurements showed that the squeal noise was eliminated. For tread-braked wheels, constrained layer damping can only be applied to the wheel web, due to the high temperatures reached in the tread region during prolonged periods of drag braking. Under these circumstances, even on the web, the materials have to be capable of surviving temperatures of over 200 ℃ (Thompson, 2009).

In Australia, it is reported that the constrained layer damping treatment supplied by OneSteel Ltd was ineffective in controlling squeal in the Queensland railway network (Skerman, 2011).

(4) Advantage:

The treatment is expected to be equally effective on all wheel eigen-modes related to curve squeal, which usually involve transverse bending of a wheel.

No machining is required in the wheel, and thus there is no stress concentration resulting from modification of the wheel.

(5) Disadvantage:

Constrained layer damping has the drawback of covering a portion of the wheel surface, which interferes with visual inspection of the wheels.

Shrink (hot) fit, which is normally in use to mount the wheels on the axle, cannot be used; cool fit is necessary, as the polymer could not survive to the 200~250 ℃ heating.

This type of damping treatment is generally only possible for disc-braked wheelsets, as block braking introduces too much heat in the wheel tread that is transferred to the wheel web damaging the polymer.

The effective durability of the treatment in real service is still in question, sometimes external panels had some parts that were apparently detached. Besides, the performance of this type of viscoelastic damping treatment is primarily affected by temperature. However, no data have been supplied concerning the performance of viscoelastic damping treatment at high (due to braking) temperatures, or low temperatures in winter.

(6) Commercial product:

The Soundcoat Co. constrained layer damping treatment has evidently been implemented at the Paris Metro and was tested at the MTA NYCT (Nelson, 1997). Constrained layer damping treatments, made by Heathcote Industrial

Plastics, were fitted to the entire passenger fleet Between Llandudno to Blaenau Ffestiniog on the Conway Valley, North Wales, UK (Müller, 2003).

2.5.4 Summary

In terms of mitigating or eliminating curve squeal, various wheel damping devices have been reported as applicable for squeal mitigation (Remington, 1985; Nelson, 1997; Müller, 2003). Each type of wheel damper has its own advantages and disadvantages:

(1) Ring damper is a very economic and effective method of squeal control, but its control effect is unstable due to ring/groove contamination, after commencing operation. The mechanism involved with the ring damper is not currently well understood. Its effectiveness varies without a known reason and so its effect in actual operation is not predictable. A mode coupling mechanism may explain the mechanism of the vibration coupling of the ring damper and the wheel structure, providing new and further insights into the attenuation mechanism (Brunel et al., 2010), since numerical simulations found that friction and impact mechanism (López, 1999; López et al., 2004) can only account for about 1 dB noise and vibration reduction (Brunel et al., 2006), rather than the normally observed 10 dB at a distance of 7 m from the track (Wetta et al., 1985).

(2) The tuned-mass damper has been shown to be effective in eliminating squeal for the pre-defined wheel condition (Remington, 1985; Nelson, 1997; Müller, 2003). However, after re-profiling during normal maintenance, the eigenmodes of the wheel are significantly changed (Cataldi-Spinola et al., 2003), which subsequently affects the required tuned affecting damping effectiveness and thus the noise control effect. The relatively high price of tuned mass dampers and possible safety issues related to cracks initiated from the mounting position also need to be taken into consideration (Nelson, 1997).

(3) The effect on squeal control of the constrained layer damping treatment varies.

They largely depend on the damping characteristics of the viscoelastic material used (Nelson, 1997). The constrained layer damping treatment is exempt from safety issues related to machining of the wheel for mounting, but special considerations are needed for its effective durability (Nelson, 1997; Bracciali et al, 2009). Temperature, humidity, fuel and other harsh conditions during the railway operation all have strong adverse effects on its effective durability. All of them should be taken into account when choosing or developing an appropriate viscoelastic damping material for this kind of damping treatment, due to the sensitivity of the viscoelastic material to the environment (Bracciali et al, 2009).

3. Sensitivity analysis of key bogie parameters on AOA

3.1 Aim and Objective

The research aim is to determine the sensitive bogie parameters or combination of parameters for a specific type of wagon that leads to large AOA (10~30 mrad) when negotiating a tight curve (curve radius ≤ 300 m). The influence and the ranking of importance of bogie parameters and their combination in different worn conditions on wheelset AOA will assist vehicle operators in determining AOA management strategies relevant to bogies.

The objective is to identify effective and efficient AOA control methods. It is suspected that a modification of criteria in current maintenance standard and evidence-based advice on limits or combinations of limits on maintaining the required curving performance.

Given the reported relationship between bogie parameter and AOA, investigation of combinations of parameters is warranted. Here we present a curving dynamics model for the three-piece bogie in worn conditions, using nonlinear curving theory. Potentially important rolling stock parameters are investigated individually to quantify their influence on the wheelset AOA and thus determine their rank on this issue, then several of the most important parameters are combined to investigate the worst case scenario when the largest wheelset AOA occurs. An explanation of the observed AOA behaviour is sought.

3.2 Vehicle dynamics simulation model

3.2.1 Wagon parameters

The AOA distribution, for the leading axle of the leading bogie, varies significantly as a function of the freight wagon design, or class. For example, the wagon class (Class A as shown in Figure 3-1) has the most passes at the field observation site (3498 out of

33324, more than 10% of the total freight wagon passes), 100% of its 3498 passes are detected within the band of 0-10mrad. The worst-performing wagon class (Class B as shown in Figure 3-1), has in total only 632 passes, 158 had an AOA exceeding 30mrad, making up more than 40% of the wagon passes that exceeded 30mrad. Class A is a radial three-piece bogie design with cross links, while Class B is a conventional three-piece bogie design.

Here, a typical wagon with a typical 70 ton Ride-control three-piece bogie (Class B) was chosen for examining the influence of worn condition of bogie components on large AOA negotiating a tight curve (curve radius = 300 m). A non-linear transient curving simulation has been conducted using the VAMPIRE® software package.

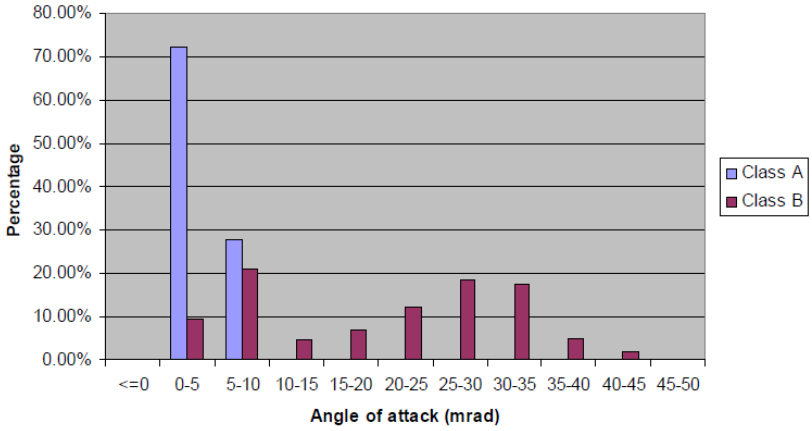

Figure 3-1 A comparison of the AOA (Leading axle of leading bogie) distribution of the best and worst performing freight wagon class (Dwight, Jiang, 2009)

In order to accurately simulate the curving dynamics of this type of wagon, a mathematical model has been built which can consider the coupling dynamics of longitudinal, lateral and vertical movement of the system. This wagon model contains 11 rigid masses, that is, 1 car body, 2 bolsters, 4 sideframes and 4 wheelsets. The degrees-of-freedom of each rigid mass are listed in Table 3-1. The number of DoF used for one wagon is 66.

Table 3-1 Degrees-of-freedom for the simulated wagon

DoF	Longitudinal	Lateral	Vertical	Roll	Pitch	Yaw
Car body	X_c	Y_c	Z_c	Φ_c	θ_c	ψ_c
Sideframe (i=1~4)	X_{sfi}	Y_{sfi}	Z_{sfi}	Φ_{sfi}	θ_{sfi}	ψ_{sfi}
Wheelset (j=1~4)	X_{wj}	Y_{wj}	Z_{wj}	Φ_{wj}	θ_{wj}	ψ_{wj}
Bolster (k=1~2)	X_{bk}	Y_{bk}	Z_{bk}	Φ_{bk}	θ_{bk}	ψ_{bk}

Table 3-2 General parameters of the simulated wagon

Parameter	Value
Mass of car body (full loaded)	82689 kg
Mass moment of inertia of car body about *X* axis (full loaded)	52553 kg·m^2
Mass moment of inertia of car body about *Y* axis (full loaded)	3706100 kg·m^2
Mass moment of inertia of car body about *Z* axis (full loaded)	3741802 kg·m^2
Mass of bolster	587.5 kg
Mass moment of inertia of bolster about *X* axis	234.6 kg·m^2
Mass moment of inertia of bolster about *Y* axis	14.9 kg·m^2
Mass moment of inertia of bolster about *Z* axis	234.2 kg·m^2
Mass of sideframe	354.5 kg
Mass moment of inertia of sideframe about *X* axis	16.4 kg·m^2
Mass moment of inertia of sideframe about *Y* axis	134.5 kg·m^2
Mass moment of inertia of sideframe about *Z* axis	121.9 kg·m^2
Mass of wheelset	1083.2 kg
Mass moment of inertia of wheelset about *X,Z* axis	572.8 kg·m^2
Mass moment of inertia of wheelset about *Y* axis	76.9 kg·m^2
Friction coefficient of centre plate	0.1-0.5
Lateral distance between the left and the right side bearers	1.270 m
Friction coefficient of metal cap of side bearer	0.2- 0.4
Reference preload of side bearer	26.69 kN
Warp stiffness of bogie	0.67-1.05 MN·m/rad
Distance of two bogie mass centres	16.764 m
Lateral distance between the left and the right secondary suspensions	1.980 m
Wheelset base	1.727 m
Wedge angle	0.654 rad
Preload of wedge spring	5.491-9.345 kN
Lateral clearance of bearing adapter	5 mm
Longitudinal clearance of bearing adapter	5 mm
Friction coefficient of bearing adapter	0.4

The key suspension components of the three-piece bogie are the centre plate, side bearers, friction wedges and bearing adapters. All these components are modelled with non-linear spring stiffness and friction damping in the VAMPIRE® model. A detailed list of parameters of the model is presented in Table 3-2.

3.2.2 VAMPIRE model of the suspension components

The centre plate to centre bowl connection is modelled with four vertical VAMPIRE® "bumpstop elements" (non-linear elements) at centre plate edges. It allows the modelling of lift-off of the centre plate and bogie pitch and roll characteristics, which reflects the looseness of the actual centre plate/centre bowl connection. The non-linear characteristics of this bumpstop element are shown in Figure 3-2. Each vertical bumpstop element couples with planar friction elements to account for the effect of dynamic vertical loads on centre bowl rotational friction. In addition, two nonlinear bumpstop elements are used to represent the longitudinal and lateral characteristics with the gap between centre plate and centre bowl rim included.

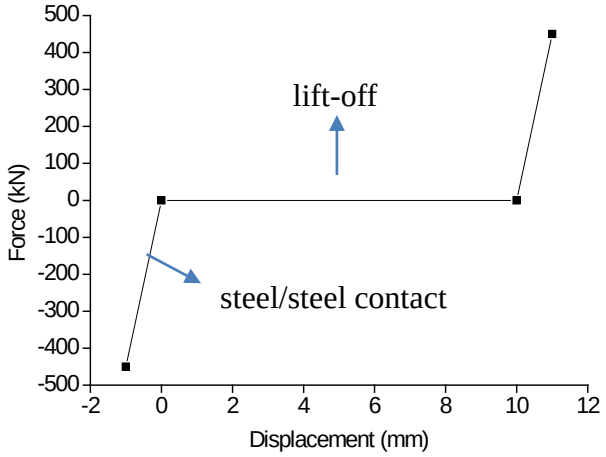

Figure 3-2 Centre plate to centre bowl vertical non-linear connections

The side bearers in this case are modelled for a typical long-travel constant contact side bearer design with a metal cap on top of elastomeric blocks. The spring stiffness characteristics of this long-travel CCSB are shown in Figure 3-3 as plots of vertical force against vertical deflection. It has a preload of approximately 27 kN at setup

height. This is represented by a bumpstop element in the vertical direction. Tangential friction between the metal cap of the CCSB and the wear plate of the carbody underframe in two directions is added by planar friction elements.

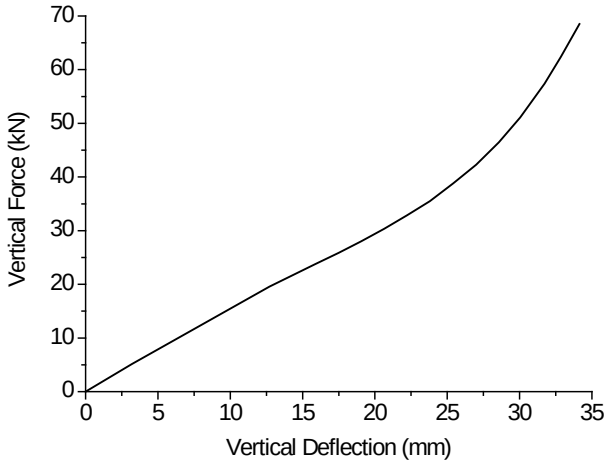

Figure 3-3 Side bearer stiffness characteristics

The model for a friction wedge is built for a ride control bogie design. It contains two perpendicular line friction elements coupled with a constant static load from a wedge spring. These friction elements can model slope and column face friction values, as well as wedge angle by having different effective friction coefficient for the up and down movements of the wedge with column toe-out. This wedge model can link the bogie warping and bouncing of the car interactions at the wedge interface.

The bearing adaptor is modelled with two non-linear springs for the vertical lift-off and nonlinear springs for lateral and longitudinal pedestal gap contact. Planar friction elements are used to model the longitudinal and lateral friction forces between bearing adaptor and pedestal roof.

3.2.3 Track parameters

The track model for this study represents a tight curve for which trackside measurement of AOA is available. The curve radius modelled is 300 m with an 80 m entry transition curve and another 80 m exit transition curve. The full length of the curve used in this study is 200 m and the cant is 120 mm. The total track distance for

simulation is 500 m.

3.3 Simulation cases and analysis of results

Since usually the AOA of the leading wheelset of the leading bogie is the largest, only simulation results of AOA from that wheelset are compared in this report. Simulation cases are separated into two major parts: part one is to investigate the influence of the individual bogie parameter on the leading wheelset AOA; after major influencing parameters are identified, part two is to investigate the combination of these parameters causing the largest wheelset AOA. All curving simulations are conducted on a fully loaded wagon, as this condition generally has worse curving performance than the empty wagon. The running speed of the loaded wagon in all simulations is set at 36 km/h. The new ANZR wheel profile and new AS1085 60 kg/m rail profile are used in all cases.

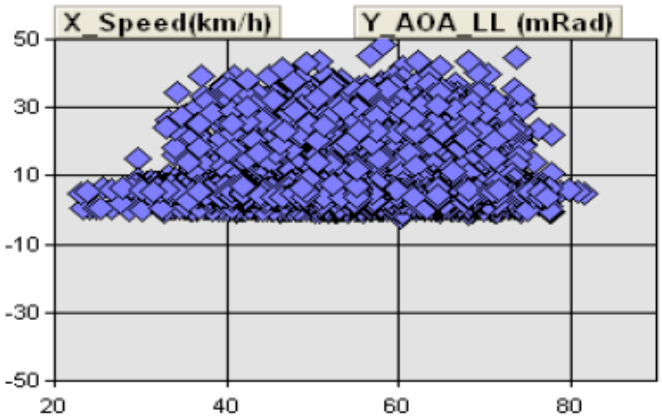

Figure 3-4 4axle freight vehicles, AOA of the leading axle, leading bogie (Dwight, Jiang, 2009)

In these simulations, the curve radius is 300 m and the cant is 120 mm, thus the balance speed of curving is 55 km/h. The curving speed in our simulation cases is chosen to be 36 km/h, which results in a cant excess of 68.4 mm for a cant of 120 mm. In our early testing simulation case of higher running speed of 60 km/h and in comparison with the 40 km/h case, a similar trend to the one shown in Figure 2-4 (Simson, 2006e) is obtained, that is, about a 2 mrad increase is due to this level of cant

excess. This 2 mrad difference is considered to be insignificant in regard to the large increase of AOA from normally below 10 mrad to 30 mrad (Dwight, Jiang, 2009). The running speed of the freight wagons ranges from 40 km/h to 60 km/h in the field monitoring data. As shown in Figure 3-4, increasing speed to balance speed for freight wagon to avoid excessive cant seems unable to improve AOA performance. Since we tend to investigate the worst case scenario of AOA, cant excess is introduced as the default case at the beginning.

3.3.1 Individual bogie parameter investigation

The parameters investigated here can be divided into three main categories:

- **Parameters controlling turning moment between carbody and bolster**: that is, centre bowl friction level, setup height of constant contact side bearer (CCSB), and friction coefficient of the metal cap of CCSB. Under full load from the carbody, this turning moment will potentially reach its maximum. It will strongly depend on the carbody load distribution through centre bowl and CCSB to bogie bolster, as well as friction level of centre bowl and CCSB contact interfaces.

  (1) Based on Equations 2-2 and 2-3, three equivalent friction coefficients of centre bowl are considered: 0.1 for a lubricated centre bowl, 0.33 for a dry, new centre bowl in full contact, and 0.5 for a dry, worn centre bowl with rim contact. A dry, new centre bowl in full contact is set as the reference case.

  The associated simulation results of the AOA are shown in Figure 3-5. Centre bowl lubrication can improve AOA by 2.95 mrad, while AOA under a worn centre bowl with rim contact condition deteriorating by 4.62 mrad, compared with that of a dry, new centre bowl in full contact condition.

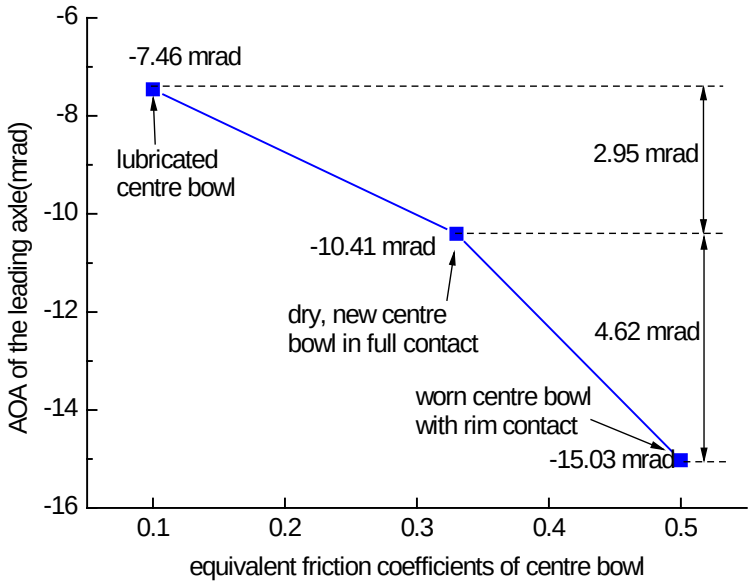

Figure 3-5 AOA of the leading wheelset by varying centre bowl friction

(2) Three different friction coefficients of the metal cap of the CCSB are considered: 0.2, 0.4, 0.6 with the '0.4' case as the reference case.

The associated simulation results of the AOA of the leading wheelset in the leading bogie are shown in Figure 3-6. Decreasing this friction coefficient from 0.4 to 0.2 AOA can improve AOA by 1.68 mrad, while increasing from 0.4 to 0.6, AOA deteriorates by 1.98 mrad, compared to that of the '0.4' reference case.

(3) Three different setup heights of the CCSB are considered: a standard setup height of 5-1/16 inches (128.6 mm) suggested by the manufacturer, that is, CCSB preload of 26.7 kN; the manufacturer recommended minimum setup height of 5 inches (127 mm), that is, CCSB preload of 28.8 kN; and a setup height of 4-15/16 inches (125.4 mm), that is, CCSB preload of 31.5 kN. A regular setup height of 5-1/16 inches is set as the reference case.

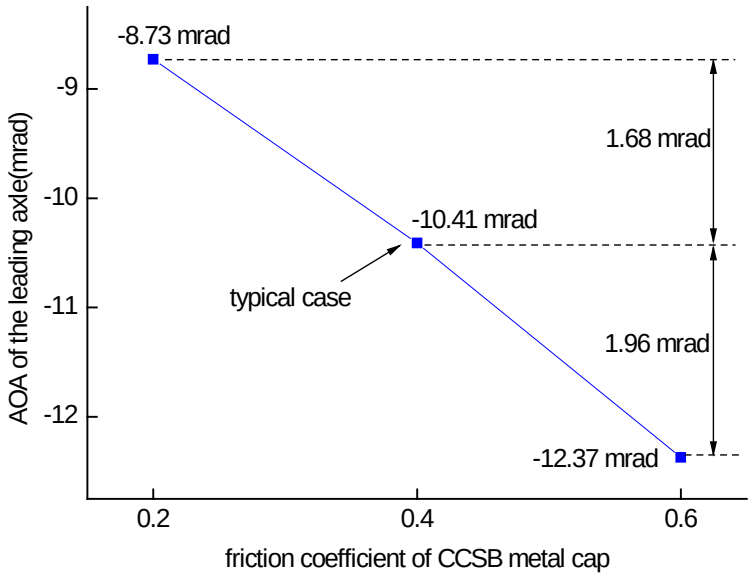

Figure 3-6 AOA of the leading wheelset by varying the friction coefficient of CCSB metal cap

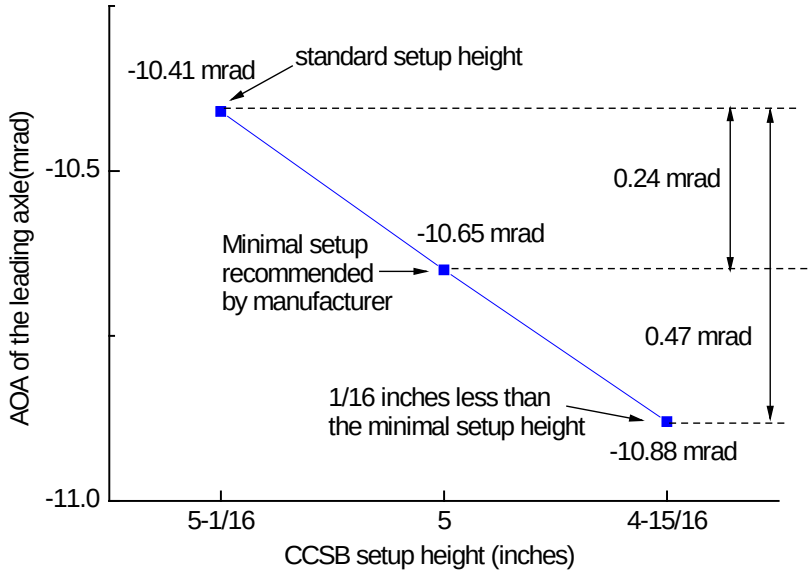

Figure 3-7 AOA of the leading wheelset by varying CCSB setup height

The associated simulation results of the AOA of the leading wheelset in the leading bogie are shown in Figure 3-7. When the setup height is within the manufacturer's recommended range (from 5-1/16 to 5 inches), AOA increases very slightly by 0.24 mrad; by further decreasing to 4-15/16 inches, the AOA increase rate stays much the same with its value increasing by only 0.47 mrad, compared to that of the standard setup height case.

Actually, AAR Rule 60 specifies that a minimum set-up height of 4-7/8 inches should be maintained for constant contact designs. Based on the simulation results, it is predicted that the increased rate of AOA with respect to CCSB setup height will stay much the same in this setup height range as well.

- **Parameters controlling warp moment between bolster and sideframes**: Hawthorne (1990) reports testing of warp stiffness for this type of bogie. The associated simulation results of the AOA of the leading wheelset in the leading bogie are shown in Figure 3-8. The difference of AOA between new wedge condition and half-worn wedge condition is 0.66 mrad, while the difference of AOA between new wedge condition and fully-worn wedge condition is 1.77 mrad.

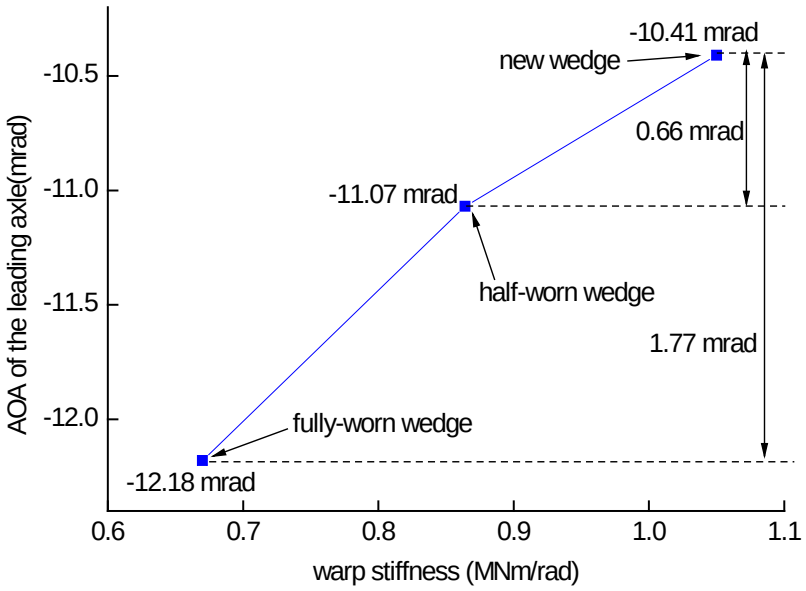

Figure 3-8 AOA of the leading wheelset by varying warp stiffness

- **Parameters affecting wheelset steering moment**: while hollow wheel profiles to varying depths has not been investigated, the effect of rail gauge corner lubrication on wheelset AOA is investigated here, as recent field trials (Jiang, Dwight, 2013) showed that rail gauge corner lubrication indicated a significant reduction in the occurrence of the freight wagon squeal events. Here for the rail

gauge corner lubrication case, the friction coefficient of both rail gauge corners is reduced from 0.3 to 0.15, while the friction coefficient of the rail head stays the same at 0.3. The simulation shows that under gauge lubrication the leading wheelset AOA increases from -10.41 mrad to -13.29 mrad. The difference is 2.88 mrad.

- **Short summary in individual parameter investigation**

  From the discussion above, it can be concluded that for this type of wagon and summarized in Table 3.3. It can be found that the biggest influencing parameter of turning moment generated between the carbody and the bolster on AOA is the equivalent friction coefficient of the centre bowl (AOA difference is -2.95 ~ 4.62 mrad). The second most important parameter is the friction coefficient of the CCSB metal cap (AOA difference is -1.68 ~ 1.96 mrad), while the setup height of the CCSB investigated shows negligible influence on the AOA (AOA difference is 0.24 ~ 0.47 mrad).

Table 3-3 Parameters variations of the simulated wagon

bogie parameters	parameter value		leading wheelset AOA (mrad)		
	typical value	range	range	typical value	AOA difference
equivalent friction coefficients of centre bowl	0.33	0.1~0.5	-7.46 ~ -15.03	-10.41	-2.95 ~ 4.62
friction coefficient of the ccsb metal cap	0.4	0.2~0.6 (assumed)	-8.73 ~ -12.37	-10.41	-1.68 ~ 1.96
setup height of ccsb	5-1/16 inches	5-1/16 ~ 4-15/16 inches	-10.41 ~ -10.88	-10.41	0.24 ~ 0.47
warp stiffness	1.05 mnm/rad	0.67~1.05 mnm/rad	-10.41 ~ -12.18	-10.41	0.66 ~ 1.77
gauge corner lubrication	0.15	compared with 0.3 (dry rail)	-10.41 ~ -13.29	-10.41	2.88

The biggest influencing parameter of warp moment generated between bolster and sideframes on AOA is the warp stiffness between sideframes and bolster

from the constant frictional rubbing of the wedge against the pocket and column wear plate. The differences of AOA in different wedge worn conditions range from 0.66 ~ 1.77 mrad. By affecting the wheelset steering moment, gauge corner lubrication can increase the leading wheelset AOA by 2.88 mrad.

On the other hand, hunting stability requires the friction coefficient of the CCSB to be relatively high. No lubrication of the CCSB metal cap is allowed. As a result, it seems that the most important parameters are the worn condition of the centre bowl and warp stiffness change due to wedge worn condition. In the next section, the combination of major influencing bogie parameters will be further investigated.

3.3.2 Combinations of major influencing bogie parameters investigation

- **Combinations of different centre bowl friction levels and warp stiffness**

  Given the range of feasible centre bowl friction levels and warp stiffness set out in Section 3.3.1, a study of different combinations of values of these two parameters has been explored using the model developed. The resulting AOA for the various combinations investigated are presented in Figure 3-9.

  From Table 3.4, the influences of centre bowl friction on leading wheelset AOA under different warp stiffness are investigated. It is shown that under a new wedge condition, the increasing rate of leading wheelset AOA is the smallest, that is, every increment of 0.1 of centre bowl friction, AOA increases by 1.155 mrad on average; while under half-worn wedge and fully-worn wedge conditions, that average value is 1.685 mrad, and 1.775 mrad respectively. The influences of centre bowl friction levels on leading wheelset AOA increases as the warp stiffness decreases.

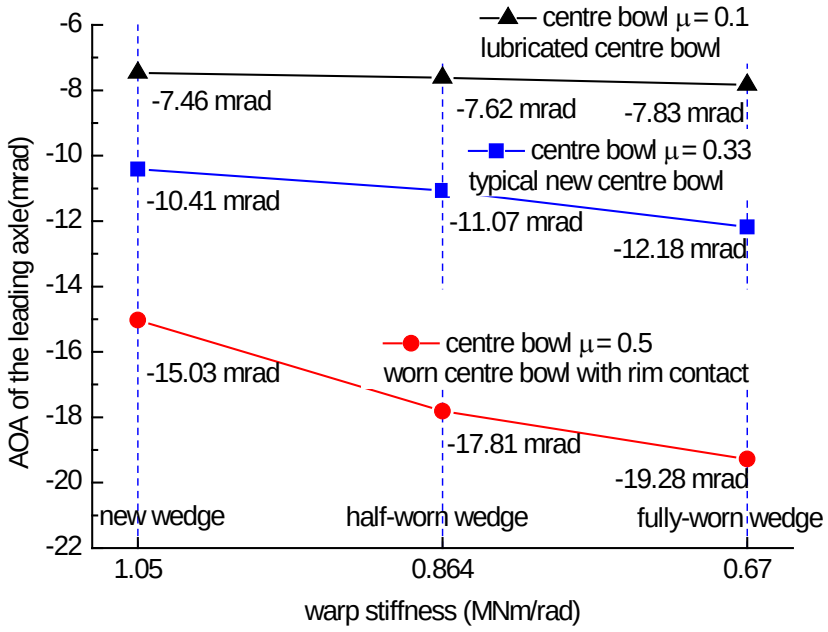

Figure 3-9 AOA of the leading axle by varying warp stiffness and centre bowl friction

The influences of warp stiffness, as indicated by wedge rise, on leading wheelset AOA under varying centre bowl friction is presented in Table 3.5. It is shown that for the lubricated-centre-bowl condition, the increasing rate of leading wheelset AOA is the smallest, that is, every increment of 7/16 inch (11 mm) of wedge rise, AOA increases by 0.105 mrad on average; while under half-worn wedge and fully-worn wedge conditions, that average value is 0.555 mrad, 0.735 mrad, respectively. The influences of warp stiffness on leading wheelset AOA increases as the centre bowl friction level increases.

The results show that the friction coefficient of the centre bowl has a more significant influence on AOA of the leading wheelset than does the warp stiffness. The less the warp stiffness is, the higher AOA for the same centre bowl friction level. In the well lubricated centre bowl case, the warp stiffness has a relatively small influence on AOA, while as the centre bowl friction level increases, the controlling effect of warp stiffness on the AOA of the leading axle increases significantly.

As expected, the most severe case of large leading wheelset AOA (-19.28 mrad) occurs with highest centre bowl friction level and lowest warp stiffness. Conversely, the best case of small leading wheelset AOA (-7.46 mrad) occurs with lowest centre bowl friction level and highest warp stiffness. This represents a variation of approximately 12 mrad.

Table 3-4 Influence of centre bowl friction on leading wheelset AOA under different warp stiffness

wedge condition	AOA difference between new and lubricated centre bowl cases	AOA difference between worn and new centre bowl cases	AOA difference between worn and lubricated centre bowl cases
new wedge (wedge rise=0)	2.95 mrad	4.62 mrad	7.57 mrad
half-worn wedge cases (wedge rise=1/2 inch)	3.45 mrad	6.74 mrad	10.19 mrad
fully-worn wedge cases (wedge rise=7/8 inch)	4.35 mrad	7.1 mrad	11.45 mrad

Table 3-5 Influence of warp stiffness on leading wheelset AOA under centre bowl friction

centre bowl condition	AOA difference between half-worn and new wedge cases	AOA difference between fully-worn and half-worn wedge cases	AOA difference between fully-worn and new wedge cases
lubricated centre bowl (equivalent friction coefficient=0.1)	0.16 mrad	0.21 mrad	0.37 mrad
new metal-metal centre bowl in full contact (equivalent friction coefficient=0.5*2/3=0.33)	0.66 mrad	1.11 mrad	1.77 mrad
worn centre bowl with rim contact (equivalent friction coefficient=0.5)	2.78 mrad	1.47 mrad	4.25 mrad

(2) Worst scenario leading to largest wheelset AOA

The worst case scenario for the leading wheelset AOA is -23.63 mrad, with the combination by setting highest effective friction coefficient of the centre bowl

as 0.5, lowest warp stiffness as 0.67 MNm/rad, associated wedge spring preload as 5.49 kN, CCSB friction coefficient as 0.6 (increased from typical value 0.4), flange/gauge corner contact friction coefficient as 0.15.

3.4 Summary

From simulation results of the leading wheelset AOA of the leading bogie presented above, for this type of fully-loaded wagon negotiating a 300 m radius curve at a speed of 36 km/h, the importance rank of individual bogie parameters on AOA from the most importance to the least is:

1. equivalent friction coefficient of the centre bowl,
2. friction coefficient of the CCSB metal cap,
3. warp stiffness between sideframes and bolster,
4. setup height of CCSB.

The influence of centre bowl friction levels on AOA increases as the warp stiffness decreases. The influence of warp stiffness on AOA increases as the centre bowl friction level increases. The friction coefficient of the centre bowl has a more significant influence on AOA than that of warp stiffness.

The worst combination of bogie parameters in regards to AOA is high centre bowl friction level combined with low warp stiffness. In this combination, AOA can reach -19.28 mrad. If further setting the CCSB friction coefficient from 0.4 to 0.6, the value increases to -19.96 mrad, which means the CCSB friction coefficient has a very limited effect in the worst case AOA scenario; besides the preload of CCSB investigated in the worst case scenario has a negligible contribution to AOA as well. Moreover, if rail gauge corner lubrication applies, this result can further increase to -23.63 mrad, which is in line with the AOA field observation in field trials.

4. Curve squeal model for wheel-rail contact

4.1 Introduction

The aim of the work presented in this chapter is to contribute to the understanding of curve squeal by building a detailed frequency-domain FEM model for wheel-rail curving contact and considering a different squeal mechanism - the coupling of degrees-of-freedom in normal and tangential directions. Under this squeal mechanism, it is possible that squeal would occur in the case of the constant friction coefficient between the wheel and rail contact interface. The model covers the prediction of squeal noise occurrence of the detailed wheel-rail models by searching unstable system eigenvalues in the frequency domain in an efficient manner, but it does not include actual vibration amplitude or sound radiation from the wheel.

ABAQUS provides a complex eigenvalue solution for the stability analysis of friction-induced vibration problems. This capability uses direct coupling at the contact interface described by Ouyang et al. (2005) in automotive disc brake analysis, and Chen et al. (2010) in wheelset-track system rail corrugation analysis.

4.1.1 Brief theory introduction of complex eigenvalue analysis

The governing equation of the system is

$$\boldsymbol{M}\ddot{\boldsymbol{x}} + \boldsymbol{C}\dot{\boldsymbol{x}} + \boldsymbol{K}\boldsymbol{x} = \boldsymbol{0} \tag{4.1}$$

where $\boldsymbol{M}$ is the mass matrix, $\boldsymbol{C}$ is the damping matrix, which includes friction-induced components, and $\boldsymbol{K}$ is the stiffness matrix, which is also asymmetric due to friction. The eigenvalue equation of Equation 4.1 is given as follows

$$(\lambda^2\boldsymbol{M} + \lambda\boldsymbol{C} + \boldsymbol{K})\boldsymbol{\Phi} = \boldsymbol{0} \tag{4.2}$$

where λ is the eigenvalue and $\boldsymbol{\Phi}$ is the corresponding eigenvector. Both eigenvalues and eigenvectors may be complex. In order to solve the complex eigenvalue problem, this system is first symmetrized by ignoring the damping matrix $\boldsymbol{C}$ and the asymmetric contributions to the stiffness matrix $\boldsymbol{K}$. Then this symmetric eigenvalue problem is solved to find the projection subspace. The N eigenvectors obtained from the

symmetric eigenvalue problem are expressed in a matrix as [$\boldsymbol{\Phi_1}$, . . . , $\boldsymbol{\Phi_N}$]. Next, the original matrices are projected onto the subspace of *N* eigenvectors

$$\boldsymbol{M}^* = [\boldsymbol{\Phi_1}, \dots, \boldsymbol{\Phi_N}]^{\mathrm{T}} \boldsymbol{M} [\boldsymbol{\Phi_1}, \dots, \boldsymbol{\Phi_N}] \tag{4.3}$$

$$\boldsymbol{C}^* = [\boldsymbol{\Phi_1}, \dots, \boldsymbol{\Phi_N}]^{\mathrm{T}} \boldsymbol{C} [\boldsymbol{\Phi_1}, \dots, \boldsymbol{\Phi_N}] \tag{4.4}$$

and

$$\boldsymbol{K}^* = [\boldsymbol{\Phi_1}, \dots, \boldsymbol{\Phi_N}]^{\mathrm{T}} \boldsymbol{K} [\boldsymbol{\Phi_1}, \dots, \boldsymbol{\Phi_N}] \tag{4.5}$$

Then the projected complex eigenvalue problem becomes

$$(\lambda^2 \boldsymbol{M}^* + \lambda \boldsymbol{C}^* + \boldsymbol{K}^*) \boldsymbol{\Phi}^* = 0 \tag{4.6}$$

Finally, the complex eigenvectors of the original system can be obtained by

$$\boldsymbol{\Phi} = [\boldsymbol{\Phi_1}, \dots, \boldsymbol{\Phi_N}]^{\mathrm{T}} \boldsymbol{\Phi}^* \tag{4.8}$$

4.1.2 Instability indicators in complex eigenvalue analysis

The complex eigenvalue λ, can be expressed as $\lambda = \alpha \pm i\omega$, where α is the real part of λ, Re(λ), indicating the stability of the system, and ω is the imaginary part of λ, Im(λ), indicating the mode frequency. The generalized displacement of the wheel-rail system, *x*, can then be expressed as

$$x = Ae^{\lambda t} = e^{\alpha t}(A_1 \cos \omega t + A_2 \sin \omega t) \tag{4.9}$$

This analysis determines the stability of the system. When the system is unstable, the real part of the complex eigenvalue, α, becomes positive and squeal occurs. Moreover, an effective damping ratio is defined as $-\alpha/(\pi|\omega|)$. If the effective damping ratio is negative, the system becomes unstable, and vice versa.

4.2 Squeal prediction model

4.2.1 Four key analysis steps

Here, the complex eigenvalue analysis capability in ABAQUS is applied to study vibration instability of the wheel-rail system. The main procedure for using ABAQUS to perform the complex eigenvalue analysis of the wheel-rail system is given as follows:

STEP 1 Initial nonlinear static analysis of the wheel-rail system under small load,

STEP 2 Nonlinear static analysis of the wheel-rail system under full axle load,

STEP 3 Nonlinear static analysis under constant sliding friction between wheel and rail,

STEP 4 Normal mode analysis to extract natural frequencies without friction coupling,

STEP 5 Complex eigenvalue analysis that incorporates the effect of friction coupling.

4.2.2 Finite element mesh

As shown in Figure 4-1, this model contains detailed 3D FEM models of a typical Australian freight wheel with flat tread and an AS60kg rail which has 4 spans. The whole structure is meshed with hexahedral and tetrahedron solid elements. The wheel has conformal mesh while the rail contains two parts, with one dense mesh part in the contact zone connecting to the sparse mesh part using ABAQUS surface-to-surface tie constraints to maintain translational DOFS consistence on the adjacent unconformable meshing surfaces. The average mesh size of the coarse parts ranges from 10-20 mm while that of the dense contact regions is 1 mm.

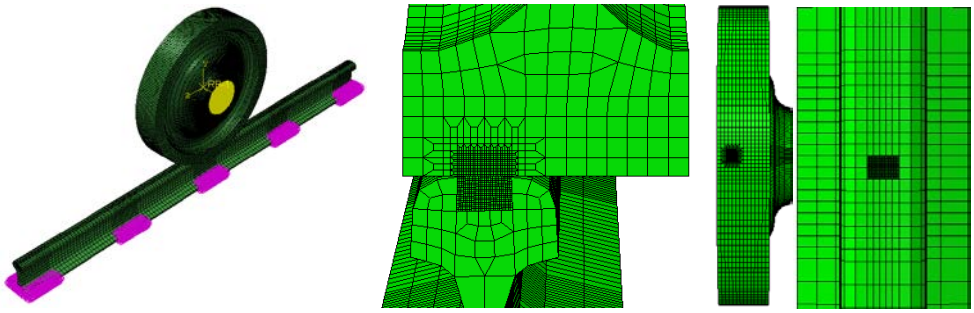

Figure 4-1 Wheel and rail FEM model

4.2.3 Boundary condition and wheel-rail interaction

Symmetric boundary conditions about the plane of rail cross section are applied to both rail ends. The distance between two adjacent sleepers is 600 mm. The width of sleepers is 180 mm. The rails are supported by a group of lateral and vertical springs and dashpots at each position of sleeper. Wheel modal damping is not considered in all cases. The number of lateral or vertical springs and dashpots in each group is the same as the number of rail nodes on the contact interface between the rail and the sleeper. The rail contact center is kept in the symmetrical center of the rail cross section in all

cases.

For constraint, there is one kinematic coupling constraint between a reference node on the wheel axle line and all the nodes around the inner cylinder of the wheel hub. Kinematic coupling constrains the motion of the coupling nodes to the rigid body motion of the reference node.

For load conditions, in STEP 1, a small load of 100 N is applied to the reference node on the wheel axle line in the vertical direction, in STEP 2, this load is replaced with the full axle load of 65 kN.

For wheel-rail interaction, in STEP 1, initial frictionless contact is established under small load; in STEP 2, frictionless contact is established under full axle load; in STEP 3, the frictionless contact state changes into the friction contact state using the keyword *CHANGEFRICTION. Meanwhile, the wheel moves relatively to the rail in a constant sliding speed to simulate a lateral and longitudinal sliding friction condition using the *MOTION card.

4.2.4 Nominal parameters of the wheel-rail system

The density of the wheel and rail material is 7800 kg/m^3. The Young's modulus of the wheel and rail material is 2.1×10^{11} N/m. The vertical stiffness and the lateral stiffness of the rail support spring are 5.88×10^7 N/m and 2.94×10^7 N/m, respectively. The dashpots in parallel with each rail support spring, which represent the rail pad vertical damping and the rail fastener lateral damping respectively, is set to zero.

4.3 Simulation cases and analysis of results

Different wheel diameters and wheel lateral shifts are considered in the following case study. The wheel-rail friction coefficient ranges from 0.1 to 0.6 in intervals of 0.1, with 0.6 as the reference value. The wheel diameter ranges from 840 mm to 780 mm, in intervals of 20 mm, with 800 mm as the reference value, while the wheel lateral shifts range from 0 mm to 30 mm in intervals of 10 mm from the nominal wheel-rail contact point, with 20 mm lateral shift case as the reference case.

4.3.1 Wheel-rail contact state check

As shown in Figure 4-2, the wheel-rail contact Von Mises stress result takes a good elliptical shape which confirms the Hertz contact theory. In Figure 4-3, over the whole contact patch, shear stress takes an oval shape which is representative in the constant sliding case where all nodes inside the contact patch are in the full slippage state.

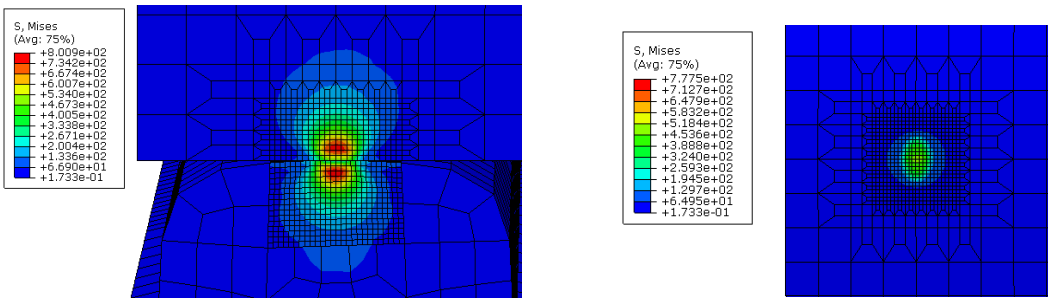

Figure 4-2 Wheel-rail Von Mises stress (MPa) before friction applied

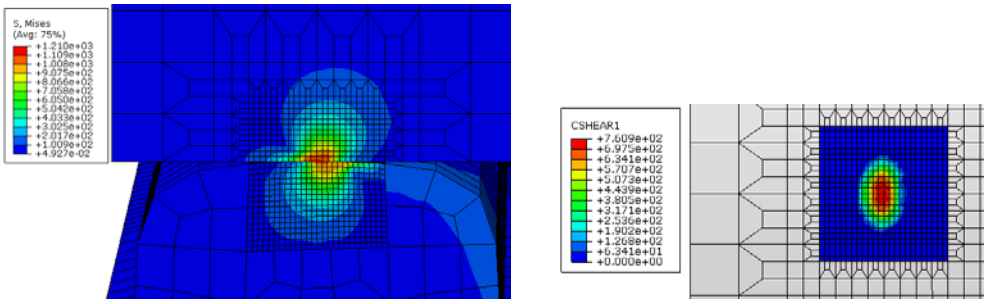

(a) Von Mises stress **(b) shear stress**

Figure 4-3 Wheel-rail contact stress (MPa) after friction applied

4.3.2 Normal mode classification

In the normal mode extraction and complex eigenvalue analysis, the eigenvalues and corresponding eigenmodes have been calculated up to 5500 Hz. The out-of-plane bending modes of the wheel are characterized by nodal diameters (a line of stationary points), *n*, and the numbers of node circles (a circle of stationary points), *m*. The mode with n nodal diameters and m nodal circles will be denoted mode (*n*,*m*). For the in-plane radial modes in the frequency range of interest, *m* is zero, these modes will be referred to as (*n*,r) (Thompson, 2009). A sample classification of the wheel normal modes is listed in Appendix I.

4.3.3 Influence of the friction coefficient on squeal

The wheel-rail friction coefficient ranges from 0.1 to 0.6. The associated simulation results of the unstable modes are shown in Figure 4-4. In the present work, only those modes whose effective damping ratios are less than -0.001 are given. It needs to be noted that if an effective damping ratio is not less than -0.001, its corresponding unstable vibration is considered unlikely to occur. As we can see, squeal starts to appear when the wheel-rail friction coefficient is equal to or above 0.3. In the typical wheel-rail friction coefficient range of 0.3 – 0.4 usually used in vehicle curving dynamics simulation, the squeal modes are modes involving a strong wheel vibration participation of (2,0) bending mode at around 510 Hz, and (0,1) bending mode at around 630 Hz. When the friction coefficient rises to 0.5, an unstable involving strong wheel vibration participation of (3,0) bending mode at around 1145 Hz appears with a negative damping of -0.004. It becomes much more unstable indicated by a negative damping of -0.041 when the friction coefficient reaches 0.6. Alternatively, when the positive real part of the system complex eigenvalues is used as the criterion, as shown in Figure 4-5, a similar pattern could be traced. These modes all involve wheel bending modes with significant wheel rim vibration in the lateral direction, and are shown in Figure 4-6.

Overall, (1) when the friction coefficient ranges from 0 to 0.2, there is no unstable mode shown, which is in line with good squeal control performance of the wheel-rail interface lubrication; (2) when the friction coefficient ranges from 0.3 to 0.5, the most unstable mode with a negative damping ratio of -0.024 to -0.037 is the one involving a strong wheel vibration participation of (0,1) bending mode at around 630 Hz. (3) When the friction coefficient reaches 0.6, two modes – (3,0) bending mode around 1145 Hz and (0,1) bending modes around 630 Hz – become equally unstable as indicated by the negative damping ratio of around -0.04.

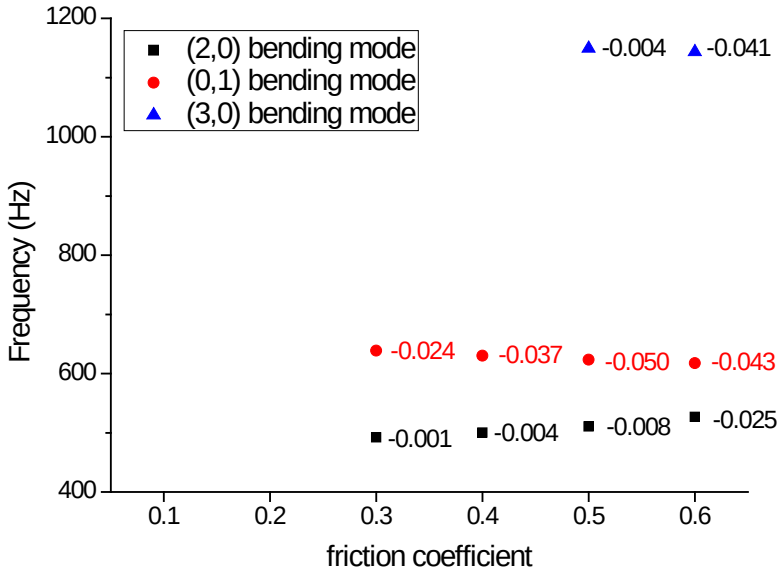

Figure 4-4 Unstable modes distribution under varied wheel-rail friction coefficient – effective damping ratio

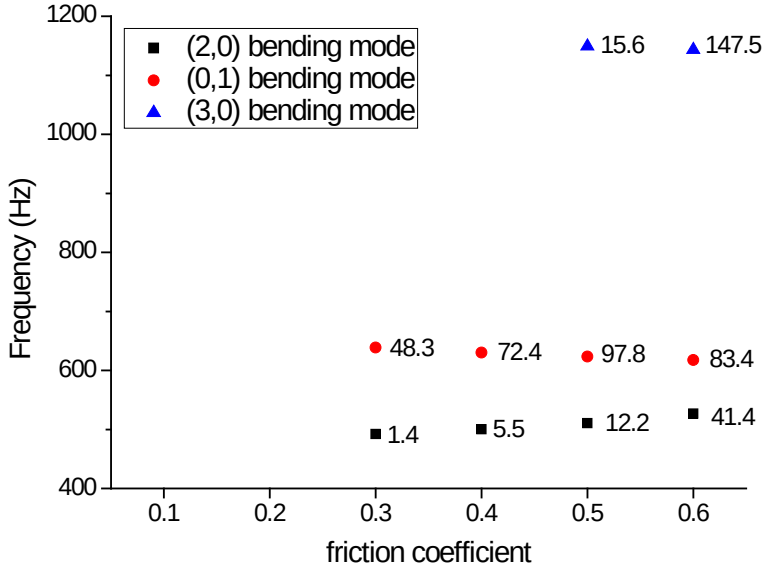

Figure 4-5 Unstable modes distribution under varied wheel-rail friction coefficient – real part

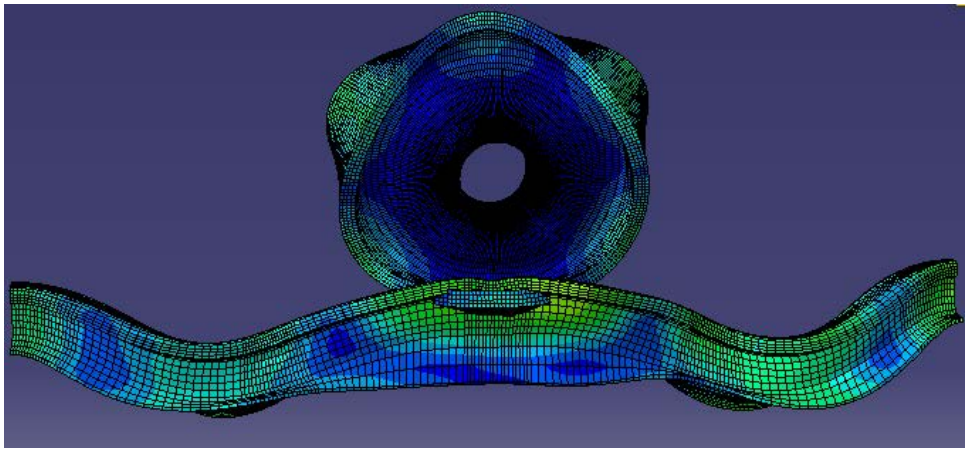

(a) Unstable mode involving wheel (3,0) bending mode around 1145 Hz

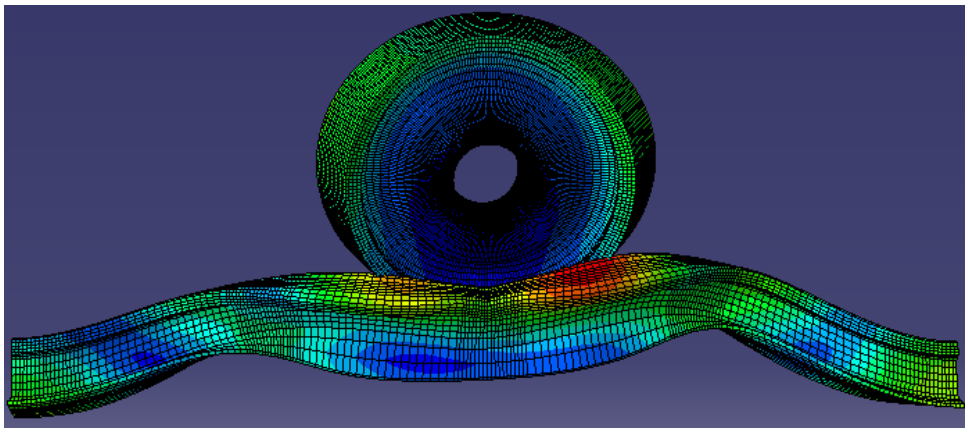

(b) Unstable mode involving wheel (0,1) bending mode around 630 Hz

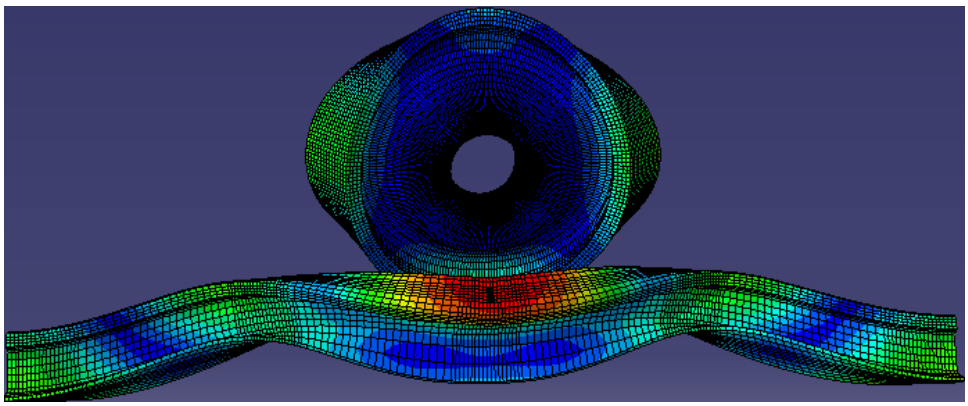

(c) Unstable mode involving wheel (2,0) bending mode around 510 Hz

Figure 4-6 Unstable modes under varied wheel-rail friction coefficient

4.3.4 Influence of the wheel rim thickness on squeal

The wheel diameter ranges from 840 mm for the new wheel to 780 mm for the fully worn wheel. The associated simulation results of the unstable modes are shown in

Figure 4-7 and Figure 4-8. As we can see, from right to left, the wheel diameter decreases. This usually occurs due to regular reprofiling to restore the wheel profile, and hence gradually reduces the thickness of the wheel rim, and the potentially unstable mode number gradually increases. However, the most unstable frequency in different wheel diameters varies and does not remain nearby only one type of wheel mode consistently.

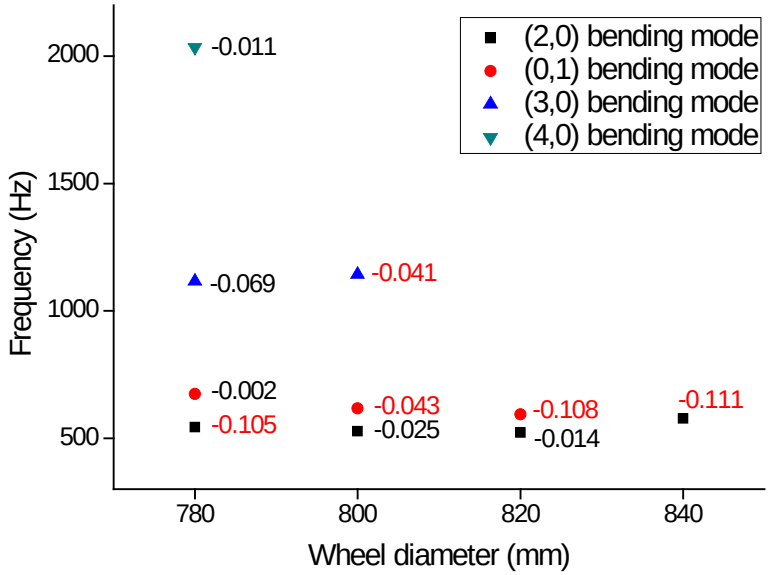

Figure 4-7 Unstable modes distribution under varied wheel diameter – effective damping ratio

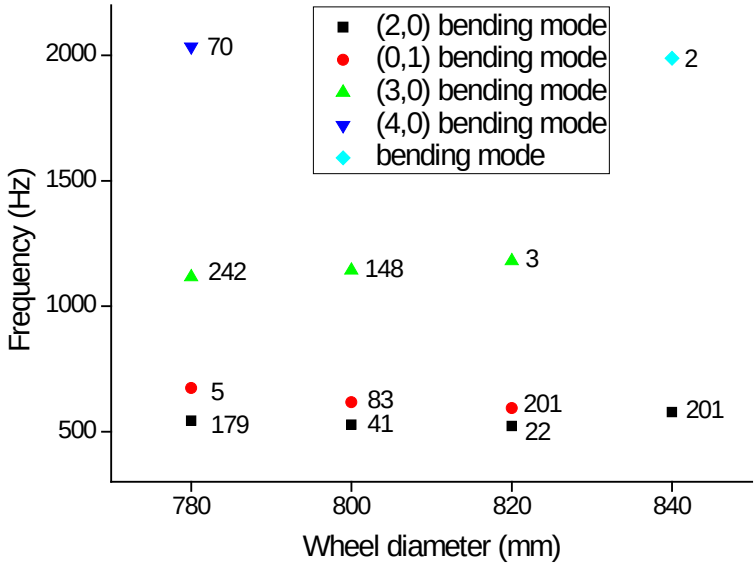

Figure 4-8 Unstable modes distribution under varied wheel diameter – real part

4.3.5 Influence of the lateral shift on squeal

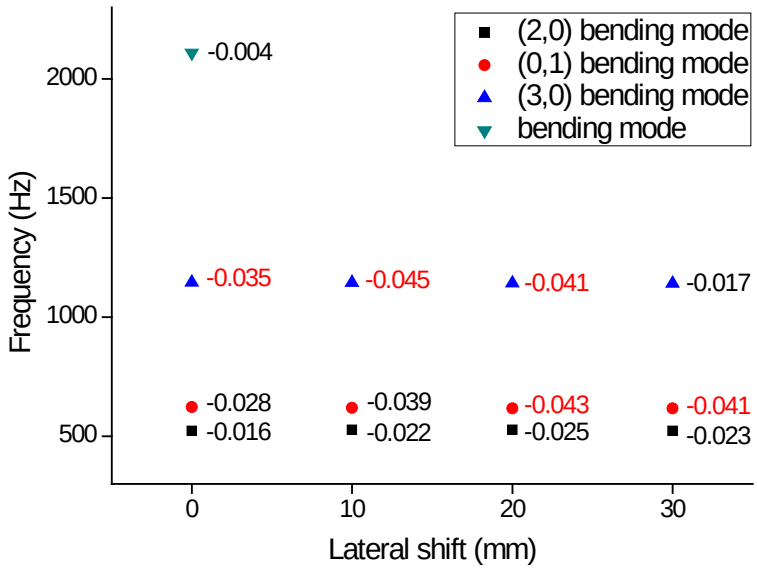

Figure 4-9 Unstable modes distribution under varied wheel lateral shift – effective damping ratio

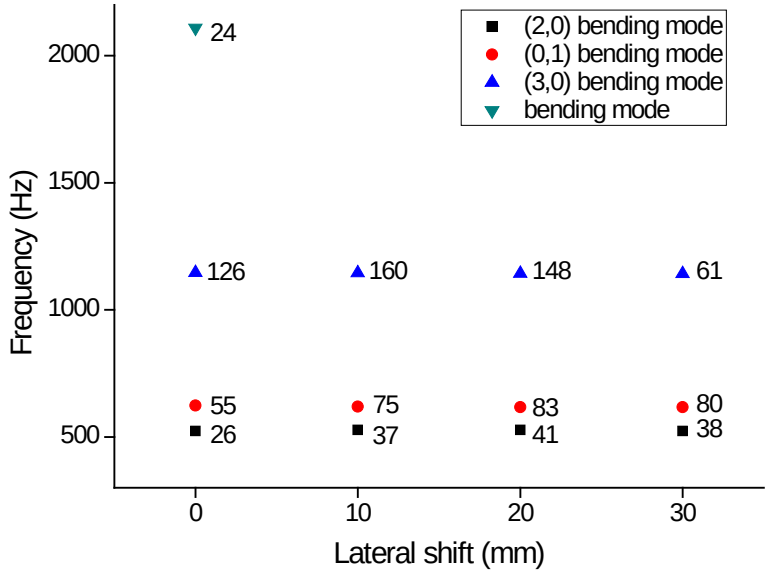

Figure 4-10 Unstable modes distribution under varied wheel lateral shift – real part

The wheel lateral shift ranges from 0 to 30 mm. The associated simulation results of the unstable modes are shown in Figure 4-9 and Figure 4-10. As we can see, when the lateral shift is 0 mm and 10 mm, the major unstable mode is the one involving (3,0) wheel bending mode; when the lateral shift increases to 20 mm, two modes, the one involving (3,0) and the one with (0,1) wheel bending mode, become equally significant with respect to vibration instability. Then, when the lateral shift continues to increase

to 30 mm, the major unstable mode shifts to the one involving (0,1) wheel bending mode only.

4.3.6 Influence of the stiffness from rail pad on squeal

For a common railway track with concrete sleeper, the rail pad characteristics, that is, its stiffness in the vertical direction, play an important role in rail vibration. To investigate the rail contribution for squeal tendency, a range of rail stiffness properties is listed below and applied in associated simulations.

The normal rail pad vertical stiffness ranges from 45.57 to 173.01 MN/m. Here, the reference case is the one with vertical stiffness of 58.8 MN/m and lateral stiffness of 29.4 MN/m. The rail pad vertical stiffness increases to about 2 times and 3 times, and the lateral stiffness is kept the same, that is, from 58.8 MN/m to 100 MN/m and 150 MN/m.

As shown on Table 4-1, the real part of these 3 unstable modes involving (2,0), (0,1), and (3,0) wheel bending mode, and the associated rail twisting mode changes by -72%~-95%, 127%~148%, 29%~45%.

Table 4-1 The influence of rail pad vertical stiffness on squeal

	Real part of the system eigenvalue		
Rail pad vertical stiffness MN/m	Wheel (2,0) and rail around 500 Hz	Wheel (0,1) and rail around 640 Hz	Wheel (3,0) and rail around 1150 Hz
58.8	41.39	83.4	147
100	11.37	189.36	190.2
150	2.14	209.12	213.53

* (*n*,*m*) wheel mode: wheel bending mode with *n* nodal diameter and *m* nodal circle.

4.3.7 Influence of the rail support damping on squeal

Here, the reference case is the one with no rail vertical and lateral support damping, then the rail pad vertical damping and lateral damping changes to 75 kNs/m and 60 kNs/m, respectively.

As shown on Table 4-2, after these rail pad and fastener damping is applied, those original rail dominant unstable modes between 500 to 5500 Hz almost disappear, the unstable modes remained are those with both wheel and rail strong vibration, but the unstable frequencies between 400~1200 Hz remain significant.

Table 4-2 The influence of rail pad damping on squeal

Without rail support damping				With rail support damping			
Mode shape	Frequency	Real part	EDR	Mode shape	Frequency	Real part	EDR
wheel (3,0) and rail	1143.5	147.5	-0.04106	wheel (2,0) and rail	487.79	126.85	-0.08278
wheel bending and rail	617.47	83.406	-0.043	wheel (0,1) and rail	430.75	91.811	-0.06785
rail dominating	1962.9	70.357	-0.01141	Wheel bending dominating	642.68	48.469	-0.02401
wheel (2,0) and rail	526.74	41.39	-0.02501	wheel (3,0) and rail	1166.9	20.557	-0.00561
rail dominating	433.8	14.915	-0.01094	Wheel bending dominating	2126.2	0.10062	-0.00002
rail dominating	4642.7	14.038	-0.00096				
rail dominating	4911.1	6.2173	-0.0004				
rail dominating	4709.6	5.8899	-0.0004				
rail dominating	89.34	3.7086	-0.01321				
rail dominating	1399.2	1.0814	-0.00025				
rail dominating	5360.3	0.35057	-0.00002				
rail dominating	288.73	2.81E-02	-0.00003				

From Table 4-3, it can be found that the most unstable frequency shifts to a lower frequency when the rail pad damping is present.

Table 4-3 The influence of rail pad damping on squeal

	Real part of the system eigenvalue (Positive value indicating instability)		
	Wheel (2,0) and rail around 500 Hz	Wheel (0,1) and rail around 640 Hz	Wheel (3,0) and rail around 1150 Hz
No rail damping	41.39	83.4	147
With rail damping	126.85	48.47	20.56

4.3.8 Combinations of wheel influencing parameters investigation

(1) Squeal events between 400 ~ 5500 Hz

In this section, a study of different combinations of values of three parameters - wheel-rail friction coefficient, wheel diameter and wheel lateral shift with respect to rail - has been explored using the model developed. These parameter variations are listed in Table 4-4.

Table 4-4 Major influencing parameters for squeal tendency investigation

Parameter	range	interval
Wheel-rail friction coefficient	0.2 – 0.6	0.2
Wheel diameter	780 mm – 840 mm	20 mm
Wheel lateral shift	0 mm – 30 mm	10 mm

The resulting effective damping ratio for the various combinations investigated is presented in Figure 4-11. In these contour plots, squeal occurrence tendency is indicated by the magnitude of the negative effective damping ratio caused by friction coupling, with the red zone representing the high squeal occurrence tendency, and the blue/grey zone representing the low squeal occurrence tendency.

From Figure 4-11, it can be found that, as the friction coefficient decreases, the magnitude of the negative effective damping ratio due to friction coupling generally decreases, as indicated by the warm color zones gradually replaced by cold colors. When the friction coefficient is small enough, such as the 0.2 cases, the unstable status

disappears in most of the combination of wheel diameter and lateral shift, as indicated by the gray area in Figure 4-11(c).

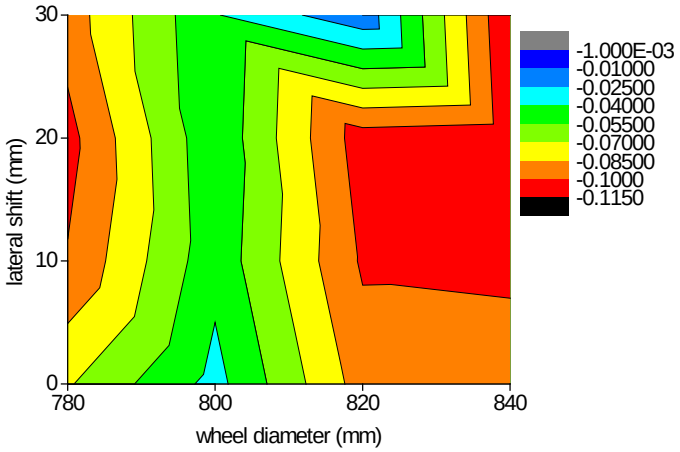

(a) Friction coefficient = 0.6

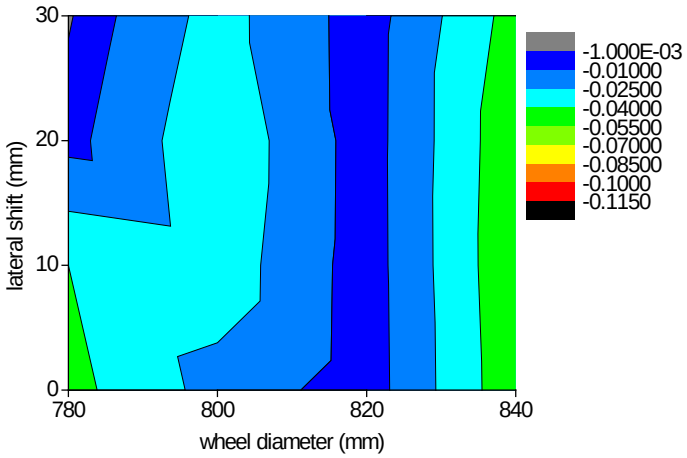

(b) Friction coefficient = 0.4

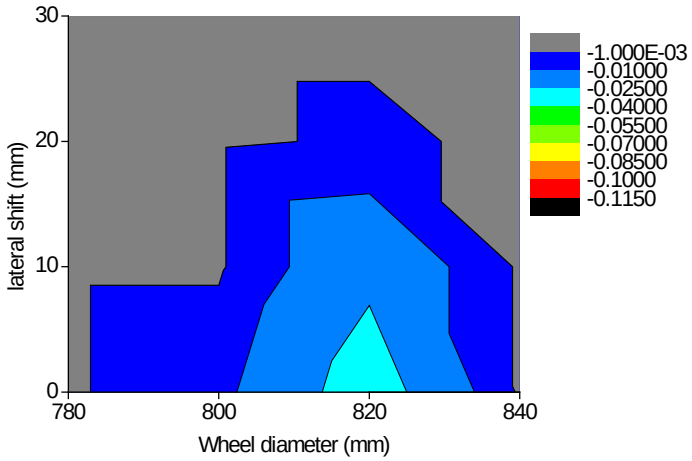

(c) Friction coefficient = 0.2

Figure 4-11 Maximum magnitude of the negative effective damping ratio under friction coupling

For the high friction cases: μ=0.6, the highest number of unstable cases occurred when the lateral shift ranged from 10 to 20mm and the wheel diameter was either between 820 and 840 mm, or was 780 mm. For the medium friction cases: μ=0.4, the highest number of unstable cases occurred for a wheel diameter of 780 mm with lateral positions of 0 to 10 mm off the nominal contact position, and for all wheel positions where the wheel diameter was 840mm wheel diameter cases. The wheel diameter of 820 mm was the most stable for all wheel lateral positions. For the low friction cases: μ=0.2, the highest number of unstable cases occurred for a wheel diameter of 820 mm with 0 mm lateral shift.

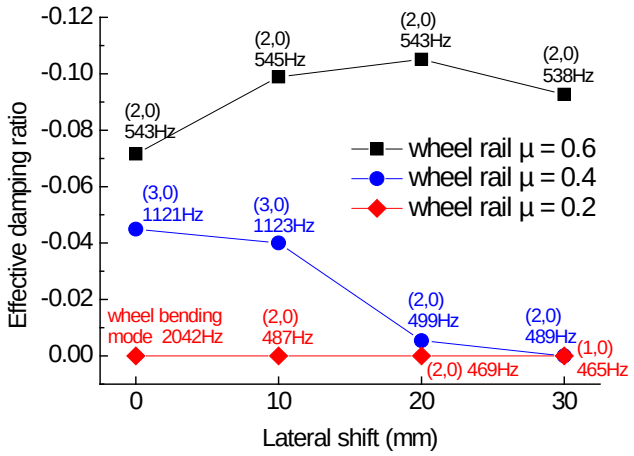

(a) Wheel diameter = 780mm

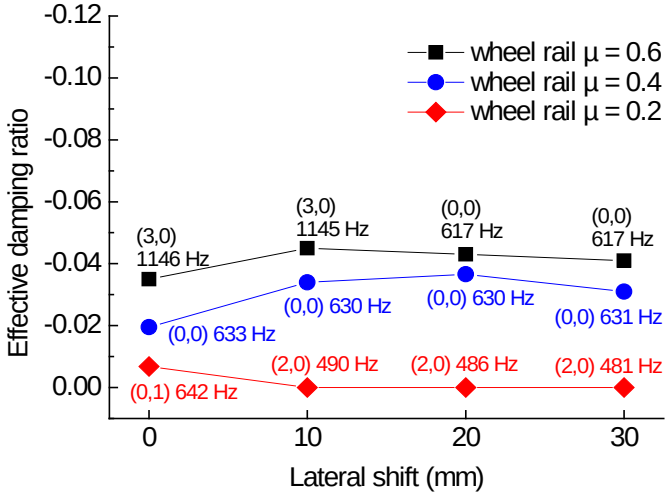

(b) Wheel diameter = 800 mm

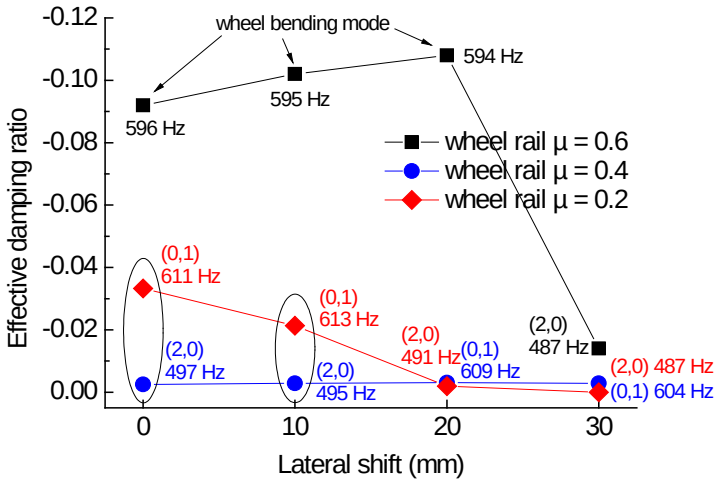

(c) Wheel diameter = 820mm

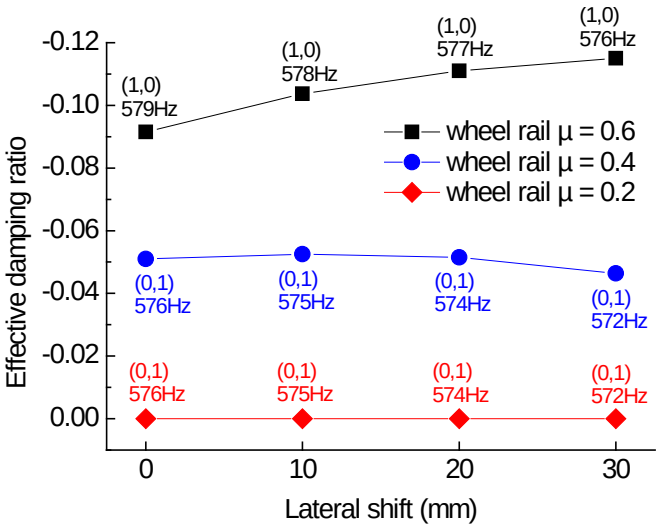

(d) Wheel diameter = 840 mm

Figure 4-12 Effective damping ratios under different conditions

There are some exceptional cases where for a lower friction level the tendency for squeal is actually higher than for the high friction case, as indicated by the larger magnitude of negative effective damping ratio caused by friction coupling. This is evident in Figure 4-12, as circled in Figure 4-12 (c). These exceptions occur for a wheel diameter of 820 mm and a friction coefficient range from 0.2 to 0.4 for a lateral shift of both 0 and 10 mm.

In each case the most unstable mode, as indicated by the dots against points in Figure 4-12, may or may not correspond to the same type of wheel-rail system mode. The risk is the spurious comparison of relative values of squeal index of different types of

system mode which often are of different magnitude. For this reason it is necessary to further compare the squeal index: the positive real part or the negative effective damping ratio for the same type of wheel-rail system individually.

Most interest in the rail noise situation is related to wheel-rail curve squeal events that are mono-tonal, high pitch noise at frequencies above 1000 Hz. In contrast, the majority of the observed unstable modes in this study were below 1000 Hz and normally between 500 – 600 Hz. This represents only one type of squeal: low frequency squeal. These unstable modes mostly involve significant vibration contribution of (2,0), (1,0) and (0,1) wheel bending modes around 500 – 600 Hz. In a small number of cases unstable (3,0) wheel bending modes were observed at around 1120 Hz.

(2) Squeal events between 1000 Hz ~ 5500 Hz

Unstable modes, their frequencies, and squeal index of 48 simulation cases when wheel-rail friction coefficient is 0.6, 0.4 and 0.2 are set out in Table 4-5 to Table 4-7, respectively. Again, only unstable modes with a significant wheel vibration component are included based on the visual inspection of the displacement contour of the individual complex eigenmode. There are quite a few unstable modes. Only the rail shows a significant vibration. The wheel vibration level was found to be minor and so is not important to the phenomenon under investigation here..

The reason for the neglecting of discussion of the types of unstable modes with only strong rail vibration and low wheel vibration is: firstly that the rail support damping from the rail pad is not included in the simulation; and, secondly, as shown in Section 4.3.7 and Section 4.3.9 (2), when the rail support damping is included then the original rail dominant unstable modes between 500 to 5500 Hz almost disappear. The unstable modes that remain are those that result in strong vibration of both the wheel and rail. However the unstable frequencies between 400~1200 Hz remain significant.

The friction coefficient was also observed to influence the relationship between squeal and the wheel-rail friction coefficient. In the 0.6 friction coefficient cases there are 22

unstable modes altogether. Conversely, in the 0.4 and 0.2 friction coefficient cases the number of unstable modes is significantly reduced to 10 and 3, respectively. The corresponding squeal index: the amplitude of the positive real part of the unstable complex eigenvalue, is also reduced as the friction level is reduced.

Table 4-5 Unstable frequencies above 1000 Hz (friction coefficient = 0.6)

		Lateral displacement			
		0 mm	10 mm	20 mm	30 mm
Wheel diameters	780 mm	Wheel (3,0) mode, 1117.9 Hz, Real Part=243.4; Wheel (4,0) mode, Freq=2046 Hz, Real Part=70.4;	Wheel (3,0) mode, 1117.6 Hz, Real Part=260.4; Wheel (4,0) mode, Freq=2040.6 Hz, Real Part=85.7;	Wheel (3,0) mode, 1116.7 Hz, Real Part=242; Wheel (2,1) mode, Freq=2035 Hz, Real Part=69.9;	Wheel (3,0) mode, 1114.6 Hz, Real Part=177.5; Wheel (2,1) mode, 2029 Hz, Real Part=18;
	800 mm	Wheel (3,0) mode, 1145.8 Hz, Real Part=125.9; Wheel (4,0) mode, 2108.5 Hz, Real part=24; Wheel (5,0) mode, 3146.7 Hz, Real part=1.7;	Wheel (3,0) mode, 1144.5 Hz, Real Part=160.6	Wheel (3,0) mode, 1143.5 Hz, Real Part=147.5	Wheel (3,0) mode, 1141.5 Hz, Real Part=61.7
	820 mm	Wheel (3,0) mode, 1186.6 Hz, Real Part=10.1	Wheel (3,0) mode, 1180.8 Hz, Real Part=12.6; Wheel web bending mode, 2056.8 Hz, Real part=2.3;	Wheel (3,0) mode, 1180.7 Hz, Real Part=2.5;	None
	840 mm	Wheel (3,0) mode, 1210.4 Hz, Real Part=2.8;	Wheel (3,0) mode, 1207 Hz, Real Part=1.6;	Wheel web bending mode, 1989 Hz, Real Part=2.3;	Wheel web bending mode, 1989 Hz, Real Part=1.2;

For the related wheel mode in these squeal situations, there are: 16 counts of the wheel (3,0) bending mode around 1120 Hz; 7 counts of the wheel (4,0) bending mode around 2040 Hz; 4 counts of the wheel (2,1) bending mode around 2030 Hz; and, 1 count of

wheel (5,0) bending mode around 3150 Hz. In addition, there are 6 counts of 2 types of wheel web bending mode with non-identifiable nodal diameter *n* or nodal circle *m*.

Table 4-6 Unstable frequencies above 1000 Hz (friction coefficient = 0.4)

		Lateral displacement			
		0 mm	10 mm	20 mm	30 mm
Wheel diameters	780 mm	Wheel (3,0) mode, 1121 Hz, Real Part=158.3; Wheel axial bending mode (4,0), 2046 Hz, Real Part=43.9;	Wheel (3,0) mode, 1123 Hz, Real Part=140.9; Wheel axial bending mode (4,0), 2042 Hz, Real Part=45;	Wheel (2,1) mode, 2033 Hz, Real Part=7.9;	Wheel (2,1) mode, 2023.5 Hz, Real Part=0.8;
	800 mm	(3,0) mode, 1164 Hz, Real Part=4.3; Wheel bending mode, 2106.5 Hz, Real Part=0.4;	None	None	None
	820 mm	None	Wheel web bending mode, 2057 Hz, Real Part=2.7;	None	None
	840 mm	None	None	Wheel web bending mode, 1989 Hz, Real Part=1.75;	None

Table 4-7 Unstable frequencies above 1000 Hz (friction coefficient = 0.2)

		Lateral displacement			
		0 mm	10 mm	20 mm	30 mm
Wheel diameters	780 mm	Wheel (4,0) mode, 2041.5 Hz, Real Part=1.9;	Wheel (4,0) mode, 2034.5 Hz, Real Part=0.2;	None	None
	800 mm	None	None	None	None
	820 mm	None	Wheel web bending mode, 2057 Hz, Real Part=2.0;	None	None
	840 mm	None	None	None	None

Table 4-8 Squeal index comparison around 1120 Hz involving wheel (3,0) bending mode

		μ	Lateral displacement			
			0 mm	10 mm	20 mm	30 mm
Wheel diameters	780 mm	0.6	Real part=243.4; EDR=-0.06931	Real part=260.4; EDR=-0.07417	Real part=242; EDR=-0.06898	Real part=177.5; EDR=-0.05069
		0.4	Real part=158.3; EDR=-0.04494	Real part=140.9; EDR=-0.03995		
		0.2				
	800 mm	0.6	Real part=125.9; EDR=-0.03497	Real part=160.6 EDR=-0.04467	Real part=147.5 EDR=-0.04106	Real part=61.7 EDR=-0.0172
		0.4	Real part=4.3; EDR=-0.00116			
		0.2				
	820 mm	0.6	Real part=10.1 EDR=-0.00271	Real part=12.6; EDR=-0.0034	Real part=2.5; EDR=-0.00068	
		0.4				
		0.2				
	840 mm	0.6	Real part=2.8; EDR=-0.00073	Real part=1.6; EDR=-0.00042		
		0.4				
		0.2				

* Positive real part or negative effective damping ratio (EDR) indicate vibration instability (squeal)

* The cells left blank mean these are the stable cases (no squeal)

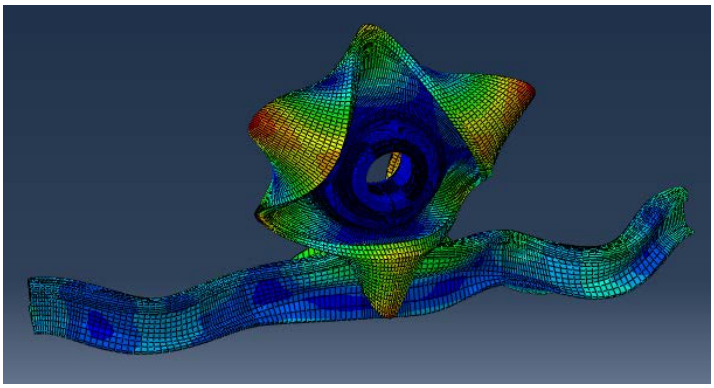

Figure 4-13 Unstable wheel (3,0) bending mode and rail around 1120 Hz

Several types of unstable modes are worth detailed analysis. In Table 4-8: for the wheel (3,0) modes shown on Figure 4-13, it is observed that when the friction level is high: μ=0.6, this mode becomes unstable at most lateral displacements for all wheel diameters. However, when the friction level is in the moderate range: μ=0.4, instability of this mode only occurs at wheel diameters of 780 and 800 mm and then only for

lateral displacements of no more than 10mm. When the friction level is low: μ=0.2, this mode becomes stable in all cases.

Table 4-9: for the wheel (4,0) modes shown on Figure 4-14, indicates that it only becomes unstable in a small number of wheel diameter and lateral displacement combination. In the case of 780 mm wheel diameter and 0-10 mm lateral displacement, it remains unstable in all three different friction levels. Whereas in the 800 mm wheel diameter and 0 mm lateral displacement, it only is unstable at the high friction level.

Table 4-9 Squeal index comparison around 2040 Hz involving wheel (4,0) bending mode

		μ	Lateral displacement			
			0 mm	10 mm	20 mm	30 mm
Wheel diameters	780 mm	0.6	Real part=70.4; EDR=-0.01096	Real part=85.7; EDR=-0.01337		
		0.4	Real part=43.9; EDR=-0.00683	Real part=45; EDR=-0.00701		
		0.2	Real part=1.9; EDR=-0.0003	Real part=0.2; EDR=-0.00003		
	800 mm	0.6	Real part=24; EDR=-0.00362			
		0.4				
		0.2				
	820 mm	0.6				
		0.4				
		0.2				
	840 mm	0.6				
		0.4				
		0.2				

* Positive real part or negative effective damping ratio (EDR) indicate vibration instability (squeal)

* The cells left blank mean these are the stable cases (no squeal)

A closer analysis of Table 4-9 and Table 4-10 reveals that the 780 mm wheel diameter cases involve only the unstable wheel (4,0) bending mode when the lateral displacement is between 0 mm to 10 mm, whereas it involves only the unstable wheel (2,1) bending mode, shown on Figure 4-15, when the lateral displacement is between 20 mm to 30 mm. These two unstable modes are important between 2000 and 3000 Hz.

Table 4-10 Squeal index comparison around 2030 Hz involving wheel (2,1) bending mode

		μ	Lateral displacement			
			0 mm	10 mm	20 mm	30 mm
Wheel diameters	780 mm	0.6			Real part=69.9; EDR=-0.01094	Real part=18; EDR=-0.00284
		0.4			Real part=7.9; EDR=-0.00124	Real part=0.8; EDR=-0.00013
		0.2				
	800 mm	0.6				
		0.4				
		0.2				
	820 mm	0.6				
		0.4				
		0.2				
	840 mm	0.6				
		0.4				
		0.2				

* Positive real part or negative effective damping ratio (EDR) indicate vibration instability (squeal)

* The cells left blank mean these are the stable cases (no squeal)

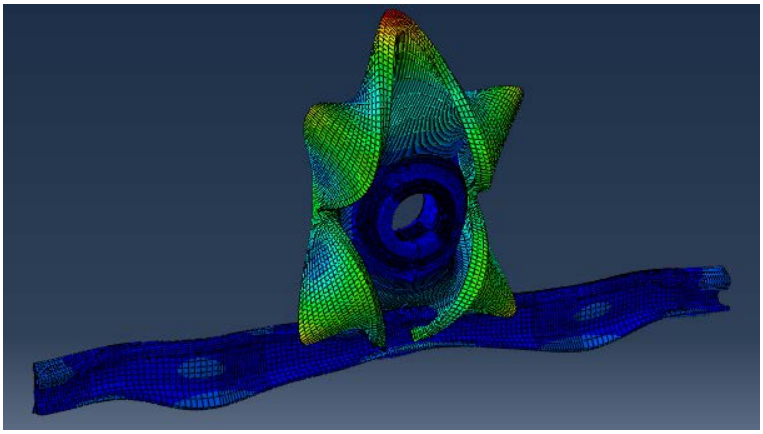

Figure 4-14 Unstable wheel (4,0) bending mode and rail around 2040 Hz

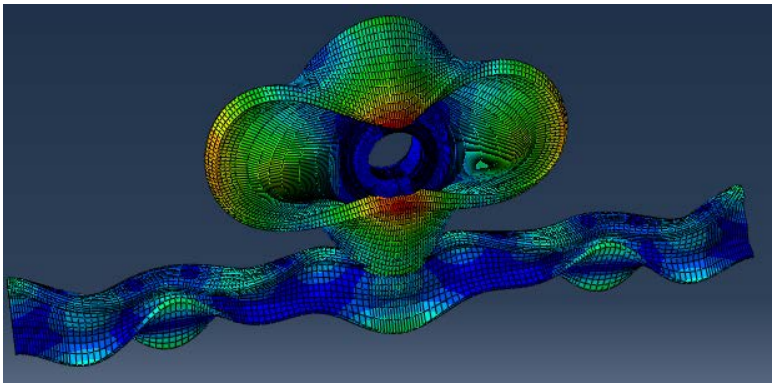

Figure 4-15 Unstable wheel (2,1) bending mode and rail around 2030 Hz

For the wheel (5,0) bending mode around 3150 Hz, it is only unstable in the case of 800 mm wheel diameter and 0 mm lateral displacement.

Table 4-11 Squeal around 3150 Hz involving wheel (5,0) bending mode

		μ	Lateral displacement			
			0 mm	10 mm	20 mm	30 mm
Wheel diameters	780 mm	0.6				
		0.4				
		0.2				
	800 mm	0.6	Real part=1.7; EDR=-0.00017			
		0.4				
		0.2				
	820 mm	0.6				
		0.4				
		0.2				
	840 mm	0.6				
		0.4				
		0.2				

* Positive real part or negative effective damping ratio (EDR) indicate vibration instability (squeal)

* The cells left blank mean these are the stable cases (no squeal)

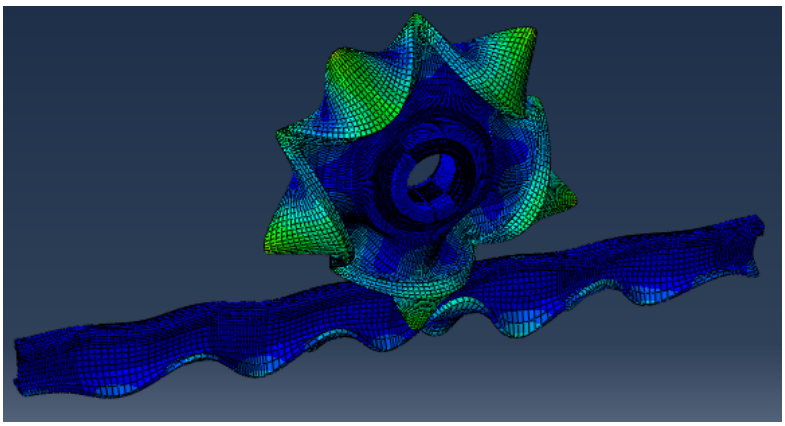

Figure 4-16 Unstable wheel (5,0) bending mode and rail around 3150 Hz

4.3.9 Combinations of lateral and longitudinal creepage investigation

In these simulation cases the longitudinal and lateral creepage values have been combined in order to maintain a unit sliding velocity in five different directions: longitudinal (0 degree); lateral (90 degrees); 22.5 degrees; 45 degrees; and, 67.5 degrees. In each direction six different wheel-rail friction coefficients are applied: from

0.1 to 0.6. Altogether 30 cases are simulated and the maximum real part of the complex eigenvalue is represented besides each dot on Figure 4-17 and Figure 4-18.

(1) Simulation cases without rail support damping present

In Figure 4-17, in each sliding direction, different sets of wheel and rail modes are excited:

In the longitudinal direction (0 degree), only two unstable modes exist, (1) wheel vibration from wheel radial mode combined with rail head and foot twisting vibration along the longitudinal axis is excited at 4901 Hz; (2) wheel vibration from wheel bending mode combined with rail vertical vibration along the longitudinal axis is excited at 4901 Hz. The real parts range from 0.38~2.68. Although instability can be indicated, they are relatively small.

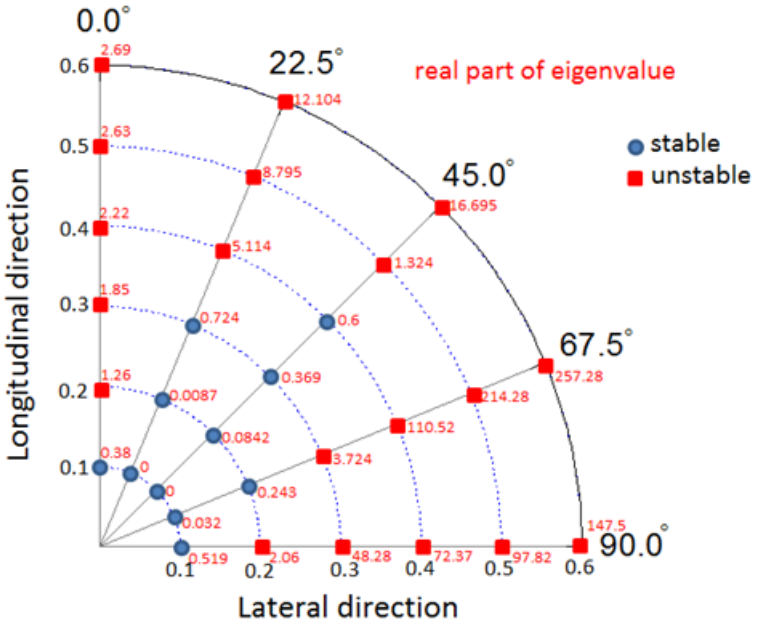

Figure 4-17 Instability under different creepage combination without rail damping

Stable： real part of system eigenvalue >1.0, positive

Unstable: real part of system eigenvalue <1.0 or negative

At 22.5 degrees, instability starts when the friction coefficient reaches 0.4, while at 45 degrees instability starts when the friction coefficient reaches 0.5.

A significant feature which cannot be missed is at the lateral direction (90 degrees) and the direction nearest it (67.5 degrees). The instability index – the real part – has a much

larger value (10 to 100 times) when compared with these values in other directions. It should be noted that the lateral creepage or lateral sliding velocity plays a major role in causing instability and thus squeal. Alternatively, we could say that, the longitudinal creepage or the longitudinal sliding velocity tends to make the system more stable when it is added to the lateral sliding cases.

(2) Simulation cases with rail support damping represent

As shown in Figure 4-18, firstly, rail support damping can largely eliminate all of the unstable eigenmodes. These have been observed to result in very strong rail vibration only with relatively minor wheel vibration. In addition, earlier simulations of deformable wheel with rigid rail model, briefed in Appendix IV, show no unstable frequencies. Thus, based on these observations, it is concluded that rail vibration/deformation plays an irreplaceable and necessary part in the instability of wheel-rail lateral sliding contact in 1000 Hz and above in the case of constant friction coefficient. Such instability is not caused the frequency convergence (or mode coupling) of the two wheel modes in the nearby frequency range. It is due to coupling of vibration of wheel and rail in the vertical and lateral directions. Furthermore, when rail support damping is applied, the former unstable cases in longitudinal direction become stable.

Compared with rails with concrete sleep support, rails with timber sleeper support may provide large damping in the higher frequency range, as shown in the experimental data of track decay rate. From our frequency domain squeal simulations, it has been shown that rail damping exhibits a great influence on reducing the positive value of the real part of the complex eigenvalue and thus eliminates most of the squeal frequencies in the case of 800 mm wheel diameter and 20 mm wheel lateral shift under different combinations of longitudinal and lateral sliding. Also, rail damping can greatly reduce the value of the instability indicator and eliminate most unstable eigenmodes which feature very strong rail vibration with minor wheel vibration.

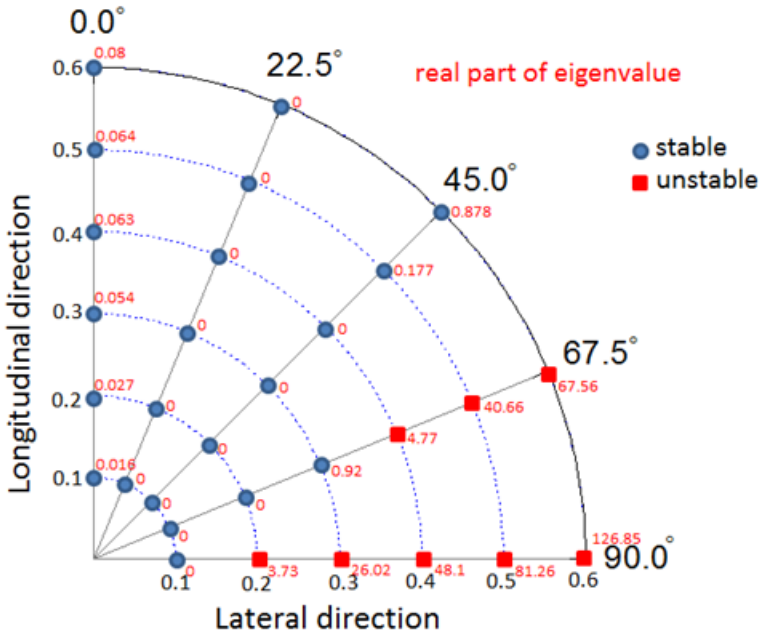

Figure 4-18 Instability under different creepage combination with rail damping

4.4 Summary

The following have been observed:

1. All of the unstable frequencies are related to certain out-of-plane bending modes of wheel and rail lateral twisting. There is strong vibration coupling between wheel and rail in the normal and tangential directions due to friction. The unstable wheel mode with the maximum value of squeal index was found to be the wheel (3,0) bending mode around 1120 Hz in the 1000-2000 Hz range.
2. The wheel-rail friction coefficient has a major impact on the occurrence of curve squeal; wheel-rail interface lubrication, indicated by a friction coefficient ≤0.2, can largely prevent the occurrence of vibration instability and hence squeal; the possibility of the occurrence of curve squeal increases as the friction coefficient increases.
3. For the wheel investigated, the reduction of wheel rim thickness and hence wheel diameter tends to increase the number of potentially unstable modes. Especially when the wheel diameter reaches the replacement level, 780mm in

the cases studied, there is a high squeal tendency at frequencies of 1000-2100 Hz. This was observed for all lateral displacements simulated.

4. Wheel-rail relative lateral shift tends to alter the most unstable frequencies from one involving a certain wheel mode to another.
5. Rail support damping plays an important role in reducing the tendency of squeal in quite a few frequencies, especially those involving significant or dominating rail vibrations with relatively smaller wheel vibration. However, rail support damping test data of rail pads is only available at low frequencies, below 100 Hz, so when it is extended to be used in our squeal simulation at much higher frequencies, these damping values might be too large. Thus this prediction tends to overestimate the influence of rail support damping on squeal control.
6. The lateral creepage or lateral sliding velocity plays a major role in causing instability and thus squeal. Alternatively, we could say that the longitudinal creepage or longitudinal sliding velocity tends to make the system more stable when it is added to the lateral sliding cases.

5. Conclusion and future work

5.1 Conclusion

A frequency-domain model for wheel-rail curve squeal prediction has been developed representing: nonlinear wheel-rail contact; with a constant friction coefficient; constant sliding state; and, subsequent complex eigenvalue extraction.

Although a similar model was originally proposed by Chen et al. (2010) for wheelset-track system rail corrugation analysis, this work has been extended to thoroughly investigate a comprehensive set of parameters, and their combination, that influence curve squeal in a freight operation scenario common to the Australian rail industry in particular. These parameters include: wheel-rail friction coefficient; wheel rim thickness; lateral shift between wheel and rail; rail pad properties; and lateral and longitudinal creepage. A clear advantage of the model developed is its computation efficiency, which allows a large number of parameters to be simulated in the frequency domain.

A better understanding of the complexity of different parameters influencing the curve squeal is obtained. These new understandings are:

1. All of the unstable frequencies are related to particular out-of-plane bending modes of the wheel and rail lateral twisting. Strong vibration coupling between wheel and rail in the normal and tangential directions due to friction has been observed. The unstable wheel mode with the maximum value of squeal index was found to be the wheel (3,0) bending mode around 1120 Hz in the 1000-2000 Hz range.
2. The wheel-rail friction coefficient has a major impact on the occurrence of curve squeal. Wheel-rail interface lubrication, indicated by a friction coefficient of less than 0.2, can largely prevent the occurrence of vibration instability and hence squeal. The possibility of the occurrence of curve squeal increased as the friction coefficient increased.
3. For the wheel investigated, reduction of the wheel rim thickness and hence the

wheel diameter increases the number of potentially unstable modes. Especially when the wheel diameter reaches the replacement level, 780mm in the cases studied, there is a high squeal tendency at frequencies of 1000-2100 Hz. This was observed for all lateral displacements simulated.

4. The wheel-rail relative lateral shift alters the most unstable frequencies from one involving a certain wheel mode to another.
5. Rail support damping has a significant effect on the tendency of squeal at numerous frequencies, especially those involving a combination of significant or dominating rail vibrations with relatively smaller wheel vibration.
6. Lateral creepage or lateral sliding velocity plays a major role in causing instability and thus squeal. This also implies that longitudinal creepage or longitudinal sliding velocity makes the system more stable when it is added to the lateral sliding case.

The frequency-domain squeal prediction model of deformable wheel and rigid rail has not shown any unstable frequency, whereas the models of deformable wheel and deformable rail in this thesis do show a lot of unstable frequencies. The rail vibration participation in these unstable wheel rail system modes plays an important role in wheel rail squeal as an energy feeding resource which was largely neglected by other experts. The deformable wheel structure alone is not enough to lead to vibration instability (squeal) under the initial condition of stable sliding and constant friction coefficient. The structure coupling of the wheel between the lateral and vertical direction is not enough to induce instability of the wheel in the lateral direction under the influence of the constant friction coefficient condition.

The rail supporting damping can greatly reduce the number of the unstable modes, it can stabilize these unstable system modes with only rail strong vibration and very weak wheel vibration participation in the non-rail-support-damping cases, but it does not greatly affect these unstable system modes with both strong wheel bending vibration and rail twisting vibration. The rail vertical deformation changes as the rail twists in its cross section. This sustained vertical deformation of the rail in the

coinciding frequency of a certain wheel bending mode will create a type of harmonic displacement in the vertical direction in this particular frequency. Since it is generally known that in the simple one degree of freedom ‘mass on a belt’ model that both the negative slope friction coefficient and the sustained normal force variance can induce the limit cycle: the instability of the mass in the lateral direction. It is proposed that it is the sustained vibration of the rail in its twisting mode that provides the normal force variance needed for the occurrence of instability of the wheel axial bending mode in the lateral direction. In addition, in the rail twisting mode, the deformation of the rail in the vertical and lateral direction is coupled and cannot be separated. Thus the coupling of degrees-of-freedom mechanism for the wheel rail curve squeal phenomenon would be the friction coupling between one or two degrees of freedom for the wheel vibration and two degrees of freedom for the rail vibration in the vertical and lateral directions.

The sensitivity of wheel angle-of-attack has been explored through the development of a detailed freight wagon model that included key bogie parameters. A ranking in terms of influence of these parameters has been established. The nature of the influence of a combination of centre bowl friction and warp stiffness on AOA has now been clarified. Largest simulated AOA values approximate field test measurements.
The influence and ranking of importance of bogie parameters and their combination in different worn conditions on wheelset AOA will assist vehicle operators in determining AOA management strategies relevant to bogies. This work partially fulfils this goal.

The functioning of these two models: for the rapid prediction of railway curve squeal, and for the investigation of large AOA has been proved. They serve as efficient and effective models for a thorough investigation of a vast number of parameters involved wheel-rail curve squeal phenomena. All simulated results help to demystify the relationship of years of field monitoring data of wheel AOA, squeal, rail force, bogie worn condition, and wheel-rail geometry collected from a specific monitoring site.

5.2 Future work

Investigation of wheel profile impact on AOA:

The vehicle curving dynamics simulations developed are based on unworn wheel profiles. Worn profiles, particularly hollowed wheels, could induce a very large AOA of 24 mrad from field monitoring. More data of worn wheel profiles needs to be pursued in any future assessment of its effect on AOA.

Trailing axle role in squeal generation:

Trailing axle AOA is apparently a significant source of wheel squeal. The work undertaken here was limited to a study of the leading axle. Similar investigations focusing on the observations from field measurements of large AOA on trailing axles and particularly from trailing bogies will be worthwhile.

Train dynamic effects:

There is a relationship between tractive effort, longitudinal dynamics and the curving behaviour of freight bogies (Grassie, Elkins, 2005; El-Sibaie, 1993), which has not been included in the wagon simulation work done. Coupler-load alone could induce leading axle AOA of 30 mrad including high rail-flange contact, and the trail axle AOA reaching around 30 mrad in low rail-flange contact when negotiating a 175 m radius curve (El-Sibaie, 1993).

Field verification of modelling results:

In order to verify the conclusion of the main causes of large wheelset AOA drawn through simulation, and to provide solid associated bogie maintenance advice in regard to wheelset AOA control, depot bogie data testing needs to be conducted in order to verify the results obtained. Firstly, a series of tests needs to be conducted to measure these key bogie parameter' values under the worn conditions shown in that bogie, especially the friction moment between bolster and carbody, the warp stiffness of the bogie, and the worn wheel profiles. Secondly, individual wheelset AOA, the bogie steering moment from wheelsets, and bogie warp angle need to be measured from field

test with sensors from wayside and on the bogie. These results would then be compared with the corresponding simulation results after the simulated bogie parameters are adjusted according to tests conducted in the workshop. This would serve as the first step in verifying the major conclusion obtained by the model and decide the accuracy threshold of the model.

Further steps would include renovating bogie components which affect only one of the three major moments that control wheelset AOA performance, that is, re-profiling wheels to restore normal wheelset steering moment, replacing worn friction wedges with new wedges to restore normal warp stiffness, repair worn centre plates and checking the CCSB setup height to restore normal friction moment between bolster and carbody. Wheelset AOA performance will then be re-checked.

Energy feeding mechanism:

It will be valuable to further clarify the energy feeding mechanism of the wheel rail vibration instability in higher frequencies (several hundred to several thousand Hz) when squeal will dissipate energy.

Due to the formidable computation time requirement for a time-domain FEM model searching for a possible limit cycle phenomenon, it will not serve as an effective or efficient method for further research of the underlying squeal mechanism. Rather, it will be good to use a smaller scale FEM model of wheel and rail for validation of and/or comparison with results from the simple several degrees-of-freedom model.

Future work could usefully explore three or four degrees of freedom models to seek an explanation of wheel rail curve squeal mechanism: one or two degrees of freedom for the wheel vibration and two degrees of freedom for the rail vibration.

References

Anderson D., Wheatley N., etc. (2008a), Mitigation of curve squeal noise in Queensland, New South Wales and South Australia, Conference on Railway Engineering, Perth, 2008.

Anderson D., Wheatley N. (2008b), Mitigation of wheel squeal and flanging noise on the Australian rail network. Noise and Vibration Mitigation, NNFM 99, pp. 399-405, 2008.

Berglund H. (1972), Stockholm tackles the noise problem. Railway Gazette International (1972), 254-259.

Bochumer Verein (2011), http://www.bochumer-verein.de/index.php?id=488., accessed on Sep. 12th 2011.

Boocock D. (1969), Steady-state motion of railway vehicles on curved track, J. Mech. Eng. Sci., 11, 556-566, 1969.

Brunel J. F., Dufrénoy P., Demilly F. (2004), Modelling of squeal noise attenuation of ring damped wheels, Applied Acoustics, 65 (2004) 457–471.

Brunel, J. F., Dufrénoy P., Nait M., Munoz J. L., Demilly F. (2006), Transient models for curve squeal noise, Journal of Sound and Vibration, 293, 758-765.

Brunel J. F., Dufrénoy P., Charley J. (2010), Analysis of the attenuation of railway squeal noise by preloaded rings inserted in wheels. J. Acoust. Soc. Am. 127(3), 2010.

Cataldi-Spinola E., Glocker Ch., Stefanelli R., Götsch M. (2003), Influence of the wheel diameter on the curve squealing of railway vehicles, Proceedings of the 5th European Conference on Noise Control, Naples 2003.

Cataldi-Spinola E. (2007), Curve squealing mechanism of railway vehicles, Diss. ETH No. 17453, ETH Zurich, 2007.

Chen G.X., Zhou Z.R., Ouyang H., et al (2010), A finite element study on rail corrugation based on saturated creep force-induced self-excited vibration of a wheelset-track system, Journal of Sound and Vibration, 329(2010) 4643-4655.s

Chen G.X., Xiao J.B., Liu Q.Y., Zhou Z.R. (2008), Complex eigenvalue analysis of railway curve squeal, Noise and Vibration Mitigation, NNFM 99, 2008, 433-439.

de Beer F. G., Janssens M.H.A., Kooijman P.P. (2003), Squeal noise of rail-bound vehicles influenced by lateral contact position, Journal of Sound and Vibration, 267(2003), 497-507.

D'Souza A.F., Dweib A.H. (1990), Self-excited vibrations induced by dry friction, part 2: stability and limit-cycle analysis, Journal of Sound and Vibration (1990) 137(2), 177-190.

Dwight R., Jiang J. (2009), Report on current knowledge on curving noise. CRC for rail innovation, Project R1-105 Report A1, 2009, p20-31.

Earles S.W.E, Lee C.K. (1976), Instabilities arising from the frictional interaction of a pin-disc system resulting in noise generation, ASME Journal of Engineering for Industry, 98, 1, 81-88.

Elkins J.A., Gostling R.J. (1977), A general quasi-static curving theory for railway vehicles, In The Dynamics of Vehicles on Roads and Tracks, Proceedings of Fifth IAVSD Symposium, Vienna, Austria, September 1977, Slibar, A. and Springer, H., Eds., Swets & Zeitlinger Publishers, Lisse, pp. 388-406, 1978.

Elkins J.A. (1992), Prediction of wheel/rail interaction: The state-of-the-art. Vehicle System Dynamics, 20(Issue S1):1-27, 1992.

Emereole O., Simson S., Brymer B. (2006), A parametric study of bogie rotation friction management utilising vehicle dynamic simulation, 7th International Conference on Contact Mechanics and Wear of Rail/Wheel Systems (*CM2006*), Brisbane, Australia, Sep 24-26, 2006, 535-541.

Fingberg U. (1990), A model for wheel-rail squealing noise, Journal of Sound and Vibration 143(1990), 365–377.

Fritz G., Sinou J.J, Duffal J.M., Jézéquel L. (2007), Investigation of the relationship between damping and mode-coupling patterns in case of brake squeal, Journal of Sound and Vibration, 307 (2007), 591-609.

Glocker Ch. Cataldi-Spinola E., Leine R.I. (2009), Curve squealing of trains: Measurement, modelling and simulation, Journal of Sound and Vibration 324 (2009) 365-386.

Guan D., Huang J. (2003), The method of feed-in energy on disc brake squeal, Journal of Sound and Vibration, 261:297-307, 2003.

Hawthorne V.T., Sellberg R.P., Wronkiewicz R.D. (1990), Effect of maintenance practices upon performance of freight car railroad trucks, Railroad Conference, Technical Papers Presented at the 1990 ASME/IEEE Joint, 1-12.

Hoffman N., Fisher M., Allgaier R., Gaul L. (2002), A minimal model for studying properties of the mode-coupling type instability in friction reduced oscillations. Mechanics Research Communications, 29:197-205, 2002.

Jarvis R.P., Mills B. (1963-1964), Vibration induced by dry friction, Proc. IMechE, 178, 32, 847-866.

Kalker J.J. (1979), Survey of wheel-rail rolling contact theory. Vehicle System Dynamics, 5, 317-358, 1979.

Kluijver de H. (1997), Booggeluid literatuuronderzoek naar de relatie met verkanting, boogstralen en snelheid. Holland Railconsult, 1997.

Kraft K. (1967), Der Einfluβ der Fahrgeschwindigkeit auf den Haftwert zwischen Rad und Schiene. AET 22 addendum to ETR, 58-78, 1967.

Kurzweil L.G., Wittig L.E. (1981), Wheel/rail noise control – A critical evaluation. Interim Report, Bolt, Beranek & Newman, Inc., for UMTA/U.S. DOT, 1981.

López I. (1999), Theoretical and experimental analysis of ring-damped wheels, Ph.D. thesis, University of Navarra, Navarra, Spain, 1999.

López I., Busturia J.M., Nijmeijer H. (2004), Energy dissipation of a friction damper, Journal of Sound and Vibration 278(2004), 539–561.

Mace S., DiBrito D., etc. (1994), Effect of wheel and rail profiles on gage widening behavior. Proceeding of ASME/IEEE Joint Railroad Conference, 1994, 51-56.

Mace S., Pena R., etc. (1996), Effects of wheel-rail contact geometry on wheel set steering forces. Wear 191(1996), 204-209.

Mackenzie J. (1883), Resistance on railway curves as an element of danger, Proc. Instn. Civ. Engrs., 74, 1-57, 1883.

Millner N. (1978), An analysis of disc brake squeal, SAE Paper 780332.

Müller B., Jansen E., de Beer F.G. (2003), Curve squeal WP3 tool box of existing measures. Union Internationale des Chemins de Fer, report prepared by SBB and TNO, 2003.

Müller B., Oertli J. (2006), Combating curve squeal: Monitoring existing applications. Journal of Sound and Vibration 293(2006).

Monk-Steel A.D., Thompson D.J., De Beer F.G., Janssens M.H.A (2006), An investigation into the influence of longitudinal creepage on railway squeal due to lateral creepage. Journal of Sound and Vibration 293 (2006), 766-776.

Nack W.V. (2000), Brake squeal analysis by the finite element method, Int. J. Vehicle Des., 23, 3-4, 263-275.

Nashif A.D., Jones D.I.G., Henderson J.P. (1985), Vibration damping, Wiley, New York, 1985.

Nelson J.T. (1997), Wheel/rail noise control manual, TCRP Report 23, 1997.

Newland D.E. (1968), Steering characteristics of bogies, Railway Gazette, 124, 745-750, 1968.

North M.R. (1976), Disk brake squeal, Institute of Mechanical Engineering, C38/76, 169-176.

Ouyang H., Nack W., Yuan Y., Chen F. (2005), Numerical analysis of automotive disc brake squeal: a review, In. J. Vehicle Noise and Vibration, 1, 3/4, 2005, 207-231.

Park C., Han, Min G., Cho S.S. (2001), A study on the reduction of disc brake squeal using complex eigenvalue analysis, SAE 2000-01-3141.

Périard F. (1998), Wheel-rail noise generation: curve squealing by Trams, PhD Thesis, Delft University of Technology, 1998.

Pieringer A. (2011), Time-domain modelling of high-frequency wheel/rail interaction, PhD Thesis, Chalmers University of Technology, 2011.

Redtenbacher F.J. (1855), Die Gesetze des Locomotiv-Baues, Verlag von Friedrich Bassermann, Mannheim, P. 22,1885.

Remington P.J. (1985), Wheel/rail squeal and impact noise: what do we know? What don't we know? Where do we go from here? Journal of Sound and Vibration 116(1985) 339–353.

Rudd M.J. (1976), Wheel/rail noise—part 2: wheel squeal, Journal of Sound and Vibration 46(1976), 381–394.

Sawley K., Wu H. (2005), The formation of hollow-worn wheels and their effect on wheel/rail interaction. Wear 258(2005), 1179-1186.

Schrey & Veit GmbH (2011), http://sundv.gidt.info/ref.aspx, accessed on Sep. 12th 2011.

Simson S. (2006a), Project 82: Bogie rotation friction management, Bogie design factors, CRC Rail Research Industry Report, 2006.

Simson S. (2006b), Project 82: Bogie rotation friction management, Curve type and transition effects of 3 piece bogies, CRC Rail Research Industry Report, 2006.

Simson S., Pearce M. (2006c), Centre bearing rotation forces during curve transitions. Conference on Railway Engineering. Melbourne 30th April – 3rd May, 2006.

Simson S., Brymer B. (2006d), Gauge face contact implications of bogie rotation friction in curving. 7th International Conference on Contacts and Wear of Rail/Wheel Systems (*CM2006*), Brisbane, Australia, September 24-26, 2006.

Simson S., Pearce M. (2006e), Wheel wear losses from bogie rotation resistance, effects of cant and speed. ASME/IEEE Joint Rail Conference, 2006, American Society of Mechanical Engineers, Rail Transportation Division RTD, v31, 109-114.

Skerman D. (2009), Comments from Don Skerman in QRN.

Shust W., Urban C., Lovette M. (2000), Poorly-performing trucks - How to find a bad factor, Railway age, January 2000, 69-70.

Stappenbeck H. (1954), Das Kurvengeräusch der Straβenbahn – Möglichkeiten zu seiner Unterdrückung. VDI Zeitschrift, 96(6):171-175, 1954.

Tarter J.F. (2004), Prediction of unstable friction-induced vibrations using an energy criterion, PhD Thesis, Carnegie Mellon University, 2004.

Tallion A. (2001), The optimized three piece bogie – A design method for maximum performance of coulomb-damped vehicles without braces or linkages, 7th International Heavy Haul Conference, 2001, 139-149.

Tickell C.E., Downing P., Jacobsen C.J. (2004), Rail wheel squeal – some causes and a case study of freight-car wheel squeal reduction, Proceedings of ACOUSTICS 2004, 3-5 November 2004, Gold Coast, Australia.

Thompson D.J. (2009), Railway Noise and Vibration: Mechanisms, modelling and Means of Control. Oxford, UK, Elsevier Science, 2009.

Wetta, P., and Demilly, F. (1985), Reduction of wheel squeal generated on curves or during braking," Fifth International Wheelset Congress Proceedings, Paris, France, 17–22.

Wickens A.H. (2003), Chapter 6 The bogie vehicle, Fundamentals of rail vehicle dynamics: guidance and stability, Swets & Zeitlinger Publishers, 2003, p173.

Wolf G. P. (2004), Truck Warp: Causes and Cures. The Journal of Wheel/Rail Interaction, Sep 22 2004.

Wolf G. (2005), The truck bolster bowl: Is it a bowl or a bearing? The Journal of Wheel/Rail Interaction, Oct 2005.

Appendix I Wheel normal mode classification

The wheel simulated is a typical NSW freight wheel with a diameter of 800 mm and a flat tread. Eigen frequencies up to 5.5 kHz are calculated using the finite element model. All wheel nodes on the surface of the fitting hole of the wheel hub are constrained in the X direction and Y direction, not in the Z direction. Three rotational degrees-of-freedom of these nodes are all constrained. X, Y, Z direction is the longitudinal, lateral and vertical direction respectively when the wheel is running on the rail. The observation is as follows:

1. For this type of freight wheel, it can be observed that vibration in the radial and axial direction is generally coupled. It is hard to identify a pure radial mode without axial bending vibration components.

2. For the squeal occurrence peak around 2200 Hz, the corresponding mode is (4,0) axial bending mode (mode 14 and 15) at 2118.4 Hz. The frequencies of nearby modes 13 and 16 are 2103 Hz and 2126.6 Hz. For this case, it is possible that squeal is due to mode coupling of these three nearby wheel modes.

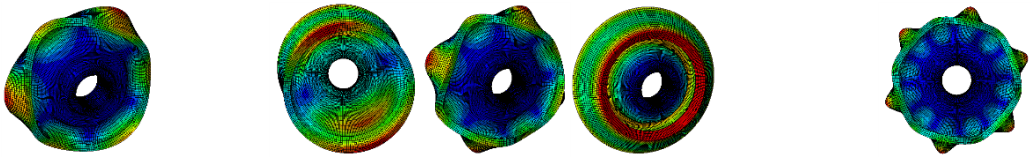

1182.3 Hz 2103 Hz 2118.4 Hz 2126.6 Hz 4233.9 Hz

(a) mode near 1200 Hz (b) modes near 2200 Hz (c) mode near 4300 Hz

Figure I-1 wheel modes around three most frequent squeal frequency ranges

3. For the squeal occurrence peak around 1200 Hz, the corresponding mode is (3,0) bending mode (mode 8 and 9) at 1182.3 Hz. The frequencies of nearby modes 7 and 10 are 843.9 Hz and 1490.2 Hz. It is not quite possible to get these nearby modes to merge into the (3,0) bending mode, since friction cannot shift the frequency of modes by 100 Hz, as seen in Hoffman's research (Hoffmann et al., 2002).

4. For the squeal occurrence peak around 4300 Hz, the corresponding mode is (6,0) bending mode (mode 34 and 35) at 4233.9 Hz. The frequencies of nearby modes 33

and 36 are 3934.7 Hz and 4572.7 Hz. It is not quite possible to get these nearby modes to merge into the (6,0) bending mode, since friction cannot shift the frequency of modes by 100 Hz as seen in Hoffman's research (Hoffmann et al., 2002).

5. For the latter two frequency ranges (1200 Hz and 4300 Hz), if a mode coupling mechanism applies, then it is only possible that the wheel and rail mode coupling in the vertical and lateral directions.

(*n*,*m*) – bending mode with n nodal diameters, m nodal circles;

(*n*,r) – radial mode with n nodal diameters;

(*n*,c) – circumferential mode with n nodal diameters.

Table 1 Classification of normal modes of a freight wheel

Mode Number	Frequency (Hz)	Mode Shape	
1	0	Rigid mode	
2	411.42	(1,0)	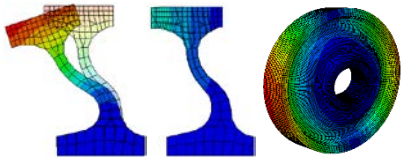
3	426.57		
4	494.27	(2,0)	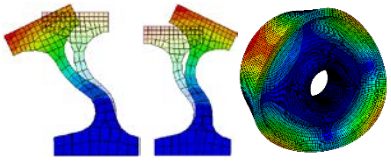
5	494.27		
6	649.14	(0,0)	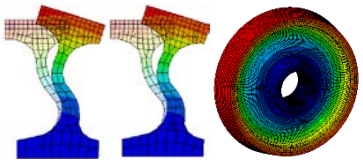
7	843.93	(0,c)	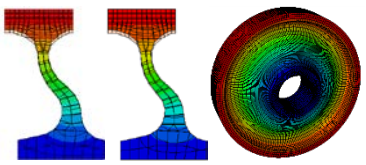
8	1182.3	(3,0)	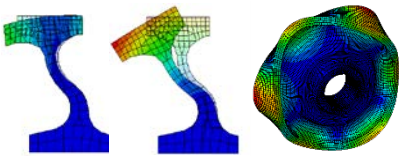
9	1182.3		

Mode Number	Frequency (Hz)	Mode Shape	
10	1490.2	Radial mode	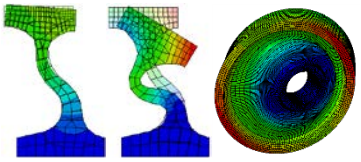
11	1922.5	(2,r)	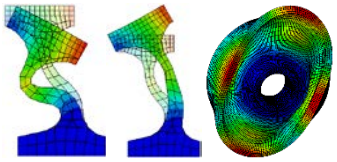
12	1922.5		
13	2103	Bending mode	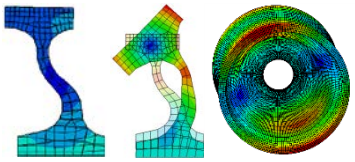
14	2118.4	(4,0)	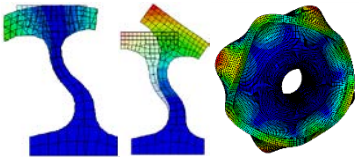
15	2118.4		
16	2126.6	Bending mode	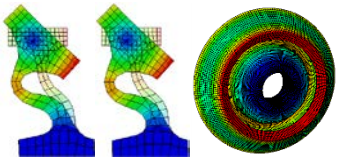
17	2409.5	Bending mode	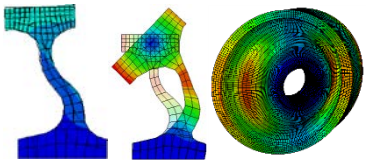
18	2417.8	(3,r)	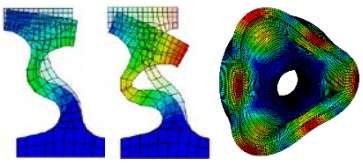
19	2417.8		
20	2854.7	Bending mode	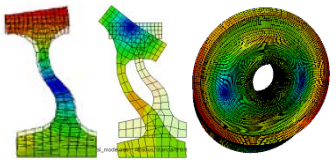
21	3037.6	(2,0)	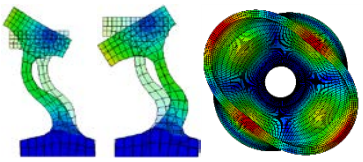
22	3037.6		

Mode Number	Frequency (Hz)	Mode Shape	
23	3098.8	(4,r)	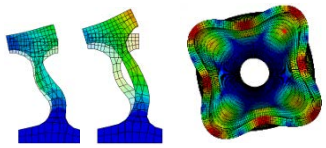
24	3098.8		
25	3159.1	(5,0)	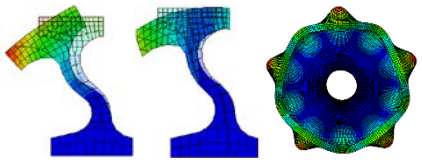
26	3159.1		
27	3244.2	Circumferential mode	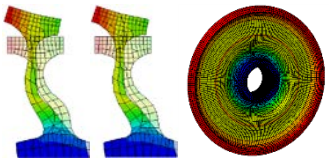
28	3621.4	(1,r)	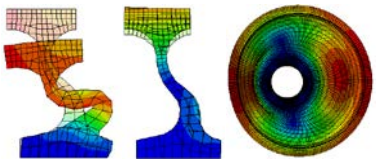
29	3783.4	(3,1)	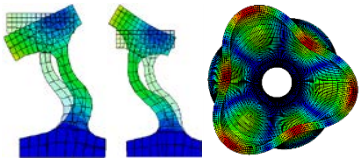
30	3783.4		
31	3896	(1,r)	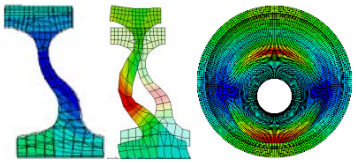
32	3934.7	(5,r)	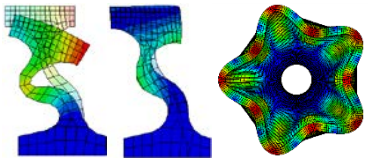
33	3934.7		
34	4233.9	(6,0)	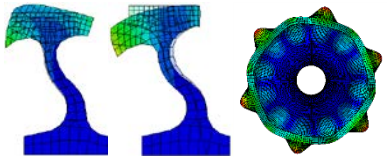
35	4233.9		
36	4572.7	Bending mode	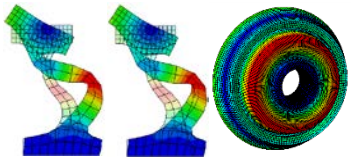

Mode Number	Frequency (Hz)	Mode Shape	
37	4605.6	Bending mode	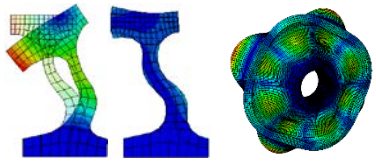
38	4605.6		
39	4646.6	Bending mode	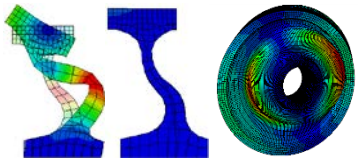
40	4703	Bending mode	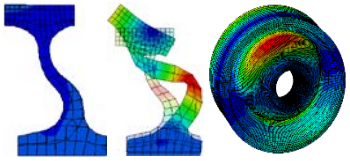
41	4792.4	Bending mode	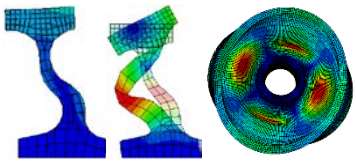
42	4792.4		
43	4881.8	bending mode	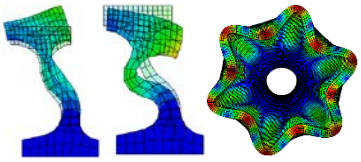
44	4881.8		
45	5162.3	Bending mode	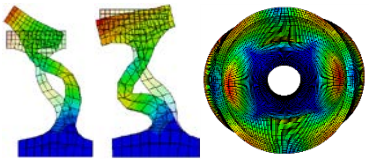
46	5162.3		
47	5301.7	(7,0)	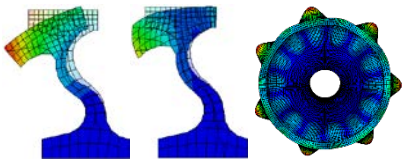
48	5301.7		
49	5346.9	(3,1)	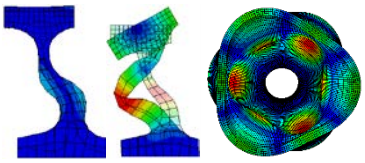
50	5346.9		
51	5477.5	(5,1)	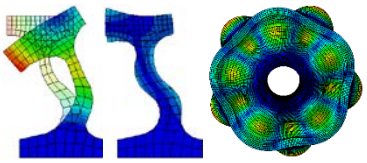
52	5477.5		

Appendix II Complex eigenvalue analysis results of curve squeal

(1) Results of 16 simulation cases with wheel/rail friction coefficient = 0.6 and no rail damping

1. Wheel diameter = 780mm, lateral shift = 0mm, wheel-rail μ=0.6

Wheel diameter: 780mm			
Lateral shift from the wheel nominal contact point: 0mm			
Mode shape	Frequency	Real part of eigenvalue	Effective damping ratio
rail vibration dominating	84.648	0.27928	-0.00105
wheel bending mode (1,0) and rail	475.14	0.29924	-0.0002
wheel bending mode (2,0) and rail	542.54	122.04	-0.0716
wheel bending mode (0,0) and rail	677.55	5.1989	-0.00244
wheel bending mode (3,0) and rail	1117.9	243.43	-0.06931
wheel bending mode (4,0)	2046.1	70.423	-0.01096
rail vibration dominating	2063.9	0.82439	-0.00013
rail vibration dominating	3440.5	15.027	-0.00139
rail vibration dominating	3517.1	0.89373	-0.00008
rail vibration dominating	4641.6	13.725	-0.00094
rail vibration dominating	4910.8	4.4705	-0.00029

2. Wheel diameter = 780mm, lateral shift = 10mm, wheel-rail μ=0.6

Wheel diameter: 780mm			
Lateral shift from wheel nominal contact point: 10mm			
Mode shape	Frequency	Real part of eigenvalue	Effective damping ratio
rail vibration dominating	84.504	0.1584	-0.0006
wheel bending mode (1,0) and rail	476.08	0.25123	-0.00017
wheel bending mode (2,0) and rail	544.91	169.29	-0.09889
wheel bending mode (0,0) and rail	674.95	5.7029	-0.00269
wheel bending mode (3,0) and rail	1117.6	260.42	-0.07417
wheel bending mode (4,0)	2040.6	85.702	-0.01337
rail vibration dominating	2063.5	0.1589	-0.00002
rail vibration dominating	3440.3	15.13	-0.0014
rail vibration dominating	3517.2	0.56615	-0.00005
rail vibration dominating	4643.2	15.255	-0.00105
rail vibration dominating	4910.9	1.7796	-0.00012

3. Wheel diameter = 780mm, lateral shift = 20mm, wheel-rail μ=0.6

Wheel diameter: 780mm			
Lateral shift from wheel nominal contact point: 20mm			
Mode shape	Frequency	Real part of eigenvalue	Effective damping ratio
rail vibration dominating	289.45	0.17112	-0.00019
wheel bending mode (1,0) and rail	476.94	0.19342	-0.00013
wheel bending mode (2,0) and rail	543.3	179.45	-0.10514
wheel bending mode (0,0) and rail	674.11	4.4782	-0.00211
wheel bending mode (3,0) and rail	1116.7	241.99	-0.06898
wheel bending mode (2,1)	2035.1	69.923	-0.01094
rail vibration dominating	3440.2	15.016	-0.00139
rail vibration dominating	3517.3	0.32001	-0.00003
rail vibration dominating	4644.3	10.651	-0.00073
rail vibration dominating	4911	0.87242	-0.00006
rail vibration dominating	5360.3	9.61E-02	-0.00001

4. Wheel diameter = 780mm, lateral shift = 30mm, wheel-rail μ=0.6

Wheel diameter: 780mm			
Lateral shift from wheel nominal contact point: 30mm			
Mode shape	Frequency	Real part of eigenvalue	Effective damping ratio
rail vibration dominating	288.84	0.31125	-0.00034
wheel bending mode (1,0) and rail	477.96	9.75E-02	-0.00006
wheel bending mode (2,0) and rail	538.45	156.8	-0.09269
wheel bending mode (0,0) and rail	675.3	1.3398	-0.00063
wheel bending mode (3,0) and rail	1114.6	177.48	-0.05069
wheel bending mode (2,1)	2029.1	18.087	-0.00284
rail vibration dominating	3440.1	15.5	-0.00143
rail vibration dominating	4644.6	4.7952	-0.00033
rail vibration dominating	4707.2	2.858	-0.00019
rail vibration dominating	4911	1.1953	-0.00008
rail vibration dominating	5360.2	0.24835	-0.00001

5. Wheel diameter = 800mm, lateral shift = 0mm, wheel-rail μ=0.6

Wheel diameter: 800mm			
Lateral shift from the wheel nominal contact point: 0mm			
Mode shape	Frequency	Real part of eigenvalue	Effective damping ratio
rail vibration dominating	89.47	14.836	-0.05278
wheel bending mode (1,0) and rail	432.66	6.4473	-0.00474
wheel bending mode (2,0) and rail	523.45	25.92	-0.01576
rail vibration dominating	610.75	0.20462	-0.00011
wheel bending mode (0,0) and rail	623.34	54.917	-0.02804
wheel bending mode (3,0) and rail	1145.8	125.89	-0.03497
rail vibration dominating	1971.7	55.982	-0.00904
wheel bending mode (4,0)	2108.5	23.981	-0.00362
rail vibration dominating	2129.3	0.16717	-0.00002
wheel bending mode and rail (5,0)	3146.7	1.6483	-0.00017
rail vibration dominating	4641.2	2.2232	-0.00015
rail vibration dominating	4911.8	11.761	-0.00076

6. Wheel diameter = 800mm, lateral shift = 10mm, wheel-rail μ=0.6

Wheel diameter: 800mm			
Lateral shift from wheel nominal contact point: 10mm			
Mode shape	Frequency	Real part of eigenvalue	Effective damping ratio
rail vibration dominating	89.542	8.7142	-0.03098
wheel bending mode (1,0) and rail	433.33	12.206	-0.00897
wheel bending mode (2,0) and rail	526.89	36.567	-0.02209
wheel bending mode (0,0) and rail	619.43	75.108	-0.0386
wheel bending mode (3,0) and rail	1144.5	160.63	-0.04467
rail vibration dominating	1399	4.23E-02	-0.00001
rail vibration dominating	1968.4	70.424	-0.01139
rail vibration dominating	4641.5	10.583	-0.00073
rail vibration dominating	4708.3	6.8604	-0.00046
rail vibration dominating	4911.3	9.2501	-0.0006
rail vibration dominating	5360.3	3.83E-02	0

7. Wheel diameter = 800mm, lateral shift = 20mm, wheel-rail μ=0.6

Wheel diameter: 800mm			
Lateral shift from wheel nominal contact point: 20mm			
Mode shape	Frequency	Real part of eigenvalue	Effective damping ratio
rail vibration dominating	89.34	3.7086	-0.01321
rail vibration dominating	288.73	2.81E-02	-0.00003
wheel bending mode (1,0) and rail	433.8	14.915	-0.01094
wheel bending mode (2,0) and rail	526.74	41.39	-0.02501
wheel bending mode (0,0) and rail	617.47	83.406	-0.043
wheel bending mode (3,0) and rail	1143.5	147.5	-0.04106
rail vibration dominating	1399.2	1.0814	-0.00025
rail vibration dominating	1962.9	70.357	-0.01141
rail vibration dominating	4642.7	14.038	-0.00096
rail vibration dominating	4709.6	5.8899	-0.0004
rail vibration dominating	4911.1	6.2173	-0.0004
rail vibration dominating	5360.3	0.35057	-0.00002

8. Wheel diameter = 800mm, lateral shift = 30mm, wheel-rail μ=0.6

Wheel diameter: 800mm			
Lateral shift from wheel nominal contact point: 30mm			
Mode shape	Frequency	Real part of eigenvalue	Effective damping ratio
rail vibration dominating	89.417	3.7169	-0.01323
rail vibration dominating	288.5	0.20217	-0.00022
wheel bending mode (1,0) and rail	434.15	16.655	-0.01221
wheel bending mode (2,0) and rail	522.71	38.432	-0.0234
wheel bending mode (0,0) and rail	616.86	79.82	-0.04119
wheel bending mode (3,0) and rail	1141.5	61.686	-0.0172
rail vibration dominating	1399.2	3.44E-02	-0.00001
rail vibration dominating	1956.7	34.78	-0.00566
rail vibration dominating	4643.8	12.521	-0.00086
rail vibration dominating	4710	0.69435	-0.00005
rail vibration dominating	4911.1	4.1887	-0.00027
rail vibration dominating	5360.4	0.47384	-0.00003

9. Wheel diameter = 820mm, lateral shift = 0mm, wheel-rail μ=0.6

Wheel diameter: 820mm			
Lateral shift from the wheel nominal contact point: 0mm			
Mode shape	Frequency	Real part of eigenvalue	Effective damping ratio
rail vibration dominating	87.414	44.648	-0.16258
wheel bending mode (2,0) and rail	519.42	15.378	-0.00942
wheel bending mode and rail	596.24	171.97	-0.09181
wheel bending mode (3,0) and rail	1186.6	10.117	-0.00271
rail vibration dominating	1960.3	3.9658	-0.00064
rail vibration dominating	2392.2	38.912	-0.00518
rail vibration dominating	3438.8	0.7727	-0.00007
rail vibration dominating	4371.8	0.18953	-0.00001
rail vibration dominating	4642.5	10.725	-0.00074

10. Wheel diameter = 820mm, lateral shift = 10mm, wheel-rail μ=0.6

Wheel diameter: 820mm			
Lateral shift from wheel nominal contact point: 10mm			
Mode shape	Frequency	Real part of eigenvalue	Effective damping ratio
rail vibration dominating	87.582	43.37	-0.15762
wheel bending mode (2,0) and rail	521.52	19.958	-0.01218
wheel bending and rail	594.77	190.5	-0.10195
wheel bending mode (3,0) and rail	1180.8	12.596	-0.0034
rail vibration dominating	1959.8	4.0102	-0.00065
wheel web bending mode and rail	2056.8	2.3417	-0.00036
rail vibration dominating	2389.8	34.344	-0.00457
rail vibration dominating	3438.8	0.53364	-0.00005
rail vibration dominating	4371.9	0.35484	-0.00003
rail vibration dominating	4643.9	7.0522	-0.00048

11. Wheel diameter = 820mm, lateral shift = 20mm, wheel-rail μ=0.6

Wheel diameter: 820mm			
Lateral shift from wheel nominal contact point: 20mm			
Mode shape	Frequency	Real part of eigenvalue	Effective damping ratio
rail vibration dominating	87.666	42.531	-0.15443
wheel bending mode (2,0) and rail	521.63	22.736	-0.01387
wheel bending mode and rail	593.7	201.08	-0.10781
wheel bending mode (3,0) and rail	1180.7	2.5071	-0.00068
rail vibration dominating	1960.5	1.1953	-0.00019
rail vibration dominating	2388	21.448	-0.00286
rail vibration dominating	3438.9	0.33209	-0.00003
rail vibration dominating	4371.9	0.55881	-0.00004
rail vibration dominating	4644	1.6707	-0.00011

12. Wheel diameter = 820mm, lateral shift = 30mm, wheel-rail μ=0.6

Wheel diameter: 820mm			
Lateral shift from wheel nominal contact point: 30mm			
Mode shape	Frequency	Real part of eigenvalue	Effective damping ratio
rail vibration dominating	87.661	42.139	-0.15301
rail vibration dominating	288.25	0.1632	-0.00018
wheel bending mode (2,0) and rail	519.58	23.055	-0.01412
rail vibration dominating	593.13	203.97	-0.10946
rail vibration dominating	2064.1	1.7167	-0.00026
rail vibration dominating	2388.5	5.9592	-0.00079
rail vibration dominating	3439	0.14347	-0.00001
rail vibration dominating	4371.9	0.79541	-0.00006
rail vibration dominating	4707.4	1.4187	-0.0001
rail vibration dominating	5360.2	3.85E-02	0

13. Wheel diameter = 840mm, lateral shift = 0mm, wheel-rail μ=0.6

Wheel diameter: 840mm			
Lateral shift from the wheel nominal contact point: 0mm			
Mode shape	Frequency	Real part of eigenvalue	Effective damping ratio
rail vibration dominating	85.448	57.202	-0.21309
wheel bending mode (2,0) and rail	516.9	10.396	-0.0064
wheel bending mode (1,0) and rail	578.51	166.35	-0.09153
wheel bending mode (3,0) and rail	1210.4	2.7593	-0.00073
wheel bending mode and rail	2389.5	0.83461	-0.00011
rail vibration dominating	3438.8	0.41079	-0.00004

14. Wheel diameter = 840mm, lateral shift = 10mm, wheel-rail μ=0.6

Wheel diameter: 840mm			
Lateral shift from wheel nominal contact point: 10mm			
Mode shape	Frequency	Real part of eigenvalue	Effective damping ratio
rail vibration dominating	85.61	56.491	-0.21004
wheel bending mode (2,0) and rail	518.32	12.822	-0.00787
wheel bending mode (1,0) and rail	577.59	188.12	-0.10367
wheel bending mode (3,0) and rail	1207	1.5802	-0.00042
wheel bending mode and rail	1961.9	0.46266	-0.00008
rail vibration dominating	3438.9	0.25565	-0.00002

15. Wheel diameter = 840mm, lateral shift = 20mm, wheel-rail μ=0.6

Wheel diameter: 840mm			
Lateral shift from wheel nominal contact point: 20mm			
Mode shape	Frequency	Real part of eigenvalue	Effective damping ratio
rail vibration dominating	85.705	55.949	-0.2078
wheel bending mode (2,0) and rail	518.49	14.493	-0.0089
wheel bending mode (1,0) and rail	576.82	201.89	-0.11141
wheel bending mode and rail	1989.1	2.3073	-0.00037
rail vibration dominating	3438.9	0.11849	-0.00001

16. Wheel diameter = 840mm, lateral shift = 30mm, wheel-rail μ=0.6

Wheel diameter: 840mm			
Lateral shift from wheel nominal contact point: 30mm			
Mode shape	Frequency	Real part of eigenvalue	Effective damping ratio
rail vibration dominating	85.731	55.56	-0.20629
rail vibration dominating	288.25	0.19311	-0.00021
wheel bending mode (2,0) and rail	517.37	15.298	-0.00941
wheel bending mode (1,0) and rail	576.27	207.94	-0.11486
wheel radial mode (2,r) and rail	1753.1	0.12414	-0.00002
wheel bending mode and rail	1988.8	1.1681	-0.00019
wheel bending mode (2,1) and rail	4689.5	0.34971	-0.00002
rail vibration dominating	4707.5	2.1129	-0.00014

(2) Results of 16 simulation cases with wheel/rail friction coefficient = 0.4 and no rail damping

1. Wheel diameter = 780mm, lateral shift = 0mm, wheel-rail μ=0.4

Wheel diameter: 780mm			
Lateral shift from the wheel nominal contact point: 0mm			
Mode shape	Frequency	Real part of eigenvalue	Effective damping ratio
rail vibration dominating	82.804	0.10992	-0.00042
wheel bending mode (1,0) and rail	474.01	0.33326	-0.00022
wheel bending mode (2,0) and rail	509.12	8.4135	-0.00526
wheel bending mode (0,0) and rail	684.85	0.87972	-0.00041
wheel bending mode (3,0) and rail	1121.3	158.31	-0.04494
wheel bending mode (4,0) and rail	2046.3	43.884	-0.00683
rail vibration dominating	3439.9	9.0738	-0.00084
rail vibration dominating	4642.1	2.8253	-0.00019
rail vibration dominating	4912.1	0.2343	-0.00002

2. Wheel diameter = 780mm, lateral shift = 10mm, wheel-rail μ=0.4

Wheel diameter: 780mm			
Lateral shift from wheel nominal contact point: 10mm			
Mode shape	Frequency	Real part of eigenvalue	Effective damping ratio
rail vibration dominating	82.976	6.67E-02	-0.00026
wheel bending mode (1,0) and rail	474.88	0.41635	-0.00028
wheel bending mode (2,0) and rail	506.08	9.1623	-0.00576
wheel bending mode (0,0) and rail	683.79	0.2631	-0.00012
wheel bending mode (3,0) and rail	1122.9	140.92	-0.03995
wheel bending mode (4,0) and rail	2042	44.992	-0.00701
rail vibration dominating	3440	9.7136	-0.0009
rail vibration dominating	4643.1	10.073	-0.00069

3. Wheel diameter = 780mm, lateral shift = 20mm, wheel-rail μ=0.4

Wheel diameter: 780mm			
Lateral shift from wheel nominal contact point: 20mm			
Mode shape	Frequency	Real part of eigenvalue	Effective damping ratio
rail vibration dominating	82.964	2.54E-02	-0.0001
wheel bending mode (1,0) and rail	475.83	0.54342	-0.00036
wheel bending mode (2,0) and rail	499.42	8.3889	-0.00535
rail vibration dominating	1117.6	22.958	-0.00654
wheel bending mode (2,1) and rail	2033.2	7.9362	-0.00124
rail vibration dominating	3440	9.5826	-0.00089
rail vibration dominating	4644.2	6.3015	-0.00043

4. Wheel diameter = 780mm, lateral shift = 30mm, wheel-rail μ=0.4

Wheel diameter: 780mm			
Lateral shift from wheel nominal contact point: 30mm			
Mode shape	Frequency	Real part of eigenvalue	Effective damping ratio
wheel bending mode (1,0) and rail	477.76	0.61809	-0.00041
wheel bending mode (2,0) and rail	488.86	6.1101	-0.00398
rail vibration dominating	610.8	3.66E-02	-0.00002
wheel bending mode (2,1) and rail	2023.5	0.82157	-0.00013
rail vibration dominating	3439.9	9.8432	-0.00091
rail vibration dominating	4644.2	1.3597	-0.00009

5. Wheel diameter = 800mm, lateral shift = 0mm, wheel-rail μ=0.4

Wheel diameter: 800mm			
Lateral shift from the wheel nominal contact point: 0mm			
Mode shape	Frequency	Real part of eigenvalue	Effective damping ratio
rail vibration dominating	84.299	0.23264	-0.00088
wheel bending mode (1,0) and rail	430.11	0.30828	-0.00023
wheel bending mode (2,0) and rail	505.45	4.9453	-0.00311
wheel bending mode (0,0) and rail	632.95	38.721	-0.01947
wheel bending mode (3,0) and rail	1164	4.2527	-0.00116
rail vibration dominating	1970.3	37.815	-0.00611
wheel bending mode	2106.5	0.39018	-0.00006
rail vibration dominating	2129.3	0.10785	-0.00002
rail vibration dominating	4912.1	4.816	-0.00031

6. Wheel diameter = 800mm, lateral shift = 10mm, wheel-rail μ=0.4

Wheel diameter: 800mm			
Lateral shift from wheel nominal contact point: 10mm			
Mode shape	Frequency	Real part of eigenvalue	Effective damping ratio
rail vibration dominating	84.533	0.18838	-0.00071
wheel bending mode (1,0) and rail	430.93	0.70552	-0.00052
wheel bending mode (2,0) and rail	503.73	5.6014	-0.00354
wheel bending mode (0,0) and rail	629.94	66.588	-0.03365
rail vibration dominating	1966.9	49.005	-0.00793
rail vibration dominating	4642.2	2.4751	-0.00017
rail vibration dominating	4708.8	4.2317	-0.00029
rail vibration dominating	4912	2.6179	-0.00017

7. Wheel diameter = 800mm, lateral shift = 20mm, wheel-rail μ=0.4

Wheel diameter: 800mm			
Lateral shift from wheel nominal contact point: 20mm			
Mode shape	Frequency	Real part of eigenvalue	Effective damping ratio
rail vibration dominating	84.521	0.13989	-0.00053
wheel bending mode (1,0) and rail	431.62	1.5035	-0.00111
wheel bending mode (2,0) and rail	500.09	5.5191	-0.00351
wheel bending mode (0,0) and rail	630.25	72.371	-0.03655
rail vibration dominating	1399.4	0.60592	-0.00014
rail vibration dominating	1961.6	33.774	-0.00548
rail vibration dominating	4642.8	8.7915	-0.0006
rail vibration dominating	4709.8	2.6657	-0.00018
rail vibration dominating	4912.1	0.97502	-0.00006

8. Wheel diameter = 800mm, lateral shift = 30mm, wheel-rail μ=0.4

Wheel diameter: 800mm			
Lateral shift from wheel nominal contact point: 30mm			
Mode shape	Frequency	Real part of eigenvalue	Effective damping ratio
rail vibration dominating	84.587	9.54E-02	-0.00036
wheel bending mode (1,0) and rail	431.93	2.9328	-0.00216
wheel bending mode (2,0) and rail	494.73	4.6919	-0.00302
wheel bending mode (0,0) and rail	631.33	60.638	-0.03057
rail vibration dominating	4643.9	8.1929	-0.00056
rail vibration dominating	4912.2	0.2246	-0.00001

9. Wheel diameter = 820mm, lateral shift = 0mm, wheel-rail μ=0.4

Wheel diameter: 820mm			
Lateral shift from the wheel nominal contact point: 0mm			
Mode shape	Frequency	Real part of eigenvalue	Effective damping ratio
rail vibration dominating	87.482	21.943	-0.07984
wheel bending mode (2,0) and rail	506.83	3.9983	-0.00251
rail vibration dominating	603.83	132.28	-0.06973
rail vibration dominating	1964.7	0.2475	-0.00004
rail vibration dominating	2391.6	24.747	-0.00329
rail vibration dominating	4642.8	6.381	-0.00044

10. Wheel diameter = 820mm, lateral shift = 10mm, wheel-rail μ=0.4

Wheel diameter: 820mm			
Lateral shift from wheel nominal contact point: 10mm			
Mode shape	Frequency	Real part of eigenvalue	Effective damping ratio
rail vibration dominating	87.632	23.115	-0.08396
wheel bending mode (2,0) and rail	505.71	4.6111	-0.0029
rail vibration dominating	605.34	141.36	-0.07433
rail vibration dominating	1964.3	0.28745	-0.00005
wheel web bending mode	2057	2.6785	-0.00041
rail vibration dominating	2389.8	17.036	-0.00227
rail vibration dominating	4644	3.0052	-0.00021

11. Wheel diameter = 820mm, lateral shift = 20mm, wheel-rail μ=0.4

Wheel diameter: 820mm			
Lateral shift from wheel nominal contact point: 20mm			
Mode shape	Frequency	Real part of eigenvalue	Effective damping ratio
rail vibration dominating	87.611	22.958	-0.08341
wheel bending mode (2,0) and rail	503.26	4.838	-0.00306
rail vibration dominating	606.12	141.78	-0.07446
rail vibration dominating	2390.2	3.6631	-0.00049
rail vibration dominating	4372.1	9.97E-02	-0.00001
rail vibration dominating	4643.8	8.11E-02	-0.00001

12. Wheel diameter = 820mm, lateral shift = 30mm, wheel-rail μ=0.4

Wheel diameter: 820mm			
Lateral shift from wheel nominal contact point: 30mm			
Mode shape	Frequency	Real part of eigenvalue	Effective damping ratio
rail vibration dominating	87.506	23.715	-0.08626
wheel bending mode (2,0) and rail	499.51	4.5056	-0.00287
rail vibration dominating	606.86	135.49	-0.07107
rail vibration dominating	2391	0.69237	-0.00009
rail vibration dominating	4372.1	0.2312	-0.00002

13. Wheel diameter = 840mm, lateral shift = 0mm, wheel-rail μ=0.4

Wheel diameter: 840mm			
Lateral shift from the wheel nominal contact point: 0mm			
Mode shape	Frequency	Real part of eigenvalue	Effective damping ratio
rail vibration dominating	85.59	40.586	-0.15094
wheel bending mode (2,0) and rail	507.46	3.3098	-0.00208
wheel bending mode and rail	584.35	94.114	-0.05127

14. Wheel diameter = 840mm, lateral shift = 10mm, wheel-rail μ=0.4

Wheel diameter: 840mm			
Lateral shift from wheel nominal contact point: 10mm			
Mode shape	Frequency	Real part of eigenvalue	Effective damping ratio
rail vibration dominating	85.74	41.378	-0.15362
wheel bending mode (2,0) and rail	506.72	3.8581	-0.00242
wheel bending mode and rail	585.58	96.572	-0.05249

15. Wheel diameter = 840mm, lateral shift = 20mm, wheel-rail μ=0.4

Wheel diameter: 840mm			
Lateral shift from wheel nominal contact point: 20mm			
Mode shape	Frequency	Real part of eigenvalue	Effective damping ratio
rail vibration dominating	85.742	41.146	-0.15275
wheel bending mode (2,0) and rail	505	4.1658	-0.00263
wheel bending mode and rail	586.03	94.857	-0.05152
wheel web bending	1989.4	1.7494	-0.00028

16. Wheel diameter = 840mm, lateral shift = 30mm, wheel-rail μ=0.4

Wheel diameter: 840mm			
Lateral shift from wheel nominal contact point: 30mm			
Mode shape	Frequency	Real part of eigenvalue	Effective damping ratio
rail vibration dominating	85.675	41.189	-0.15303
wheel bending mode (2,0) and rail	502.29	4.1288	-0.00262
wheel bending mode and rail	586.31	85.384	-0.04635

(3) Results of 16 simulation cases with wheel/rail friction coefficient = 0.2 and no rail damping

1. Wheel diameter = 780mm, lateral shift = 0mm, wheel-rail μ=0.2

Wheel diameter: 780mm			
Lateral shift from the wheel nominal contact point: 0mm			
Mode shape	Frequency	Real part of eigenvalue	Effective damping ratio
rail vibration dominating	81.308	8.48E-03	-0.00003
wheel bending mode (1,0) and rail	471.53	0.1818	-0.00012
wheel bending mode (2,0) and rail	492.03	0.65363	-0.00042
wheel bending mode (4,0) and rail	2041.5	1.8956	-0.0003
rail vibration dominating	3439.8	3.4811	-0.00032

2. Wheel diameter = 780mm, lateral shift = 10mm, wheel-rail μ=0.2

Wheel diameter: 780mm			
Lateral shift from wheel nominal contact point: 10mm			
Mode shape	Frequency	Real part of eigenvalue	Effective damping ratio
wheel bending mode (1,0) and rail	471.08	0.33332	-0.00023
wheel bending mode (2,0) and rail	487	0.48416	-0.00032
wheel bending mode (4,0) and rail	2034.5	0.20701	-0.00003
rail vibration dominating	3439.8	3.2769	-0.0003
rail vibration dominating	4643.2	3.4665	-0.00024

3. Wheel diameter = 780mm, lateral shift = 20mm, wheel-rail μ=0.2

Wheel diameter: 780mm			
Lateral shift from wheel nominal contact point: 20mm			
Mode shape	Frequency	Real part of eigenvalue	Effective damping ratio
rail vibration dominating	81.292	6.77E-03	-0.00003
wheel bending mode (1,0) and rail	469.24	0.64397	-0.00044
wheel bending mode (2,0) and rail	481.63	0.0989457	-0.00007
rail vibration dominating	3439.7	3.1458	-0.00029
rail vibration dominating	4643.9	1.4333	-0.0001

4. Wheel diameter = 780mm, lateral shift = 30mm, wheel-rail μ=0.2

Wheel diameter: 780mm			
Lateral shift from wheel nominal contact point: 30mm			
Mode shape	Frequency	Real part of eigenvalue	Effective damping ratio
wheel bending mode (1,0) and rail	464.55	0.72757	-0.0005
rail vibration dominating	3439.8	4.3208	-0.0004

5. Wheel diameter = 800mm, lateral shift = 0mm, wheel-rail μ=0.2

Wheel diameter: 800mm			
Lateral shift from the wheel nominal contact point: 0mm			
Mode shape	Frequency	Real part of eigenvalue	Effective damping ratio
rail vibration dominating	81.796	2.12E-02	-0.00008
wheel bending mode (1,0) and rail	427.93	0.0542131	-0.00004
wheel bending mode (2,0) and rail	494.09	0.55891	-0.00036
wheel bending mode (0,1) and rail	642.07	13.771	-0.00683
rail vibration dominating	1969.3	19.588	-0.00317
rail vibration dominating	2129.3	2.05E-02	0
rail vibration dominating	4912.9	0.18051	-0.00001

6. Wheel diameter = 800mm, lateral shift = 10mm, wheel-rail μ=0.2

Wheel diameter: 800mm			
Lateral shift from wheel nominal contact point: 10mm			
Mode shape	Frequency	Real part of eigenvalue	Effective damping ratio
rail vibration dominating	81.792	1.47E-02	-0.00006
wheel bending mode (1,0) and rail	427.78	0.0769657	-0.00006
wheel bending mode (2,0) and rail	490.5	0.54453	-0.00035
rail vibration dominating	1965.2	17.975	-0.00291
rail vibration dominating	4709.4	8.39E-02	-0.00001

7. Wheel diameter = 800mm, lateral shift = 20mm, wheel-rail μ=0.2

Wheel diameter: 800mm			
Lateral shift from wheel nominal contact point: 20mm			
Mode shape	Frequency	Real part of eigenvalue	Effective damping ratio
rail vibration dominating	81.806	1.72E-02	-0.00007
wheel bending mode (1,0) and rail	427.27	0.0960207	-0.00007
wheel bending mode (2,0) and rail	485.92	0.46674	-0.00031
rail vibration dominating	1399.5	6.86E-02	-0.00002
rail vibration dominating	1966.3	7.28E-02	-0.00001
rail vibration dominating	2129.3	5.69E-02	-0.00001
rail vibration dominating	4643.1	2.0618	-0.00014

8. Wheel diameter = 800mm, lateral shift = 30mm, wheel-rail μ=0.2

Wheel diameter: 800mm			
Lateral shift from wheel nominal contact point: 30mm			
Mode shape	Frequency	Real part of eigenvalue	Effective damping ratio
rail vibration dominating	81.841	1.68E-02	-0.00007
wheel bending mode (1,0) and rail	426.36	0.11305	-0.00008
wheel bending mode (2,0) and rail	480.66	0.31463	-0.00021
rail vibration dominating	4643.8	3.1147	-0.00021

9. Wheel diameter = 820mm, lateral shift = 0mm, wheel-rail μ=0.2

Wheel diameter: 820mm			
Lateral shift from the wheel nominal contact point: 0mm			
Mode shape	Frequency	Real part of eigenvalue	Effective damping ratio
rail vibration dominating	82.643	5.05E-02	-0.00019
wheel bending mode (2,0) and rail	497.46	0.51797	-0.00033
wheel bending mode (0,1) and rail	611.4	63.963	-0.0333
rail vibration dominating	2391.5	7.9321	-0.00106
rail vibration dominating	4643.3	2.2324	-0.00015

10. Wheel diameter = 820mm, lateral shift = 10mm, wheel-rail μ=0.2

Wheel diameter: 820mm			
Lateral shift from wheel nominal contact point: 10mm			
Mode shape	Frequency	Real part of eigenvalue	Effective damping ratio
rail vibration dominating	82.64	4.38E-02	-0.00017
wheel bending mode (2,0) and rail	494.65	0.5283	-0.00034
wheel bending mode (0,1) and rail	612.93	40.978	-0.02128
wheel web bending mode	2057.2	2.003	-0.00031
rail vibration dominating	2392.1	0.73295	-0.0001

11. Wheel diameter = 820mm, lateral shift = 20mm, wheel-rail μ=0.2

Wheel diameter: 820mm			
Lateral shift from wheel nominal contact point: 20mm			
Mode shape	Frequency	Real part of eigenvalue	Effective damping ratio
rail vibration dominating	82.674	3.78E-02	-0.00015
wheel bending mode (2,0) and rail	490.96	0.47181	-0.00031
wheel bending mode (0,1) and rail	608.75	3.6635	-0.00192
rail vibration dominating	2392.5	6.30E-02	-0.00001

12. Wheel diameter = 820mm, lateral shift = 30mm, wheel-rail μ=0.2

Wheel diameter: 820mm			
Lateral shift from wheel nominal contact point: 30mm			
Mode shape	Frequency	Real part of eigenvalue	Effective damping ratio
rail vibration dominating	82.785	5.49E-02	-0.00021
wheel bending mode (2,0) and rail	486.54	0.39554	-0.00026
wheel bending mode (0,1) and rail	604.04	0.48198	-0.00025

13. Wheel diameter = 840mm, lateral shift = 0mm, wheel-rail μ=0.2

Wheel diameter: 840mm			
Lateral shift from the wheel nominal contact point: 0mm			
Mode shape	Frequency	Real part of eigenvalue	Effective damping ratio
rail vibration dominating	85.75	7.8972	-0.02932
wheel bending mode (2,0) and rail	499.54	0.47435	-0.0003
wheel bending mode (0,1) and rail	576.33	1.6215	-0.0009

14. Wheel diameter = 840mm, lateral shift = 10mm, wheel-rail μ=0.2

Wheel diameter: 840mm			
Lateral shift from wheel nominal contact point: 10mm			
Mode shape	Frequency	Real part of eigenvalue	Effective damping ratio
rail vibration dominating	85.727	8.0905	-0.03004
wheel bending mode (2,0) and rail	497.31	0.49735	-0.00032
wheel bending mode (0,1) and rail	575.24	1.2844	-0.00071

15. Wheel diameter = 840mm, lateral shift = 20mm, wheel-rail μ=0.2

Wheel diameter: 840mm			
Lateral shift from wheel nominal contact point: 20mm			
Mode shape	Frequency	Real part of eigenvalue	Effective damping ratio
rail vibration dominating	85.646	9.7605	-0.03628
wheel bending mode (2,0) and rail	494.33	0.46587	-0.0003
wheel bending mode (0,1) and rail	573.85	0.93593	-0.00052

16. Wheel diameter = 840mm, lateral shift = 30mm, wheel-rail μ=0.2

Wheel diameter: 840mm			
Lateral shift from wheel nominal contact point: 30mm			
Mode shape	Frequency	Real part of eigenvalue	Effective damping ratio
rail vibration dominating	85.469	12.915	-0.0481
wheel bending mode (2,0) and rail	490.7	0.41336	-0.00027
wheel bending mode (0,1) and rail	572.36	0.67856	-0.00038

Appendix III Parameters list for a sample vehicle model

Table 2 Full parameter list for a sample vehicle model

Parameter name	Value (VAMPIRE® unit)	Notes
Axl_Lat_Gap	5.0	Bearing adapter lateral clearance
Axl1_x	Bols_x+0.5*Wheelbase	
Axl2_x	Bols_x-0.5*Wheelbase	
Axle_Box_Width	0.280	Bearing adapter width
Axle_Long_Gap	5.0	Bearing adapter longitudinal clearance
Axlebox_Center	1.98	Lateral offset of axlebox from vehicle centerline
AxleBox_Mu	0.4	Bearing adapter friction coefficient
AxleBox_y	0.5*Axlebox_Center	Bearing adapter lateral offset
AxleBox_y1	0.5*Axlebox_Center+0.5*Axle_Box_Width	Bearing adapter outer edge lateral offset
AxleBox_y2	0.5*Axlebox_Center-0.5*Axle_Box_Width	Bearing adapter inner edge lateral offset
Bols_x	0.5*Truck_Center_Distance	
Bolster_CGh	0.41429	Bolster center of gravity vertical height
Bolster_Ixx	0.2346	Bolster roll inertia
Bolster_Iyy	0.0149	Bolster pitch inertial
Bolster_Izz	0.2342	Bolster yaw inertia
Bolster_Mass	0.5876	Bolster weight Mg
Bolster_Wgt	Bolster_Mass*9.81	Bolster weight KN
Car_Body_CGh	1.26651	Car body center of gravity vertical height
Car_Body_Ixx	52.55321	Car body roll inertia
Car_Body_Iyy	3706.1	Car body pitch inertia
Car_Body_Izz	3741.802	Car body yaw inertia
Car_Body_Mass	82.68908	Car body weight Mg
Carbody_Wgt	Car_Body_Mass*9.81	Car body weight KN
CC_Static	9.345	Control coil nest static load
CoilA_Kc	Outer_Kc+Inner_Kc	
CoilA_Ks	Outer_Ks+Inner_Ks	S3 outer coil plus S6 inner coil
CoilA_Kt	Outer_Kt+Inner_Kt	
CoilA_Kz	Outer_Kz+Inner_Kz	

Parameter name	Value (VAMPIRE® unit)	Notes
CoilB_Kc	Outer_Kc	
CoilB_Ks	Outer_Ks	S3 outer coil
CoilB_Kt	Outer_Kt	
CoilB_Kz	Outer_Kz	
Col_Spacing	0.420	Longitudinal spacing between side frame columns
Col1_x	Bols_x+0.5*Col_Spacing	
Col2_x	Bols_x-0.5*Col_Spacing	
Column_Mu	0.4	Column coefficient of friction
Comp_Mu	0.465763	Effective wedge friction coefficient in compression
Coupler_EDR	0.00175127	Longitudinal damping
Coupler_Hgt	0.890000	Coupler height
Coupler_Stf	0.17512680	Longitudinal stiffness
CPlate_Dia	0.3520000	Center plate diameter
CPlate_Gap	2.0000	Center plate radial gap
CPlate_Hgt	0.684-0.06061	Center plate height ATOR
CPlate_Mu	0.3333	Center plate coefficient of friction
CPlate_Rad	0.5*CPlate_Dia	Center plate radius
D_AxleBox	0.5*Fabx_Static*AxleBox_Mu/3.0	Axle box equivalent damping @ 3 in/sec
D_CPlate	0.25*Fcpl_Static*CPlate_Mu	Center plate equivalent damping @ 1 in/sec
D_FricWdg	Fcol_Static*Column_Mu/12.0	Friction wedge equivalent damping @ 12 in/sec
D_SdBear	SdBear_Pre*SdBear_Mu/3.0	Side bearing equivalent damping @ 3 in/sec
Delta	0.02540000	Bumpstop nominal half length
Extn_Mu	0.479582	Effective wedge friction coefficient in extension
Fabx_Static	0.5*Fspr_Static+0.5*SdFrame_Wgt	
Fcol_Static	1.303225*CC_Static	Column static load
Fcpl_Static	0.5*Carbody_Wgt-2.0*SdBear_Pre	
Fspr_Load	Fspr_Static	Spring group static load
Fspr_Static	0.25*Carbody_Wgt+0.5*Bolster_Wgt	
Gib_Height	0.46629	Bolster gib height ATOR
Gib_Spacing	0.42	Longitudinal spacing between bolster gib contacts

Parameter name	Value (VAMPIRE® unit)	Notes
Gib1_x	Bols_x+0.5*Gib_Spacing	
Gib2_x	Bols_x-0.5*Gib_Spacing	
Inner_Kc	0.0	S6 inner cardan rate
Inner_Ks	0.0148	S6 inner shear stiffness
Inner_Kt	0.0	S6 inner torsional stiffness
Inner_Kz	0.206	S6 inner vertical stiffness
Insde_GibClr	15.0	Inside bolster gib clearance
K_CPlate	450	Center plate contact stiffness
K_Rigid	87.5634	Rigid Stiffness
K_SdBear	1.4797	Side bearing contact stiffness
K_Soft	0.00000018	Soft Stiffness
K_Warping	1.05	warp stiffness
Offset_xa	0.1407	First spring coil longitudinal offset
Offset_xb	0.07035	Second spring coil longitudinal offset
Offset_y	0.14287500	Spring coil lateral offset
Outer_Height	0.26000	D5 outer spring height
Outer_Kc	0.0	S3 outer cardan rate
Outer_Ks	0.1194	S3 outer spring shear stiffness
Outer_Kt	0.0	S3 outer torsional stiffness
Outer_Kz	0.396	S3 outer spring vertical stiffness
Outsd_GibClr	15.0	Outside bolster gib clearance
SdBear_Ctr	1.270000	Side bearing lateral center distance
SdBear_Hgt	0.696	Side bearing height ATOR
SdBear_Mu	0.4	Side bearing coefficient of friction
SdBear_Pre	26.6893	Side bearing preload
SdBear_y	0.5*SdBear_Ctr	Side bearing lateral offset
Sdfm_x	Bols_x	
SdFrame_Wgt	Side_Frame_Mass*9.81	Side frame weight KN
Side_Frame_CGh	0.4646	Side frame vertical center of gravity height
Side_Frame_CGy	0.9900	Lateral offset of side frame from vehicle center line
Side_Frame_Ixx	0.0164	Side frame roll inertia
Side_Frame_Iyy	0.1345	Side frame pitch inertial
Side_Frame_Izz	0.1219	Side frame yaw inertia
Side_Frame_Mass	0.3547	Side frame weight Mg

Parameter name	Value (VAMPIRE® unit)	Notes
SprGrp_Base	Wheel_Rad-0.2338	Height ATOR of spring group base
SprGrp_Defl	Fspr_Load/SprGrp_Kz	Spring group deflection under static load
SprGrp_Kz	7.0*Outer_Kz+3.0*Inner_Kz	Total spring group vertical stiffness
SprGrp_Top	Outer_Height-SprGrp_Defl*1E-3+SprGrp_Base	Height ATOR at top of spring group
SprGrp_x	Bols_x	
SprGrp_x1	Bols_x+Offset_xb	
SprGrp_x2	Bols_x-Offset_xb	
SprGrp_x3	Bols_x+Offset_xa	
SprGrp_x4	Bols_x-Offset_xa	
SprGrp_y	0.5*Spring_Group_Center	Spring center row lateral offset
SprGrp_y1	0.5*Spring_Group_Center+Offset_y	Spring outer row lateral offset
SprGrp_y2	0.5*Spring_Group_Center-Offset_y	Spring inner row lateral offset
Spring_Group_Center	1.980	Lateral offset of spring group center from vehicle centerline
Truck_Center_Distance	16.70000	Distance between truck centers
Wdg_Ktang	175.126800	Wedge face shear (tangential) stiffness
Wedge_Hgt	0.47779	Friction wedge height ATOR
Wheel_Diameter	0.84	Diameter of wheel
Wheel_Rad	0.5*Wheel_Diameter	Wheel nominal rolling radius
Wheel_Set_Ixx	0.5728	Whee set roll inertia
Wheel_Set_Iyy	0.0769	Wheel set pitch inertia
Wheel_Set_Izz	0.5728	Wheel set yaw inertia
Wheel_Set_Mass	1.0832	Wheel set weight
Wheelbase	1.72700	Longitudinal distance between axles of the same truck
WSet_XMass	Wheel_Set_Iyy/Wheel_Rad/Wheel_Rad	Extra wheel set mass due to pitch inertia

Appendix IV The deformable wheel and rigid rail model

The wheel is meshed with solid elements and refined around the contact zone, while the rail is represented by a rigid cylinder with a radius of 190 mm, which is a typical radius of the arc on the railhead at the wheel-rail contact position. The rail cylinder is fixed to a referenced point in the centre line of the cylinder; while the wheel boundary condition is the same of the model of the deformable wheel and deformable rail model shown in Chapter 4.

In Step 1 and 2, wheel and rail cylinder frictionless contact was established, by first applying small normal force, 100 N and then full axle loading, 65 kN. In Step 3, steady-state rotational motion of the rail cylinder, which is equivalent to the steady sliding between wheel and rail was established. The friction was changed from 0 to 0.6 in intervals of 0.1. A constant lateral sliding unit velocity was applied to the set of all the wheel nodes. Step 4 and 5, real eigenvalues and complex eigenvalues were extracted.

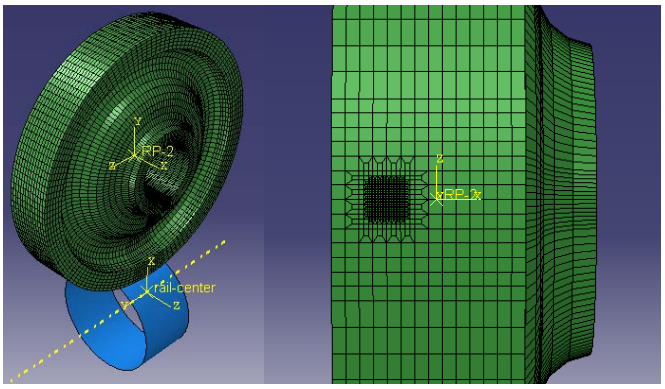

Figure IV-1 Deformable wheel and rigid rail squeal prediction model